Femtosecond-laser-induced reactions at surfaces

Richard Finlay

Harvard University

Cambridge, Massachusetts

February 1998

Femtosecond-laser-induced reactions at surfaces

A thesis presented

by

Richard John Finlay

to

the Department of Physics

in partial fulfillment of the requirements

for the degree of

Doctor of Philosophy

in the subject of

physics

Harvard University

Cambridge, Massachusetts

February 1998

ABSTRACT

We have experimentally studied chemical reactions at the surfaces of platinum and silicon using subpicosecond laser pulses to induce the reactions. The laser pulses stimulate electrons, which in turn stimulate molecules adsorbed on the surface. Irradiation of $CO/O_2/Pt(111)$ with 300-fs laser pulses yields O_2 and CO_2. We measured the yields of O_2 and CO_2 induced by laser pulses of various wavelengths to determine that nonthermalized electrons stimulate the adsorbates. When the fluence in the laser pulses is high, the effective cross section for desorption is high compared to the cross section measured using an arc lamp source. We demonstrated that by controlling the fluence in the subpicosecond laser pulses we can access either the low or high cross section regimes. We used isotopic labeling to show that the O_2 desorption is molecular, and to discover some properties of the pathway to CO_2. In many simulations of molecular dynamics following subpicosecond-pulsed laser excitation, the substrate is assumed to be static. We discovered, however, that subpicosecond laser pulses with fluences above 50 $\mu J/mm^2$ induce reaction between O_2 adsorbed on Pt(111) and atoms from beneath the surface — atoms near the surface move. Laser pulses of even higher fluence ablate the substrate. We irradiated silicon surfaces with 10 000-$\mu J/mm^2$, 100-fs laser pulses in a chamber filled with halogen gases. We discovered that sharp spikes develop on the surface, and deduced some of the elements of a model for the spike formation. We also report discovery of an electron-beam induced reaction in $C_6H_6/O_2/Pt(111)$ that yields phenol.

CONTENTS

ACKNOWLEDGMENTS

It was a pleasure to be a graduate student under Prof. Eric Mazur's supervision. Eric makes graduate school fun, partly because he has great confidence in his students. He gives us more privileges than we deserve. Eric spent many hours trying to teach me to write clearly; as you read this thesis I hope you will excuse me for not learning more from his example.

Professor Cynthia Friend has been a marvelous resource. She and her students taught me everything I know about chemistry and suggested many of the experiments in this thesis. Prof. Isaac Silvera generously shared his vast experimental knowledge when my work was stalled by mechanical and electrical problems. Professors F. Spaepen, E. Heller, and N. Bloembergen from Harvard, and Prof. H. Li from the University of Hong Kong indulgently listened to my speculations about the meaning of early experimental results. Professors Baldassare DiBartolo and Itamar Burak have consistently encouraged me.

My friend and colleague Tsing-Hua Her was instrumental in the completion of all the experiments in this thesis. He is tremendously resourceful at solving lab problems and has a marvelous sense of humor about the ridiculous means we contrived to take some of the data. Our early mentor in the fields of resourcefulness and humor was Dr. Jay Goldman. Our mentor in the field of positive thinking was Dr. Shrenik Deliwala. Dr. Walter Mieher taught Tsing-Hua, Shrenik, Jay and I about ultrahigh vacuum. Without Walter we would never have started the experiments, let alone push through the problems to successful solutions. Tsing-Hua and I were joined by Claudia Wu who is now turning many of our qualitative observations into real scientific data. Tsing-Hua, Claudia and I benefited enormously from Jenny Hoffman, an undergraduate who keeps us on our toes. Jenny took much of the data in the appendix to this thesis.

I

Introduction

1.1 General overview

This thesis describes experimental study of chemical reactions induced on surfaces by subpicosecond laser pulses. The laser pulses excite electrons in the surface faster than the electrons can transfer energy to the phonons, which allows the electrons to get very hot while the phonons remain cold. We studied chemical reactions on platinum and silicon during this nonequilibrium excitation.

The experiments on platinum are conducted in ultra-high vacuum (pressure less than 10^{-10} torr) at low temperature (84 K). We put O_2 and CO on the platinum surface and induce desorption of O_2 and reaction to make CO_2 by irradiating the platinum with 300-fs laser pulses of various wavelengths. The states of the photo-excited electrons depend on the laser wavelength, and so by comparing the desorption and reaction yields at different wavelengths we can infer which electronic states are responsible for exciting the O_2 and CO. We find that the adsorbates are stimulated by electrons from states far above the Fermi level compared with thermal energy scales ($k_B T$). [1-5] These experiments are described in chapter 3.

When O_2 adsorbs on a platinum surface, the O–O bond stretches compared to the gas phase. If the platinum is slowly heated, some O_2 molecules desorb without breaking the O–O bond. This is called molecular desorption. However, some of the O_2 molecules do dissociate to form atoms, and at higher temperatures these atoms recombine to desorb as molecules. This is called recombinative desorption. Which pathway is responsible for the desorption of O_2 when subpicosecond laser pulses excite the surface? Our intuition can be fooled. On one hand, the substrate phonon temperature is low, so we may expect only molecular desorption. On the other hand, the substrate electron temperature is high, so we may expect recombinative desorption. We used isotopic labeling to show that the O_2 desorption is molecular. We also discovered some properties of the pathway to CO_2. [6, 7] These experiments are described in chapter 4.

Reactants sometimes come from beneath the surface. For example, if a metal containing impurities is annealed in oxygen, impurities from the bulk of the metal can diffuse to the surface and react with the oxygen. We discovered that subpicosecond laser pulses induce reaction between O_2 on the platinum surface and atoms from beneath the surface. This reaction only occurs at high laser fluences (greater than 50 $\mu J/mm^2$). The results show that a surface irradiated with subpicosecond laser pulses is not static — atoms near the surface move. Our observations indicate that one cannot model adsorbate dynamics using the equilibrium potential energy surfaces. This work is described in chapter 5.

Laser pulses of even higher fluence ablate the substrate. We irradiated silicon surfaces with 10 000-$\mu J/mm^2$, 100-fs laser pulses in a chamber filled with halogen gases. The halogens react with the silicon to create volatile silicon halides. In these experiments, there is both physical ablation, and chemical etching. We discovered that sharp spikes develop on the silicon surface after 500 laser pulses. We have deduced some of the elements of a model for the spike formation. [8, 9] These experiments are the topic of chapter 6.

Many photo-activated reactions can also be driven by an electron beam. For example, both light and electrons cause O_2 dissociation on palladium. Experiments show that the oxygen atoms released when O_2 dissociates have a high translational energy, and should therefore readily react with coadsorbates. We discovered that an electron beam does indeed induce reaction between O_2 and coadsorbed benzene (C_6H_6) on platinum. The product is phenol (C_6H_5OH). We are currently comparing the yields induced with electrons with the yield induced by subpicosecond laser pulses. This ongoing work is described in an appendix.

Chapter 2 is an introduction to aspects of surface science and light-matter interactions that are relevant to these experiments. Technical details about detection of the laser-induced desorption yields are in sections 3.2, and 3.3. The references for all chapters are collected together at the end of the thesis.

II

Background

2.1 Chemical bonds

When atoms are close together, the electrons from different atoms interact and may form chemical bonds. Attraction between the atoms causes the atoms in a molecule (or solid) to have lower total energy than separate atoms. At close range the atoms repel each other, preventing the molecule from collapsing. A potential energy surface which represents these qualitative features of the interaction is sketched in Figure 2.1.
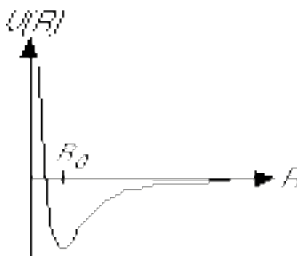
Figure 2.1 The qualitative form of the interaction potential between two nuclei in a diatomic molecule. The potential energy is plotted against the separation of the nuclei. The equilibrium separation of the nuclei is R_0.

The total energy of the molecule depends on the motion of the nuclei such as vibrations or rotations of the molecule and translation of the center of mass. While considering the internal excitation of the molecule, we typically ignore the translational

energy. The various internal excitations evolve on very different timescales. Electronic motion occurs at about 10^{15} Hz. Vibrations occur at about 10^{13} Hz. Rotational motion is slower still at 10^7–10^{11} Hz. The electronic part of the Schrödinger equation may be solved while assuming the nuclei are at fixed locations because the electronic motion occurs so much more quickly than the nuclear motions. With this Born-Oppenheimer approximation we write the wavefunction as a separable function:

$$\Psi \approx \Psi_e(\vec{r}_e, \bar{R}_N)\chi_N(\bar{R}_N) \approx \Psi_e \Psi_v \Psi_R .$$
(2.1)

Here the nuclear wavefunction χ_N is written as a product of vibrational, Ψ_v, and rotational, Ψ_R, components.

The strongest bond is the covalent bond, which is formed by an overlap of charge distribution between neighboring atoms. The lowering of the total energy comes about because electrons are shared between nuclei. Figure 2.2 schematically illustrates covalent bonding between two atoms. If the two atoms get close enough for the atomic orbitals to overlap, then the wavefunctions of these orbitals can add with either the same or opposite phase. The two new orbitals have different energies. The lower level corresponds to the wavefunctions adding in phase while the upper level corresponds to adding with opposite phase. Electrons which occupy the symmetric state are concentrated primarily in between the two nuclei; they draw both nuclei towards the center by coulomb attraction to the positive charges on the nuclei. They are known as bonding orbitals. The electrons in the anti-symmetric wavefunctions, however, have a low probability of being between the nuclei. Electrons in these states tend to pull the molecule apart, and are called anti-bonding. If both of the original electronic levels in each atom were singly occupied, then in the ground state of the new system, the two electrons occupy the bonding orbital. Since this state is energetically more favorable than the state in which the two atoms are separated, the sharing of the two electrons results in a bond between the two atoms. In the case of a solid consisting of many atoms, the bonding and antibonding levels broaden into bands. We return to the topic of bands below.
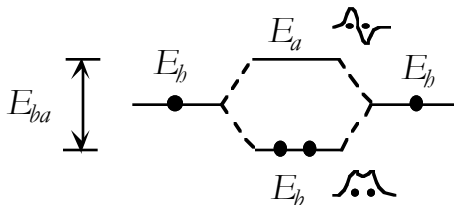
Figure 2.2 Energy level splitting in a covalent bond between two atoms.

The wavefunctions sketched in Figure 2.2 represent the combination of two *s*-orbitals. In general, the combination of the orbitals is more complicated. If the combined orbital is symmetric under rotation about the nuclear axis then the resulting bond is called a σ-bond.

The bonding of two atoms is determined by the balance between the electrons in bonding orbitals, and electrons in anti-bonding orbitals. For example, two hydrogen atoms (each in a ground-state $1s^1$ configuration) make H_2 because each atom contributes one electron to a σ bonding orbital. The orbital may contain two electrons without violating the Pauli exclusion principle because there are two available spins for each electron. Two He atoms, however, do not form a bond because the initial $1s^2$ configuration of each atom would result in a molecule with two electrons in a bonding orbital, and two electrons in an anti-bonding orbital, for no net bonding.

The formation of diatomic oxygen, O_2, is more complicated because each atom has 4 valence electrons. Three electrons from each atom go into bonding orbitals: 2 in each of two π orbitals, and 2 in the σ orbital. The remaining two electrons go into anti-bonding π^* orbitals. Overall there are 4 more electrons in bonding orbitals than anti-bonding. A full bond is formed when two electrons occupy a bonding orbital. Molecular oxygen has four such electrons, so O_2 has a double bond.

2.2 Vibrations of diatomic molecules

We now consider the vibrational motion of the nuclei in a diatomic molecule. Figure 2.1 qualitatively illustrates the interaction between two atoms comprising a molecule. The equilibrium separation of the atoms is R_0. The vibrations are usually small with respect to

the internuclear separation, R. Writing the potential as a Taylor series expansion about the equilibrium position R_0 in terms of $Q \equiv R - R_0$, we have

$$U(Q) = U(0) + \left(\frac{dU}{dQ}\right)_o Q + \frac{1}{2}\left(\frac{d^2U}{dQ^2}\right)_o Q^2 + \text{anharmonic terms} \qquad (2.2)$$

The anharmonic terms contain additional nonvanishing derivatives of $U(Q)$. The first derivative of $U(Q)$ is zero at R_0. Neglecting anharmonic contributions, the potential is quadratic in Q:

$$U(Q) \approx \frac{1}{2}kQ^2, \ k = \left(\frac{d^2U}{dQ^2}\right)_o. \qquad (2.3)$$

In classical mechanics, two atoms of mass m_a and m_b interacting with this potential vibrate sinusoidally at frequency

$$\omega = (k/\mu)^{1/2} \qquad (2.4)$$

where μ is the reduced mass:

$$\frac{1}{\mu} \equiv \frac{1}{m_a} + \frac{1}{m_b}. \qquad (2.5)$$

The Schrödinger equation describes the wavefunction for two particles interacting by the quadratic potential in Equation 2.3.

$$\nabla^2\Psi + \frac{2m}{\hbar}\left[E - \frac{1}{2}kQ^2\right]\Psi = 0 \qquad (2.6)$$

The solution is an energy spectrum with equally-spaced energy levels:

$$E_v = \left(v + \frac{1}{2}\right)\hbar\omega, \ v = 0,1,2,\dots. \qquad (2.7)$$

The wavefunctions are sketched in Figure 2.3. In the ground state the nuclei are most likely to be found at separation $Q=0$, *i.e.*, at their equilibrium separation, $R = R_0$. At higher levels of excitation the nuclei are most likely to be found at the limits of their oscillation (largest and smallest R). In classical mechanics a simple harmonic oscillator spends most of its time at the positions of greatest displacement where the velocity is lowest. The similarity of the quantum mechanical and classical behaviors for high quantum numbers is known as the correspondence principle.
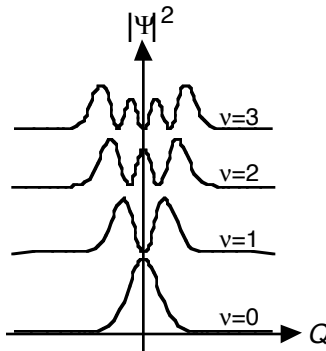
Figure 2.3 Squares of the wavefunctions of the harmonic oscillator (offset for clarity). At successively higher vibrational excitations (higher v), the nuclei are more and more likely to be found at large separation, in agreement with a classical harmonic oscillator.

The harmonic approximation is a good representation of the interaction potential at low levels of excitation where the Taylor series (2.2) remains a good approximation to the actual interaction potential. The harmonic approximation is particularly valuable because it has an exact solution.

Another expression for the interaction potential which has an exact solution is the Morse potential[10]:

$$U(Q) = D_e \left(1 - e^{-\alpha Q}\right)^2.$$
(2.8)

This is the function sketched in Figure 2.1; it increases rapidly at small separation and disappears at large separation. The energies of the bound states in a Morse potential are

$$E_v = \left(v + \frac{1}{2}\right)\hbar\omega - \left(v + \frac{1}{2}\right)^2 \hbar\omega x.$$
(2.9)

The constant x depends on D_e and α. The second term is a correction to the energy of a harmonic oscillator (32). We stress that Equations 2.7 and 2.9 are the just the energies of states of the artificial potential energy surfaces (2.3, 2.8) used in these calculations. Real molecular spectra depend on the actual interaction potential between the atoms.

2.3 Electronic transitions in diatomic molecules

Electronic transitions are often depicted in potential energy *versus* nuclear separation diagrams such as Figure 2.4. The Figure shows an electronic ground state potential energy surface, X, and the potential energy surface corresponding to an excited electronic state, A. In this example, the excited state A has a minimum at larger R than the ground state. An arrow represents a transition from X→A. The transition is vertical in this diagram because electronic transitions occur much faster than nuclear motion, R.

The most probable transitions are between vibrational states with probability maxima at the same R. This is called the Frank-Condon principle. At high levels of vibrational excitation, the molecule is most likely to be found towards the limits of the oscillation, while in the ground state the probability distribution is concentrated near $R = R_0$ (Figure 2.3). The vertical transition in Figure 2.4 satisfies the Frank-Condon principle because it is a transition from the equilibrium position in the ground state to an extreme limit of motion in an excited (vibrational) state.
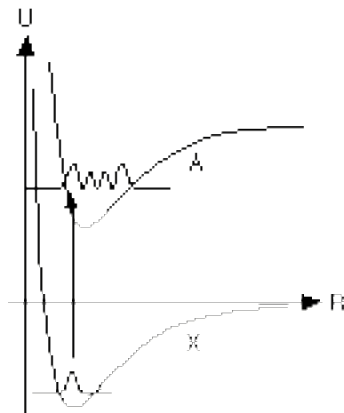
Figure 2.4 A transition between the electronic ground state of a molecule, X, and an excited electronic state, A. The displacement of these (hypothetical) potential energy surfaces ensures that the ground state wavefunction overlaps well with an excited vibrational state wavefunction. The transition shown satisfies the Frank-Condon principle.

Spectra of molecules are further complicated by rotational excitations. Transitions between rotational states lie in the microwave region of the spectrum; transitions between vibrational states lie in the infrared region of the spectrum, and electronic transitions span the range from infrared through visible to the ultraviolet.

Additional details to this brief introduction are provided below as some of the concepts are applied to the study of chemical reaction of adsorbates at metal surfaces.

2.4 Structure of solids

The atoms in a metal or semiconductor form an approximately regular three-dimensional pattern. Common arrangements of the atoms include face centered cubic (FCC) and body centered cubic (BCC), depicted in Figure 2.5, though many others are also common. [11] The energies of the states occupied by valence electrons depend on the arrangements of the atoms because valence electrons from neighboring atoms interact. The states of the valence electrons determine many properties of solids.
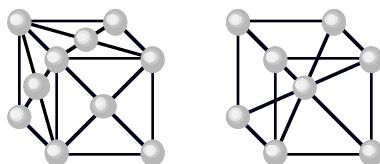
Figure 2.5 The face centered cubic (FCC, *left*) and body centered cubic (BCC, *right*) crystal structures. Not all the atoms are visible. The actual crystal is comprised of many of these cubes packed next to each other so that the atoms in the corners are shared by eight different cubes.

The wavefunction of an electron in a crystal is determined by the Schrödinger Equation 8 with $U(\bar{r})$ representing the potential of the charges in all the atoms. The equation cannot be solved analytically unless the real $U(\bar{r})$ is replaced with a simple function. Here we consider simple models to obtain a qualitative understanding of electronic states of solids.

2.5 Free electron states

We begin by considering free electrons for which $U(\bar{r}) = 0$. In the free electron model the Schrödinger equation yields a parabolic relationship between kinetic energy and momentum:

$$E = \frac{\langle p \rangle^2}{2m}. \tag{2.10}$$

This equation is called a dispersion relation; it relates the energy of the electron to its momentum. The momentum of the free electron can take on any positive value, and hence the energy of the electron can be anywhere from zero to infinity. Equation 2.10 is represented in Figure 2.6 for a one dimensional crystal.

When $U(\bar{r})$ is not zero, a theorem known as Bloch's theorem constrains the electronic wavefunction. The theorem applies to electronic states in a periodic potential $U(\bar{r})$ where

$$U(\bar{r} + \bar{R}) = U(\bar{r}) \tag{2.11}$$

for all $\bar{r}$. The vectors $\bar{R}$ which satisfy (2.11) are called lattice vectors. Bloch's theorem states that when (63) is satisfied there exists a vector $\bar{k}$ such that

$$\Psi(\bar{r} + \bar{R}) = e^{i\bar{k} \cdot \bar{R}} \Psi(\bar{r}). \tag{2.12}$$

This equation says that between points in the crystal separated by a lattice vector $\bar{R}$, only the (complex) phase of the wavefunction may change. Wavefunctions in a periodic potential satisfy (2.12) and are called Bloch wavefunctions. [11, 12]
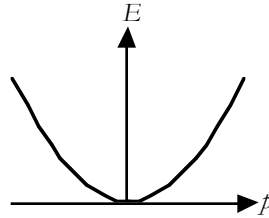
Figure 2.6 The parabolic dependence of energy on momentum for a free electron.

The quantity $\hbar\bar{k}$ is known as the crystal momentum. There are special values of the crystal momentum called reciprocal lattice vectors, $\bar{K}$, that satisfy

$$\vec{R} \cdot \vec{K} = 2\pi n, \tag{2.13}$$

where n is an integer. We may write a general $\vec{k}'$ in terms of $\vec{K}$:

$$\vec{k}' = \vec{k} + \vec{K}. \tag{2.14}$$

When this expression is substituted into (2.12), the definition (2.13) ensures that the factor containing $\vec{K}$ is 1:

$$\begin{aligned}
\Psi(\vec{r} + \vec{R}) &= e^{i\vec{k}' \cdot \vec{R}} \Psi(\vec{r}) \\
&= e^{i(\vec{k} + \vec{K}) \cdot \vec{R}} \Psi(\vec{r}) \\
&= e^{i\vec{k} \cdot \vec{R}} \Psi(\vec{r})
\end{aligned} \tag{2.15}$$

Equation 2.15 is the same as Equation 2.12. Therefore, two crystal momenta, $\vec{k}'$ and $\vec{k}$, which differ by a reciprocal lattice vector, $\vec{K}$, place the same constraints on the Bloch wavefunction. We therefore restrict attention to a small set of $\vec{k}$ values called the first Brillouin zone, comprised of those $\vec{k}$ whose magnitude cannot be made smaller by addition of a reciprocal lattice vector.

Bands are typically drawn only within the first Brillouin zone. Figure 2.7 shows an example in one dimension. The wave vectors $\vec{k}'$ and $\vec{k}$ differ by a reciprocal lattice vector of length $2\pi/a$. The horizontal arrows represent translations of the bands back into the first Brillouin zone. This representation is called the reduced zone scheme.
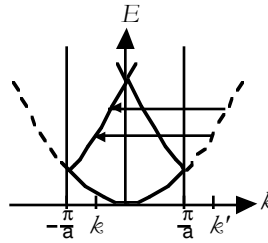
Figure 2.7 Wavevectors which differ by a reciprocal lattice vector (such as k and k') are physically equivalent. This motivates translating (represented by the horizontal arrows) the portions of the band that lie beyond $2\pi/a$ to produce a reduced zone representation.

In a real crystal, the first Brillouin zone has a three-dimensional shape that reflects the symmetry of the real three-dimensional crystal lattice. Figure 2.8 depicts the first Brillouin zone of a FCC crystal. Conventional labels for points of high symmetry on the surface are indicated. There are many points on the surface that are equivalent to the labeled points because of the symmetry of the first Brillouin zone (and the crystal). The center of the polygon, $\bar{k} = 0$, is known as the *Γ-point*.
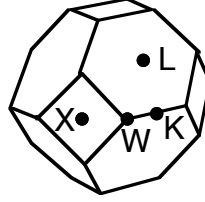
Figure 2.8 The first Brillouin zone of a FCC crystal. This is a figure drawn in three-dimensional *k*-space. The origin, $\bar{k} = 0$, is located at the center of the polygon and is called the Γ-point. Other points of high symmetry on the outer surface of the figure are labeled with letters as shown.

In a three-dimensional crystal, the $\bar{k}$ are three-dimensional and a graph of the band structure can no longer represent the states at all $\bar{k}$. Instead, the bands are shown along particular directions in $\bar{k}$-space. Figure 2.9 shows the band structure for free electrons in a FCC lattice in the directions of highest symmetry. The horizontal axis uses labels defined in Figure 2.8. Some locations in *k*-space (such as the Γ-point) are represented more than once. For example, the band structure is represented along three different paths from the Γ-point to the edge of the Brillouin zone: Γ↔X, Γ↔L, and Γ↔K.
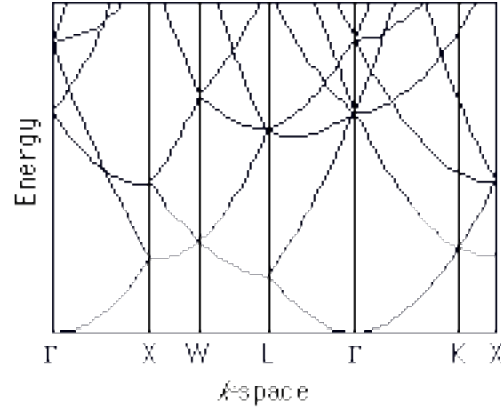
Figure 2.9 Free electron states for a FCC crystal. The states are plotted against representative directions in k-space. High symmetry positions in k-space are labeled with letters defined in Figure 2.8.

At the Γ-point, for energies near $E = 0$, the bands in Figure 2.9 have the quadratic dependence of Equation 2.10. When the bands reach the first Brillouin zone boundary (at X, L, or K for example), they are translated back into the first Brillouin zone, producing an apparent reflection of the parabolic shapes about the X, L, and K points. This reflection is analogous to that sketched in Figure 2.7 for a one-dimensional crystal.

The shape of the parabola depends on the particular path chosen in k-space. According to the dispersion relation (2.10), the energy of free-electron states depends on the square of the magnitude of $\bar{k}$. This fact explains the kink in the graph at L between Γ and W: the distance from the Γ-point increases more quickly between Γ and L than between L and W, as apparent in Figure 2.8. Throughout Figure 2.9, the bands reflect the dispersion relation for free electrons and the geometry of the first Brillouin zone.

The bands are not necessarily occupied with electrons. They cannot all be filled because the number of electrons in the crystal is finite, whereas there are infinite states available in the band structure. The probability that a state of energy E is occupied is given by the Fermi-Dirac function, [11]

$$f(E) = \frac{1}{e^{(E-E_F)/k_B T} + 1}, \tag{2.16}$$

14

where E_F is the Fermi energy, k_B is the Boltzmann constant, and T is the electron temperature. At $T = 0$, the Fermi-Dirac function is a step function: states below the Fermi energy are occupied and states above the Fermi energy are empty. At real temperatures the transition is smoother, as depicted in Figure 2.10. A Fermi-Dirac distribution is valid only when the electrons are in thermal equilibrium and temperature is well-defined. [12] Electrons out of thermal equilibrium are considered in the section on electron-electron scattering below.
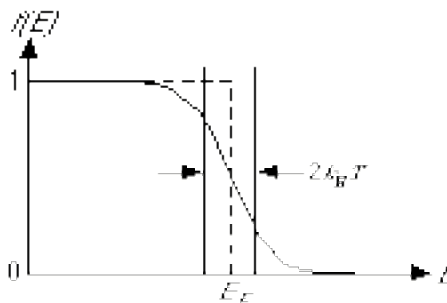
Figure 2.10 The Fermi-Dirac function at $T = 0$ (dashed line) and $T = 0.1E_F$ (solid line). The transition between $f(E) = 1$ and $f(E) = 0$ occurs over an energy range of approximately $2k_BT$.

In this section we have applied Bloch's theorem to determine how the symmetry of the crystal governs the electronic band structure. We have also assumed that the electrons are free, $U(\vec{r}) = 0$. These assumptions are, strictly speaking inconsistent. We see below, however, that when $U(\vec{r})$ is small but nonzero, the band structure resembles the free electron band structure. An excellent approximation of the band structure is obtained by applying only our knowledge of the symmetry of the crystal potential, (63) ignoring any interaction of electrons with the lattice.

2.6 Beyond free electron states

In a real crystal the electrons interact with the periodic potential of the lattice. The simplest band structures occur in metals where $U(\vec{r})$ is small. Recall that monovalent metals have a single electron outside a filled shell (or a filled sub-shell, such as Cu) and that

this electron is shielded from the nucleus by its interactions with the other electrons. The shielding leads to relatively weak interactions with the lattice and small $U(\bar{r})$ compared to other crystals. We expect the band structure of monovalent metals such as K and Cu to be approximately the band structure of free electrons.

Figure 2.11 is a graph of the solution to the Schrödinger equation obtained from perturbation theory[13] with the weak periodic potential $U(\bar{r})$. The influence of the interactions with the lattice is to segment and distort the free-particle solution (Figure 2.7). The distortion occurs near the Brillouin zone boundary; in other regions the bands remain parabolic. Alkali metals have bands which are very similar to Figure 2.11.
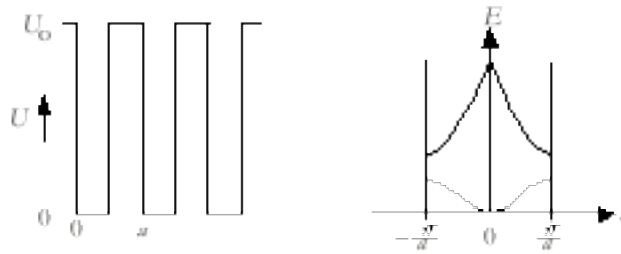
Figure 2.11 A periodic potential in one dimension (*left*) and the corresponding bands (*right*).

In other metals, there are often bands with free-electron character. For example, the bands of aluminum (configuration [Ne] $3s^23p^1$) depicted in Figure 2.12 are very similar to free electron bands. Copper, with configuration [Ar] $3d^{10}4s^1$, has a more complicated band structure. The band structure of copper in Figure 2.13 has both horizontal and parabolic bands. The roughly horizontal bands arise from electrons in *d*-orbitals. The bands are horizontal because *d*-orbital electrons from one atom interact strongly with neighboring atoms, as expected from the graph of the spatial distribution of *d*-orbitals in Figures 3 and 5. The roughly parabolic bands in Figure 2.13 arise from the electrons in *s*-orbitals. The *s*-orbital electrons interact less with the lattice than the *d*-orbitals because of the small radial extent of *s*-orbitals. The parabolic bands in Figure 2.13 are similar to the free electron bands in Figure 2.9.
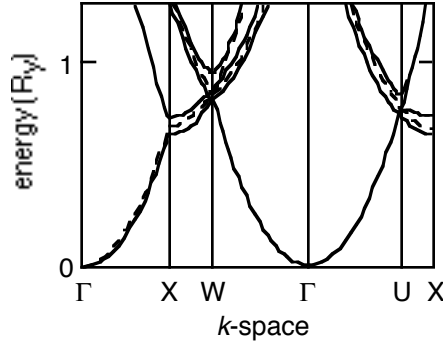
Figure 2.12 The band structure of aluminum has a lot of the parabolic character of free-electron bands. The dashed lines indicate the free electron bands. After [14]
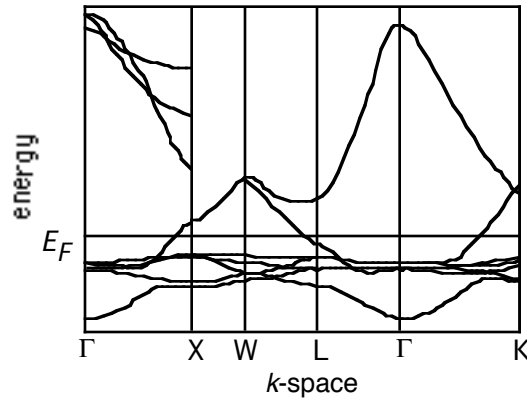
Figure 2.13 The calculated band structure of copper in a portion of *k*-space. Both parabolic free-electron-like bands and roughly horizontal *d*-bands are present. After [15].

The band structures of *d*-band metals share a number of features. Compare, for example, the band structure of copper in Figure 2.13 with the band structure of platinum shown in Figure 2.14. At low energy near the Γ-points, the quasi-free electron bands are similar because they are both FCC crystals. The Fermi levels of platinum and copper are at different locations with respect to the bands. In platinum (with configuration [Xe] $4f^{14}5d^{10}6s^0$) the Fermi level is in the horizontal *d*-bands, while in copper the Fermi level lies in the parabolic *s*-bands.
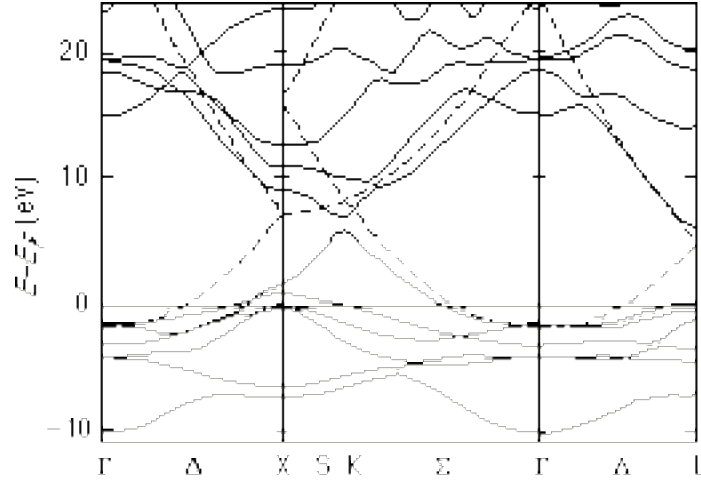
Figure 2.14 The calculated (solid lines) band structure of platinum. The dashed lines indicate the free electron bands for an FCC crystal. After [16]

2.7 The dielectric function of metals

The interaction of light with the electrons in a material is represented by transition of electrons from occupied to unoccupied states in the band structure. According to the Fermi-Dirac function, Equation 2.16, unless the temperature is very high, occupied states are below the Fermi level, and unoccupied states are mostly above the Fermi level. If the initial and final states of the electron are in the same band, the transition is intraband. If the transition is from one band to another, the transition is interband. In both cases, the transition is from below the Fermi level to above the Fermi level. Figure 2.15 shows an interband transition in the band structure of an alkali metal.
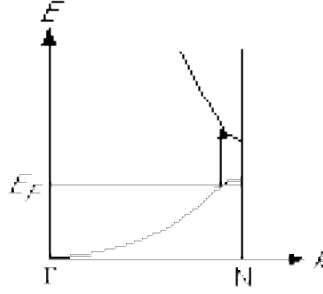
Figure 2.15 The band structure of an alkali metal, with an interband transition indicated. In an intraband transition (not shown) the initial and final states of the electron lie in the same band. After [12]

In both intraband and interband transitions, the crystal momentum is conserved. When the crystal momentum of the electron changes, as it must in an intraband transition, one or more other bodies must have an opposite change in crystal momentum. The photon does not contribute to conservation of crystal momentum because photons have negligible momentum. Phonons, on the other hand, do have crystal momentum, and intraband transitions are usually accompanied by excitation of a phonon so that the total change in crystal momentum of the phonon and the electron is zero. Phonons are discussed in section 2.9.

The imaginary part of the dielectric function of several alkali metals is shown in Figure 2.16. To explain the low energy behavior of $\varepsilon(\omega)''$, we must consider low-energy, intraband transitions in the lower parabolic band of Figure 2.15. Electrons in parabolic bands behave as free electrons (see Figure 2.6). One can show free electrons create a $\varepsilon(\omega)''$ that drops with increasing frequency.[11] The dielectric function of alkali metals is similar to the dielectric function of free electrons because the band structure is nearly parabolic near the Fermi level.
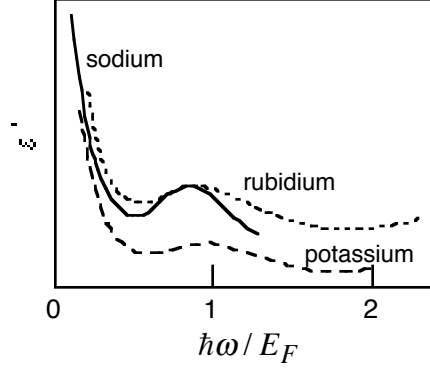
Figure 2.16 The experimentally determined imaginary parts of the dielectric function for the alkali metals. They are similar because the band structures are similar. After [12]

The dielectric functions in Figure 2.16 do not monotonically decrease. The increase in $\varepsilon(\omega)''$ near $\hbar\omega/E_F = 0.65$ is attributed to the onset of interband transitions at energies sufficient to excite electrons across the gap between bands. The lowest energy interband transition (at constant crystal momentum) is shown in Figure 2.15. There are no transitions at the Brillouin zone boundary because there are no electrons at the **N**-point: the Fermi level is below the energies of the states at the **N**-point. The length of the arrow in Figure 2.15 is about $0.65\ E_F$. The onset of interband transitions accounts for the rise in $\varepsilon(\omega)''$ in Figure 2.16 near $\hbar\omega/E_F = 0.65$.

Figure 2.17 shows the measured real and the imaginary parts of the dielectric function of platinum. [17] Overall, $\varepsilon(\omega)''$ falls with increasing energy — the expected free electron contribution to $\varepsilon(\omega)''$. The structure at about 0.8 eV, is attributed to the onset of interband transitions near the **X** point in the platinum band structure, Figure 2.14. [18]
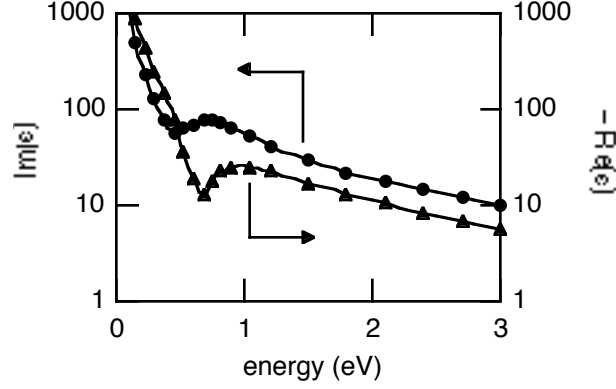
Figure 2.17 The dielectric function of platinum. The features at about 3/4 eV can be attributed to the band structure. Data from [17].

2.8 Electron-electron scattering

The electrons in a material do not necessarily have a distribution of energies described by the Fermi-Dirac equation. During absorption of light, for example, electrons acquire energies far in excess of $k_B T$. This energy is partitioned among all the electrons by collisions between electrons, until the distribution of electron energies is a Fermi-Dirac distribution. Fermi liquid theory predicts the rate at which a single electron excited above the Fermi level collides with another electron. One of the aims of the model is to predict the rate at which the excited electron scatters with other electrons.

Consider the collision of an excited electron of crystal momentum $\bar{k}_1$ with an electron of crystal momentum $\bar{k}_2$, depicted in Figure 2.18. The scattering rate depends on the probability of finding an electron of momentum $\bar{k}_2$, and also on the probability that there are empty states of momenta $\bar{k}_1{}'$ and $\bar{k}_2{}'$. In Fermi liquid theory it is assumed that, except for the single excited electron in question, the distribution of electron energies is described by the Fermi-Dirac function, Equation 2.16. With this assumption we can write the scattering rate as:

$$\frac{1}{\tau} \propto f\left(\bar{k}_2\right)\left[1 - f\left(\bar{k}_1{}'\right)\right]\left[1 - f\left(\bar{k}_2{}'\right)\right]. \tag{2.17}$$

This is the scattering rate for a particular $\vec{k}_1{}'$ and $\vec{k}_2{}'$. The scattering rate into all possible final states $\vec{k}_1{}'$ and $\vec{k}_2{}'$ depends on the total number of available states for $\vec{k}_1{}'$ and $\vec{k}_2{}'$.
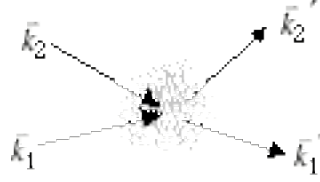
Figure 2.18 A binary collision between two electrons.

We estimate the number of available states when the temperature is zero Kelvin. The calculation begins with some observations about the relative energies of the electrons before and after the collision. Figure 2.10 implies that the final states $\vec{k}_1{}'$ and $\vec{k}_2{}'$ must satisfy $E(\vec{k}_1{}') > E_F$ and $E(\vec{k}_2{}') > E_F$ because all the available (empty) states are above the Fermi level. The figure also implies that $E(\vec{k}_2) < E_F$ because the electron $\vec{k}_2$ must begin in an occupied state. Since the collision increases the energy of the electron $\vec{k}_2$, the energy of the electron $\vec{k}_1$ must decrease to conserve energy: $E(\vec{k}_1{}') < E(\vec{k}_1)$. By a similar argument, the final energy of the electron $\vec{k}_2$ must be less than the initial energy of the excited electron: $E(\vec{k}_2{}') < E(\vec{k}_1)$. Both electrons end up with energies between E_F and $E(\vec{k}_1)$.

The number of available states between E_F and $E(\vec{k}_1)$ is proportional to $\left| |\vec{k}_1| - |\vec{k}_F| \right|$. Substituting this expression into (2.17) gives a scattering rate:

$$\frac{1}{\tau} \propto \left(|\vec{k}_1| - |\vec{k}_F| \right)^2. \tag{2.18}$$

This expression is valid when $T = 0$ and the initially excited electron $\vec{k}_1$ is near the Fermi level. Equation 2.18 shows that the lifetime of an electron becomes very large as the electron gets close to the Fermi level. Calculations of the scattering rate give electron-electron scattering times of 10 fs for an electron which lies 2 eV above the Fermi surface, and 1 ps for an electron which lies 0.2 eV above the Fermi surface. Equation 2.18 is often stated in terms of energy:

$$\frac{1}{\tau} \propto \left[E(\vec{k}_1) - E_F \right]^2. \tag{2.19}$$

Equations 2.18 and 2.19 are equivalent for energies close to the Fermi level.

At small (nonzero) temperatures the total number of states available for the electrons to scatter to depends on temperature. To calculate the scattering rate, we note that Figure 2.10 shows that the Fermi-Dirac distribution changes from 1 to 0 over a range of energies of order $k_B T$. If the target electron is to scatter into an available (empty) state, it must have an initial energy within the range $k_B T$ of E_F. Similarly, the number of available states scales as $k_B T$. Once the initial and final energies of the target electron are specified $E(\vec{k_1}')$ is known because of energy conservation. The scattering rate depends the square of the temperature:

$$\frac{1}{\tau} \propto (k_B T)^2. \tag{2.20}$$

In practice, the scattering of electrons with energy close to E_F is dominated by scattering with phonons (see below) or impurities, and the quadratic dependence of scattering rate on temperature is not observed. [12]

2.9 Phonons

In the previous two sections we assumed the ionic lattice to be fixed and immobile. In this section we consider collective motions of the ions. The ions can be displaced from their equilibrium positions and such disturbances can travel through the solid in the form of phonons which play an important role in the electronic and optical properties of solids because they can interact directly with electromagnetic waves.

Let us begin by considering a linear chain of identical atoms separated by a spacing a as illustrated in Figure 2.19. The top of the drawing shows the atoms in their equilibrium position; at the bottom the atoms are displaced from their equilibrium position. Let us assume that only nearest neighbors exert forces on each other and that the interionic force obeys Hooke's law. The forces exerted on ion n by its two nearest neighbors are thus

$$F_{n-1,n} = \gamma(u_{n-1} - u_n)$$
$$F_{n+1,n} = \gamma(u_{n+1} - u_n) \tag{2.21}$$

where γ is the force constant. The equation of motion for the ion is then

$$m\frac{d^2u_n}{dt^2} = \gamma\left[u_{n-1} + u_{n+1} - 2u_n\right]. \tag{2.22}$$
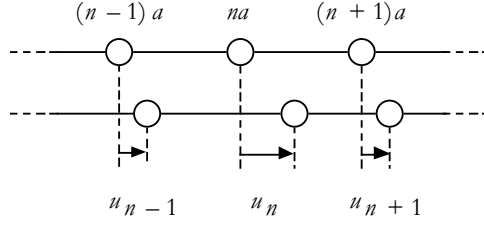
Figure 2.19 Vibrating linear chain of identical atoms spaced by distance *a*.

We look for solutions in the form of a traveling harmonic displacement wave (called a normal mode)

$$u_n(t) = Ae^{i(qna - \omega t)}, \tag{2.23}$$

where A is the amplitude of the displacement wave, q the wavevector, and ω the angular frequency. Substituting this into Equation 2.22 we get

$$-m\omega^2 = \gamma[e^{-iqa} + e^{iqa} - 2] = -4\gamma\sin^2\left(\frac{qa}{2}\right), \tag{2.24}$$

so
$$\omega = \sqrt{\frac{4\gamma}{m}}\left|\sin\frac{qa}{2}\right|. \tag{2.25}$$

As Figure 2.20 shows, we only need to consider displacement waves of wavelength larger than $2a$ — due to the discreteness of the chain, all waves of shorter wavelengths are equivalent to certain waves of longer wavelengths. This means we can restrict our analysis to small wavevectors:

$$\lambda \geq 2a \quad \Rightarrow \quad q \leq \frac{\pi}{a}. \tag{2.26}$$
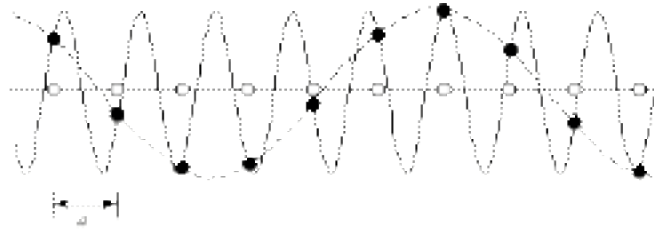
Figure 2.20 Oscillating chain of atoms showing instantaneous displacements. The solid curve conveys no information not given by the dashed one.

Figure 2.21 shows the dependence of the displacement frequency on wavevector q (77). For small wavevector, Equation 77 becomes linear in the wavevector

$$\omega = \sqrt{\frac{4\gamma}{m}}\frac{qa}{2} = \sqrt{\frac{\gamma a}{m/a}}q = v_s q, \tag{2.27}$$

with v_s the speed of sound. This is the relation one would obtain if the chain were continuous rather than discrete (when a approaches zero, π/a goes to infinity and the dispersion relation becomes linear throughout). The dispersion of waves near the edge of the Brillouin zone at π/a is therefore a direct consequence of the granularity of the chain.

In a two-atom linear chain the situation is more complicated because the atoms of different kind can either move in phase (such displacement waves are called acoustic phonons) or out of phase (optic phonons). Figure 2.22a illustrates the displacements that occur for transverse acoustic (TA) and optic (TO) phonons of small wavevector. While both displacements have the same large wavelength, the potential energy associated with the optic phonon is larger because the interatomic bonds are much more distorted. The dispersion relation now has two branches (see Figure 2.23a); for low wavevector the acoustic branch approaches zero, but because of the large distortion at low frequency, the corresponding energy for the optic branch is nonzero at zero wavevector.
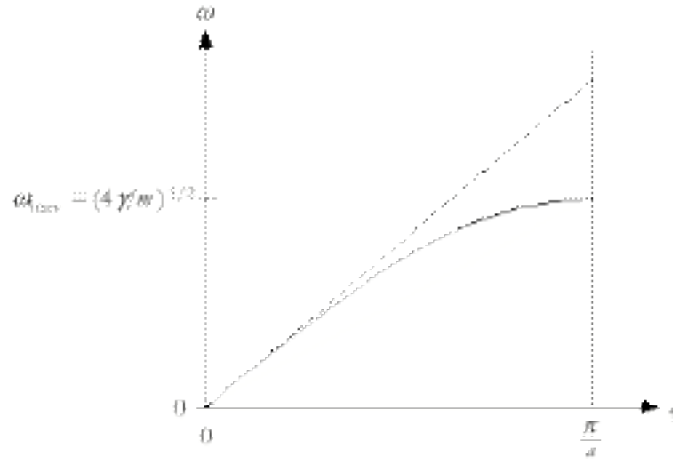
Figure 2.21 Dispersion of waves along a linear chain of atoms. The dashed line shows the result one would obtain for a continuous medium. The slope of the dashed line corresponds to the speed of sound waves in the medium.

Figure 2.22*b* shows the displacements for the acoustic and optic phonons of the shortest possible wavelength ($\lambda = 2a$). The corresponding energies (see Figure 2.23*a*) are slightly different. Figures 2.22*c* and 2.22*d* show how the cases illustrated in Figures 2.22a and 2.22*b* relate to single-atom chain phonons: the optic branch vanishes as low wavevector optic phonons map onto large wavevector acoustic phonons. Note, in particular that the low-*q* TO phonon for the two-atom chain maps to a high-*q* TA phonon on the one-atom chain (*cf.* Figures 2.22*a* and *c*). Similarly, the TO and TA phonon modes at the edge of the Brillouin zone for the two-atom chain, are identical on the one-atom chain (*cf.* Figures 2.22*b* and *d*), but are now in the middle of a Brillouin zone that is twice as wide (Figure 2.23*b*).
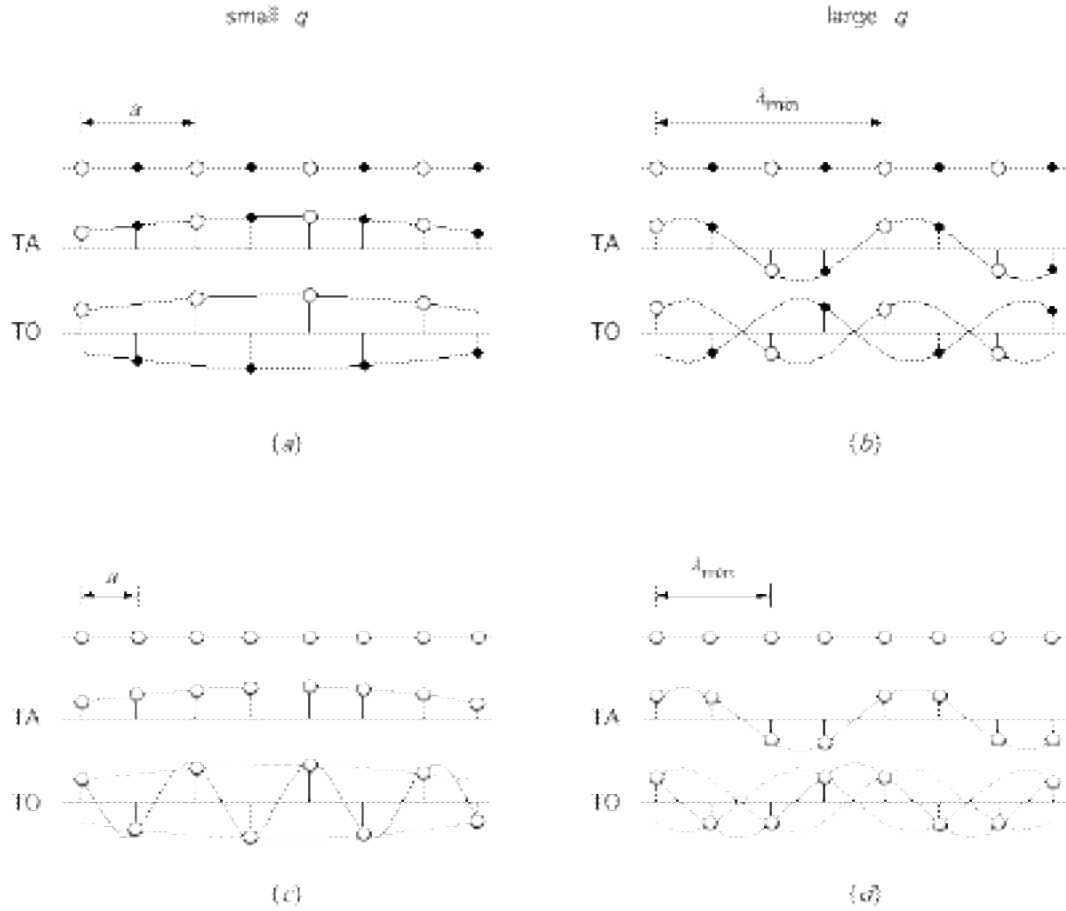
Figure 2.22 Waves on two-atom linear chains. Displacements are shown for (*a*) small and (*b*) large wavevector. The in- and out-of-phase waves correspond to acoustic and optic phonons, respectively. The bottom to graphs (*c* and *d*) show how the waves for a two-atom chain map onto waves of different wavevector for a one-atom chain.

2.10 Electron-phonon interaction

The Bloch wavefunctions (2.12) are solutions to the Schrödinger equation only when the lattice is perfectly well ordered. In practice phonons cause a distortion of the lattice. The distortion allows electrons to make transitions between Bloch states. This process is described as a scattering of an electron with a phonon, and can either transfer energy to the phonon or to the electron.
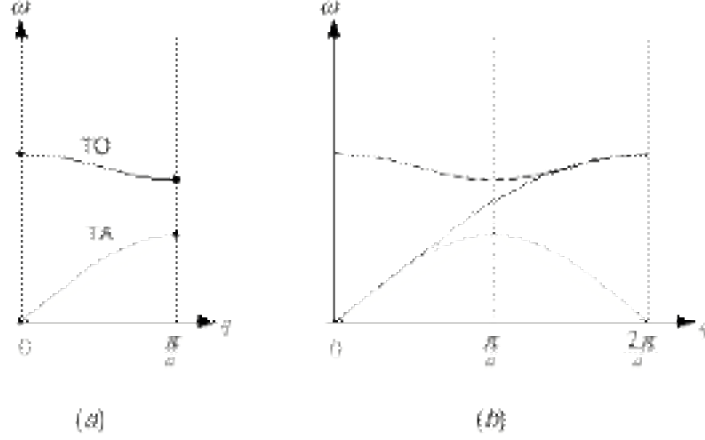
Figure 2.23 Dispersion relation for phonons (*a*) on a two-atom linear chain and (*b*) on a corresponding one-atom linear chain.

We consider a phenomenological treatment of this scattering relevant when the electrons have been very highly excited by a laser pulse. For example, when a subpicosecond laser pulse with photon energy of about 2 eV strikes a metal surface, the energy is absorbed by the electrons. The electrons share this energy among themselves by electron-electron collisions (see above), reaching a Fermi-Dirac distribution. Simultaneously, the electrons scatter with phonons, effectively heating the metal. The spatial variation in the deposited laser energy creates a complication: the energy diffuses away from the surface towards the bulk.

These ideas are expressed in a model for the response of a metal to ultra-fast photo-excitation. [19, 20] This model states that the temperatures of the electrons, T_e, and phonons (the lattice), T_l, evolve according to:

$$C_e(T_e)\frac{\partial T_e}{\partial t} = \kappa(T_e)\frac{\partial^2 T_e}{\partial x^2} - g(T_e - T_l) + A(x,t)$$

$$C_l(T_l)\frac{\partial T_l}{\partial t} = g(T_e - T_l)$$

(2.28)

where $A(x,t)$ is the energy deposited by the laser and C_e and C_l are the heat capacities of the electrons and the lattice. The constant g determines how quickly the electrons and phonons equilibrate with each other. The first equation contains a term describing the

diffusion of the electrons. The energy carried by phonon diffusion is small compared with that due to electron diffusion in a metal; phonon diffusion is neglected in this model. The constants are approximately known, and so the electron and lattice temperatures can be found by numerical solution of Equation 2.28.

Figure 2.24 shows the evolution of the electron and lattice temperatures at the surface of platinum following excitation by a 32 μJ/mm^2, 800-nm pulse. Initially the sample is in thermal equilibrium at 90 K. The laser pulse causes a large transient rise in the surface electron temperature followed by equilibration of the electron and lattice temperatures in a few picoseconds.
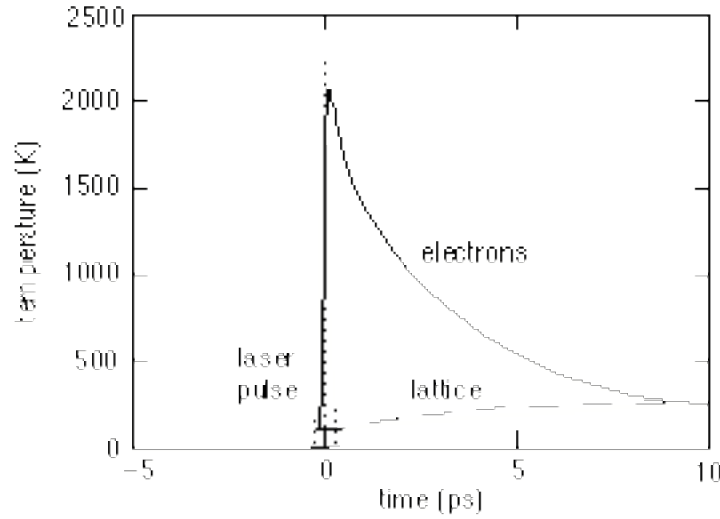
Figure 2.24 Calculated evolution of electron and lattice temperatures following excitation of platinum with a 100-fs, 32 μJ/mm^2, 800-nm laser pulse.

This model assumes that the electrons are always thermalized with each other — that they satisfy a Fermi-Dirac distribution at all times. In reality the laser pulse excites electrons far above the Fermi level and a finite time is required for the electrons to thermalize. For example, 800 nm photons have 1.6 eV energy, while at 90 K, $k_BT \approx 8$ meV. Numerous experiments have examined the relaxation of the photo-excited electrons to a Fermi-Dirac distribution. [21-24]

2.11 Photoemission spectroscopy

One of the most direct experimental methods for determining electronic states is photoemission spectroscopy, illustrated in Figure 2.25. Light stimulates an electron in a solid. If the electron is sufficiently excited, it escapes the material with energy

$$E_k = \hbar\omega - \Phi - E_i. \qquad (2.29)$$

The energy of the photo-emitted electron depends on the initial photon energy, $\hbar\omega$, the initial state energy, E_i, and the energy required to extract the electron from the material, Φ, known as the work function. By measuring E_k, the energy of the initial state can be inferred. Generally electrons are emitted over a range of electron energies corresponding to the range of occupied states in the band structure, and the electrons comprise a photoelectron spectrum, as sketched in Figure 2.25.
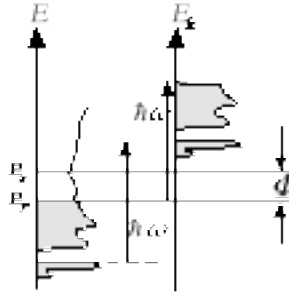
Figure 2.25 In photoemission spectroscopy the kinetic energy, E_k, of the emitted electron (right side of figure) depends on the initial state of the electron (left side of figure), the photon energy, and the work function. After [25].

The states that are probed in a photoemission experiment depend on the source of the initial excitation. Figure 2.26 depicts the some of the features which are observed with different excitation sources.

When the photon energy is low, the electrons may not receive enough energy from a single photon to overcome the work function of the material, but may escape if stimulated by two photons. This two-photon photoemission, or TPPE, is used to study the electronic states which lie between the Fermi level and the vacuum level. Because these states are

above the Fermi level, the electrons rapidly scatter out of these states; TPPE using short pulses can therefore be used to study the dynamics of electron relaxation. Another way to study states between the Fermi level and the vacuum is to apply a strong DC electric field to the sample surface. The potential barrier between an electron at the surface and a free electron in vacuum can be overcome if the applied field is sufficiently large.
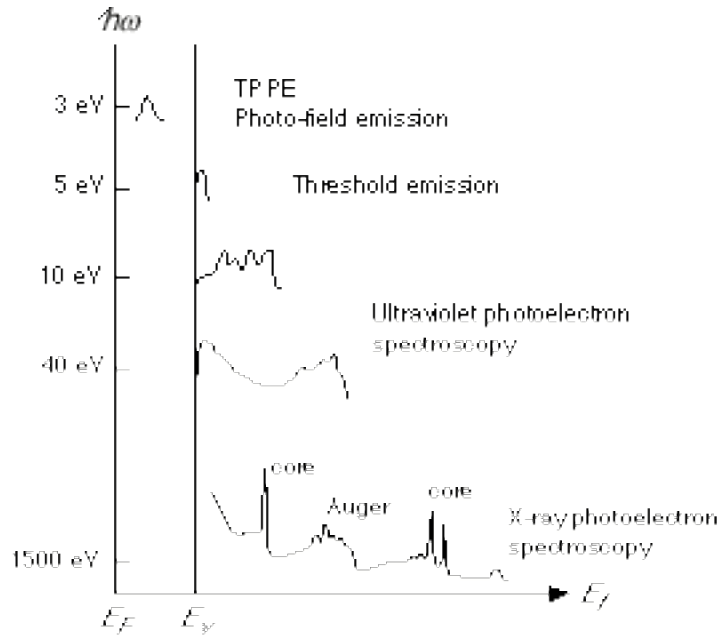
Figure 2.26 The photoelectron spectrum depends on the energy of the exciting photon. X-rays are able to induce emission of core electrons and Auger electrons. After [25]

At the other extreme, x-ray photons with energies in the 1000–eV range can eject core-level electrons. The resulting vacancy in the core level may be filled by an electron from a valence level. The energy released by this transition from the valence level to the core level may be imparted to another valence electron which is then ejected from the material with an energy depending on the energy levels of the states involved. This process is known as Auger recombination. The photoelectron spectrum following x-ray excitation has peaks which directly reflect the energies of the core levels, and peaks which arise from Auger recombination and reflect the energies of the valence and core levels. Spectroscopic

techniques that rely on core-level ionization often use a monochromatic beam of electrons as the excitation source because electron-beam sources are conveniently produced in the laboratory from hot filaments.

The escape of an electron from the surface is not always as simple as depicted in Figure 2.25. The electrons may scatter and lose some of their energy. These collisions lead to a broad distribution of electron energies. When these electrons escape the surface, they are known as secondary emission. Secondary emission is observed as a broad feature at low E_k. The scattering of electrons accounts for the surface sensitivity of photoemission spectroscopy: only electrons emitted in the near surface region escape the material and are detected. The depth of the material that is probed with photoemission spectroscopy depends usually on the escape depth of the photoelectrons and not on the absorption length of the excitation source.

2.12 Preparation of single-crystal surfaces

Surface reactions are influenced by the chemical composition of the surface and the structure of the surface. To reduce the complexity, surface reactions are often studied on very clean, single-crystal surfaces. A single-crystal surface is cleaned in ultra-high vacuum (1 × 10^{-10} torr). Using the ideal gas law, one can calculate that at a pressure of 10^{-6} torr, approximately 1 s is required for every surface atom to be struck by a gas phase molecule. [26] Each such collision is an opportunity for a gas phase molecule to stick on the surface. Thus to maintain a surface clean for, say, 10^4 s a pressure near 10^{-10} torr is required.

The direction of the surface plane with respect to the lattice of a single crystal is specified by Miller indices. [11] Figure 2.27 shows examples of surfaces obtained from an FCC lattice. The (111) surface has a high density compared with the (100) surface. We concentrate our attention on the (111) surface of platinum, Pt(111).
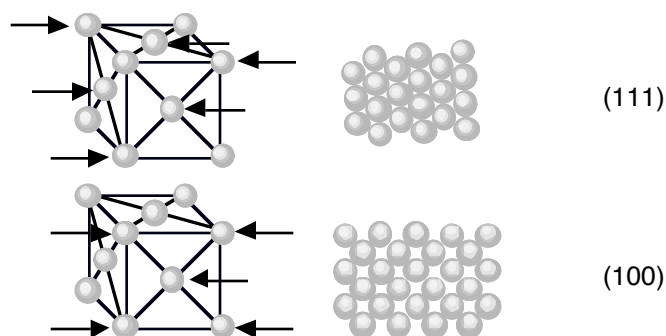
Figure 2.27 The (111) and (100) surfaces of an FCC crystal. The arrows indicate atoms in the crystal lattice which comprise the surface. In the diagrams of the crystals the spheres representing the atoms are not drawn to scale compared to the size of the cube.

Common procedures for cleaning a surface include annealing, and sputtering. The precise cleaning procedure is often determined by trial-and-error, using the diagnostic procedures described below to monitor the surface quality. As a starting point, there are compiled lists of the techniques that have been used to clean many crystals. [27]

When the sample is annealed in UHV (*i.e.* kept at elevated temperature for a certain time), some impurities simply desorb from the surface. For example, carbon monoxide desorbs from Pt(111) when the temperature exceeds about 300 K. Annealing may also provide the thermal energy required for surface atoms to rearrange themselves and correct small defects in the surface structure.

Sputtering is used to remove the first few layers of atoms from the surface. A noble gas, usually either neon or argon is admitted to the chamber. The gas is ionized and the ions are electrostatically accelerated to the surface. The ions dislodge material from the sample surface, including both the desired atoms and the impurities. This usually improves surface quality because impurities often cluster at the surface, particularly following annealing in vacuum or oxygen. Sputtering creates defects in the surface structure, so it is usually followed by annealing.

Pt(111) is usually cleaned by annealing in an oxygen atmosphere. During annealing, impurities such as silicon diffuse to the surface where they may bind with an oxygen atom, becoming trapped at the surface as an oxide. When these oxides are removed by sputtering, the density of impurities in the near-surface region is reduced. Annealing in oxygen also reduces carbon contamination because the carbon reacts to form carbon monoxide which desorbs from the surface.

2.13 Adsorption of reactants

There are two classes of interaction between a molecule and a surface. Chemisorption refers to a molecule or atom attached on a surface by a chemical bond. Physisorption is a much weaker van der Waals interaction between a molecule or atom and a surface. The energy which binds a chemisorbed species to a surface is typically 0.4–10 eV while physisorption energies are typically 0.01–0.1 eV.

To understand physisorption, picture a metal surface interacting with a polarized molecule or atom as shown in Figure 2.28. Whenever a charged species is placed near a metal surface its electric field causes an image charge in the metal. [28] The image charge is positioned so that the electric field produced by a charge and its image charge is identical to the field which would be produced by the charge and the true distribution of surface charge on the metal. Figure 2.28 depicts a polarized adsorbate as two charges separated by a distance u. The corresponding image charges are shown.
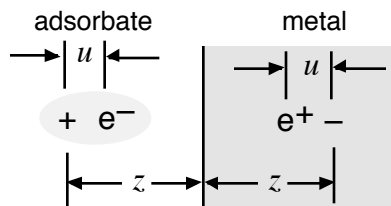
Figure 2.28 A polarized molecule or atom near a metal surface interacts with its image charges. After [26].

The interaction of the adsorbate with the surface may be determined by finding the total electrostatic (Coulomb) interaction between the charges in the adsorbate and the image charges in the metal:

$$U(z) = -\frac{e^2}{4\pi\varepsilon_0}\left[\frac{1}{2z} + \frac{1}{2(z-u)} - \frac{1}{(2z-u)} - \frac{1}{(2z-u)}\right] \qquad (2.30)$$

$$\approx -\frac{e^2}{4\pi\varepsilon_0}\frac{u^2}{z^3}.$$

On the right side of this equation, the interaction potential $U(z)$ is expanded into a Taylor series for small u/z. The interaction potential, Equation 2.30, is zero if there is no polarization, $u = 0$. Otherwise the interaction varies as $1/z^3$.

When the adsorbate is very close to the metal, the image charge model shown in Figure 2.28 is not accurate because the interaction becomes repulsive. When the repulsive interaction is balanced against the attractive interaction of Equation 2.30, the adsorbate typically settles $0.3 - 1.0$ nm from the surface in a shallow well. Physisorption is observed only at low temperatures. For example, O_2 will physisorb on Pt(111) at 45 K and form multiple physisorbed layers at 30 K. [29]

An adsorbate is chemisorbed if it forms a chemical bond with the substrate. The bond substantially changes the electronic states of the adsorbate. Figure 2.29 represents the energy levels of a molecule chemisorbed on a transition metal surface. The left side of the diagram represents the d-band of the transition metal. The right side represents a state of the free molecule. When the molecule chemisorbs on the metal surface the orbital of the molecule can mix with a d-orbital of the metal. The mixing is analogous to the formation of a bond between two atoms to make a molecule, Figure 2.1. The chemisorption of O_2 on Pt(111) is described in detail in section 2.17.
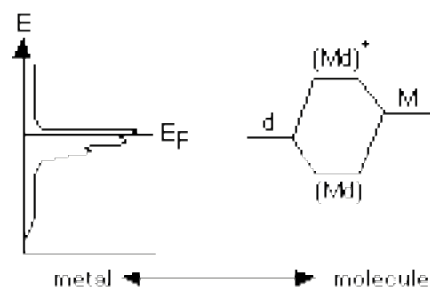
Figure 2.29 Chemisorption of a molecule on a metal surface is accomplished by mixing a *d*-orbital of the metal with an orbital of the molecule. Bonding (Md), and anti-bonding (Md)* orbitals are formed. After [26].

2.14 Surface diagnostics

In the discussion of photoemission spectroscopy, we mentioned that electrons may be emitted from an atom by Auger recombination following removal of a core-level electron. The energy of the Auger electron depends on the energies of electronic states of the atom; since these energies are unique to each atom, the Auger spectrum identifies the atoms present in the sample. Auger spectroscopy is one of the most common means of determining chemical composition of a surface. Figure 2.30 shows the Auger spectrum obtained from a platinum surface. Interpretation of an Auger spectrum requires comparison of the observed spectrum with reference spectra from samples of known composition. [30] Auger spectroscopy is discussed in more detail in chapter 5.
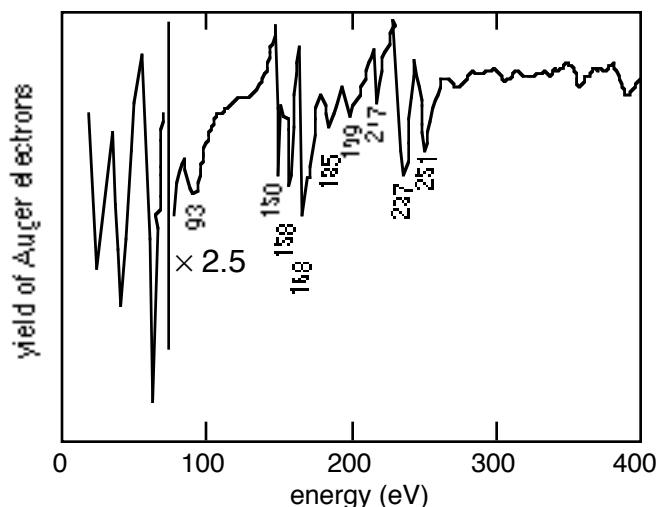
Figure 2.30 Auger spectrum of platinum. After [30].

Low energy electron diffraction (LEED) is used to determine the order of a surface. A monochromatic beam of electrons diffracts off the surface and is intercepted by a phosphor screen. The left side of Figure 2.31 shows the pattern formed by scattering of electrons from Pt(111). The hexagonal symmetry of the Pt(111) surface is reflected in the symmetry of the diffraction pattern. The right side of Figure 2.31 shows the diffraction pattern from a Pt(111) surface that has been exposed at 300 K to a few Langmuir of O_2: in addition to the diffraction spots due to the platinum atoms, there are spots attributed to diffraction of electrons from oxygen atoms. By comparing the positions of the spots due to oxygen to those due to platinum, it follows that the density of oxygen atoms is 1/4 the density of the platinum atoms. The oxygen atoms are arranged in a regular grid on top of the platinum surface; if their distributions were random they would not produce a sharp diffraction pattern. There are more examples of LEED in chapter 5.
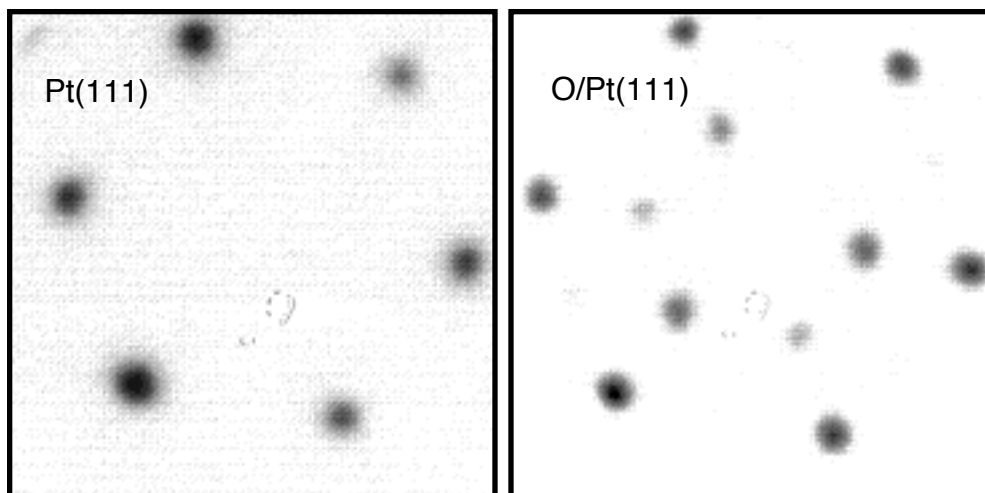
Figure 2.31 LEED patterns obtained from Pt(111), *left,* and O/Pt(111), *right.* The electron gun (not visible) obscures one of the spots due to oxygen.

The vibrational modes of an adsorbate can be probed by scattering a beam of monochromatic electrons off the sample. Some of the electrons lose energy by exciting discrete electronic or vibrational transitions in the adsorbates, so the distribution of adsorbate modes is reflected in the distribution of energies of the scattered electrons. The technique is called electron-energy-loss spectroscopy (EELS). Figure 2.32 shows the EEL spectrum of chemisorbed O_2 on Pt(111). [31-33] The signal at zero loss is 50 cm^{-1} wide; this is the resolution limit. The signals at 875 cm^{-1} and 700 cm^{-1} are attributed to stretching of the oxygen molecule along the O–O bond axis. [31] The signal at 380 cm^{-1} is assigned to vibration of the O_2 molecule perpendicular to the surface. [32] The signals at losses above 875 cm^{-1} are attributed to electrons that excited multiple quanta of the surface modes or coupled modes. The vibration of atomic oxygen with respect to the Pt(111) would scatter electrons with a loss of 480 cm^{-1}. [31, 32]
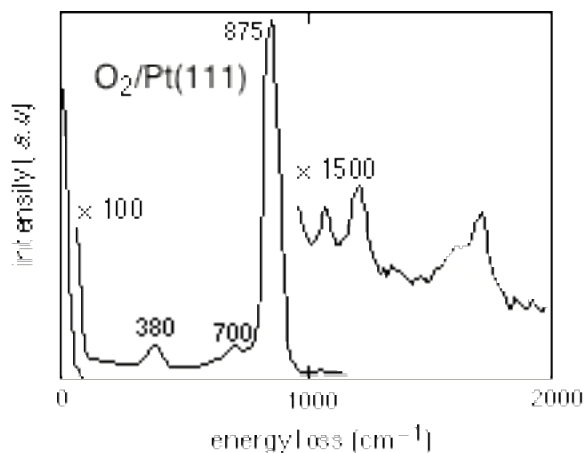
Figure 2.32 Electron-energy-loss spectroscopy of a saturated overlayer of O$_2$ on Pt(111) from a beam of 2 eV electrons incident at 75°. After [31]

Infrared (IR) spectroscopy is another way to study the vibrational modes of adsorbates. Infrared light reflected off the surface is absorbed at frequencies that are resonant with vibrational frequencies of the adsorbates. IR spectroscopy using short laser pulses has been employed to study the decay of vibration of adsorbates due to loss of vibrational energy to the substrate. The decay is complete in roughly one picosecond for adsorbates on metal surfaces. [34, 35] Very short laser pulses are used to resolve these timescales.

The spatial distribution of surface electronic states can be imaged with atomic resolution by scanning tunneling microscopy (STM). The STM micrograph can be interpreted as a map of the surface because the electronic surface states are determined by the substrate and the adsorbates. In a recent study of the thermal dissociation of O$_2$ on Pt(111), an STM was used to determine that when O$_2$ thermally dissociates, the oxygen atoms break free of their mutual bond with enough kinetic energy to move approximately two platinum lattice constants. [36] This is experimental evidence that atoms can have ballistic motion on a surface. Below we summarize how the STM was used to determine the sites where O$_2$ chemisorbs on Pt(111).

39

2.15 Thermal chemistry

We have seen that oxygen binds to platinum in several different forms: physisorbed molecular oxygen, chemisorbed molecular oxygen, and chemisorbed atomic oxygen. Because each form of oxygen is bound at a different site on the platinum with a different binding energy, these atoms become chemically active at different temperatures. A common way of studying adsorbate/substrate systems is to increase the sample temperature at a regular rate while monitoring the species desorbed from the surface. The experiment is called temperature-programmed desorption (TPD) or temperature programmed reaction spectroscopy (TPRS) depending on whether the adsorbates simply desorb from the surface, or react to form new species. The yield in TPD or TPRS is plotted against the corresponding temperature, indicating the temperatures of thermally induced desorption and reaction.

Figure 2.33 shows the TPD of chemisorbed molecular oxygen, O_2/Pt(111), obtained with a 4 K/s heating rate. The signal at 36 atomic mass units (amu), is due to oxygen molecules comprised of the 18 amu isotope of oxygen, $^{18}O_2$. The 140 K signal, called α–O_2, is attributed to direct desorption of intact molecules. The O_2 desorption at 750 K, β–O_2, shows that not all the oxygen desorbs at 140 K. If the TPD is stopped between the α–O_2 and the β–O_2 desorption signals, an EEL spectrum has features attributed to atomic oxygen, but none attributed to molecular oxygen. The LEED pattern is the pattern produced by atomic oxygen on Pt(111) (Figure 2.31, right side). These observations indicate that there is no molecular oxygen on the surface, but there is atomic oxygen. The β–O_2 signal must be due to recombination of oxygen atoms, known as recombinative desorption.
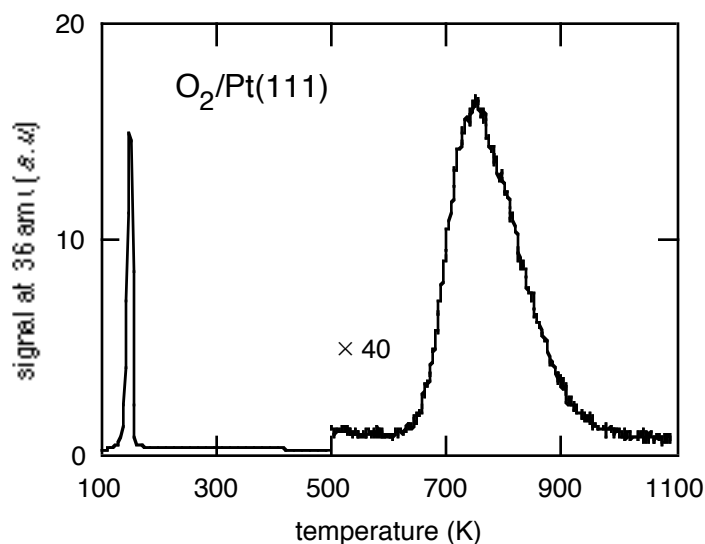
Figure 2.33 Temperature-programmed desorption of O_2/Pt(111). The sample was dosed with isotopic oxygen, $^{18}O_2$, and the signal is detected at 36 amu with a mass spectrometer.

So far we have discussed adsorption of a single species. The final section of this paper discusses photo-induced reaction between two adsorbed species, CO and O_2 on Pt(111). Production of CO_2 can be induced with light or heat. Figure 2.34 shows the signal at 48 amu detected during TPRS of CO/O_2/Pt(111). The surface was prepared with the isotopes $C^{18}O$ and $^{18}O_2$, and so the signal at 48 amu is due to $C^{18}O_2$. The different peaks correspond to the CO interacting with oxygen atoms in different states. The first desorption peak, α–CO_2 is not observed during TPRS of CO coadsorbed with atomic oxygen, CO/O/Pt(111). [37] The α-CO_2 is attributed to reaction of CO with an oxygen atom created by O_2 dissociation, before this atom equilibrates with the surface. [38] The other CO_2 peaks, β-CO_2, are due to reaction between CO and atomic oxygen after the atomic oxygen has equilibrated with the surface. The reaction occurs as the CO and O diffuse on the surface, forming islands; the multiple peaks arise from reaction as the CO and O collide during different stages of this diffusion. [39]

41
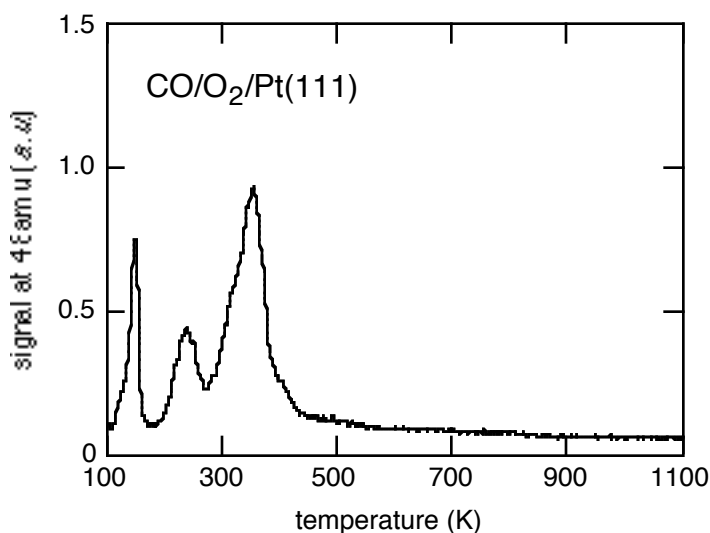
Figure 2.34 Temperature programmed reaction spectroscopy of CO/O$_2$/Pt(111). The signal at 48 amu is due to carbon dioxide, C^{18}O$_2$.

2.16 Isotope exchange

Isotopic labeling of reactants is used to determine pathways in surface reactions. Different isotopes of a molecule have different vibrational frequencies and therefore have different EEL spectra. With a mass spectrometer of resolution better than 1 amu, different isotopes of the same product are distinguishable in TPD and TPRS.

Figure 2.35 shows the application of isotopic labeling to the study of thermal reaction in O$_2$/Pt(111). A mixture of 50% ^{16}O$_2$ and 50% ^{18}O$_2$ was prepared by mixing ^{16}O$_2$ and ^{18}O$_2$ outside the vacuum chamber. This gas was admitted to the sample surface to produce a chemisorbed overlayer denoted (^{18}O$_2$, ^{16}O$_2$)/Pt(111). The left of Figure 2.35 shows the signal at 36 amu due to ^{18}O$_2$ product. The α-O$_2$ signal is about half as large as in Figure 2.33, and the β-O$_2$ signal is about one quarter as large as in Figure 2.33. The signal at 32 amu due to desorption of ^{16}O$_2$ looks very similar to the signal for ^{18}O$_2$. The right side of Figure 2.35 shows the signal at 34 amu due to ^{16}O^{18}O. There is no yield of α-^{16}O^{18}O, but comparison of the left and right sides of Figure 2.35 shows that the yield of β-^{16}O^{18}O is twice as large as the yield of β-^{18}O$_2$. These observations are consistent with the evidence

derived from EELS and LEED above. At 140 K, oxygen molecules desorb from the surface without opportunity to exchange isotopes of oxygen between molecules. Oxygen molecules also dissociate at 140 K. Near 700 K, the atoms recombine, but now there is opportunity for two different isotopes to form a molecule, $^{16}O^{18}O$. The probability of getting $^{18}O_2$ or $^{16}O_2$ at this stage is one half the probability of getting $^{16}O^{18}O$.
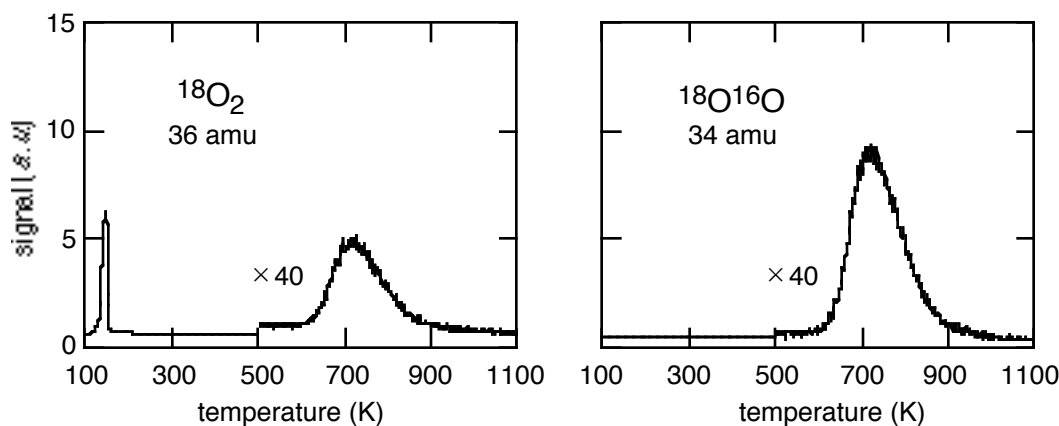
Figure 2.35 The TPD signal of (*left*) $^{18}O_2$ and (*right*) $^{16}O^{18}O$ from $(^{18}O_2, ^{16}O_2)/Pt(111)$. The yield of $^{16}O_2$ is very similar to the yield of $^{18}O_2$.

2.17 Details of the bonding of oxygen to platinum

In the gas phase, molecular oxygen has 12 valence electrons in the $2\sigma_g$, $2\sigma_u^*$, $1\pi_u$, $3\sigma_g$, and $1\pi_g^*$ orbitals [40] The right hand side of Figure 2.36 shows the electronic states of gas-phase O_2 which are most relevant to its bonding on platinum, including two π orbitals oriented normal to the molecular axis which have identical energies.

Experiments with scanning tunneling microscopes (STM) show that O_2 chemisorbs in at least three different configurations on Pt(111). [41] The O_2 is observed over a bridge site between two platinum atoms with the O–O bond axis parallel to the surface and aligned to face the tops of platinum atoms. Calculations show that the O–O bond length in this configuration is 0.139 nm and the energy of vibration of the O–O bond is 850 cm^{-1}. [42] An O_2 species bound over FCC three-fold hollows is also observed with the STM. [41] Calculations show that this O_2 molecule is tilted 8° out of the plane of the surface. The

O–O bond length is 0.143 nm and the energy of vibration is 690 cm^{-1}. [42] The calculated energies of vibration of the O–O bonds in the bridge and fcc configurations are consistent with observed vibrational energies from electron-energy-loss spectroscopy. The stretching of the O–O bond with respect to the 0.1207 nm length in the gas phase is consistent with the bond length inferred from x-ray spectroscopy. [43, 44] The stretching is due to transfer of electrons from the platinum into orbitals that are anti-bonding with respect to the O–O bond. The third O_2 species observed with STM is at O_2 adsorbed at step edges. [41, 45] Temperature-programmed desorption experiments show that the binding energy of all the O_2 species is close to 0.4 eV. [32]

When the O_2 chemisorbs, some of the oxygen orbitals mix with platinum orbitals. The $1\pi^*$ orbitals perpendicular to the surface mix with the platinum d-band orbitals, producing π_b^* and π_b orbitals. The $1\pi^*$ orbitals of the oxygen parallel to the surface are not greatly perturbed and are denoted π_n. [44, 46] A shaded bar in Figure 2.36 represents the extent of the entire π_b and π_n region compiled from experimental [43, 47] and computational [46, 48, 49] sources. Overall, there is a net transfer of charge from the platinum to the O_2. [32]
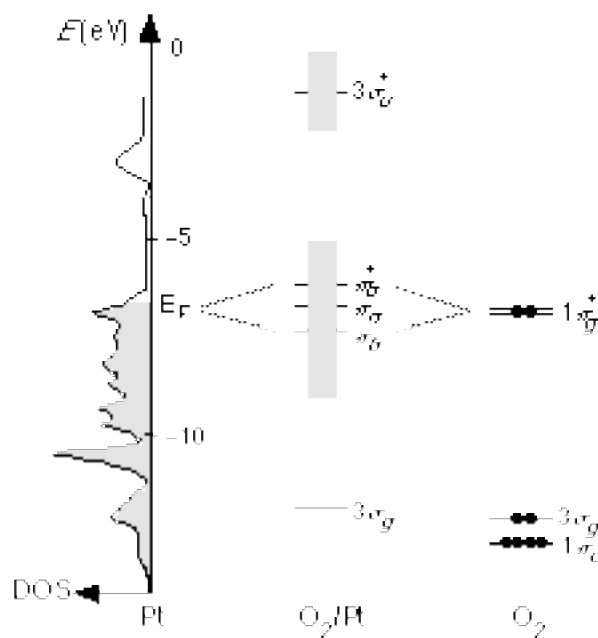
Figure 2.36 The calculated density of states of platinum [50] shown with the experimentally and theoretically determined states of O_2 chemisorbed on Pt(111). The vertical shaded bars indicate the approximate widths and locations of the orbitals of O_2 on the surface. Many of the O_2 orbitals are out of the energy range shown. [18]

A surface layer of atomic oxygen on Pt(111) can be obtained by exposing the surface to molecular oxygen at platinum temperatures above 145 K. [51] The surface coverage saturates at 0.25 ML with a p(2×2) LEED pattern. [32] The oxygen binds in fcc three-fold hollow sites, [52] with a 1.1 eV binding energy at 0.25 ML coverage, [32] and a 470-cm^{-1} Pt–O vibration. Higher coverages of atomic oxygen can be attained by photodissociation of N_2O/Pt(111), [53] or by electron-beam dissociation of O_2/Pt(111). [31]

III

Excitation pathways
in surface femtochemistry

3.1 Introduction

Irradiation of $CO/O_2/Pt(111)$ causes desorption of O_2 and oxidation of CO to form CO_2. [1-4, 6, 33, 54-58] The light excites electrons which induce the desorption or reaction. An important issue is whether the photo-excited electrons have a well-defined temperature. When the light source is a low-intensity arc lamp, there is no doubt that the photo-excited electrons interact with the adsorbates before the electrons thermalize; the energy of the thermalized electrons is far too low to stimulate the adsorbates. [59] There is an active debate, however, about the energy distribution of the electrons that excite the adsorbates when the light source is high-intensity, subpicosecond laser pulses.

According to one proposal, the adsorbates are stimulated by thermalized substrate electrons. [56] Collisions between the photo-excited electrons cause the electrons to reach a thermal distribution (Figure 2.24) before there has been opportunity for any appreciable adsorbate excitation. In this model, the desorption and reaction of the adsorbates depend on a well-defined substrate electron temperature (Figure 2.24). The electrons do not have the same temperature as the phonons.

Another proposal is that the photon-energy-dependent electron distribution plays a significant role in the surface reactions. [1] According to this model, the electrons interact with the adsorbates before the electrons have thermalized. The electron temperature is not well defined in these circumstances, because the distribution of electron energies is not a Fermi-Dirac function. This stage of the electron excitation is not captured by the simulation shows in Figure 2.24.

We measured the desorption of O_2 and production of CO_2 from $CO/O_2/Pt(111)$ irradiated with 0.3-ps laser pulses at 267, 400, and 800 nm. The states of the photo-excited electrons depend on the laser wavelength, and so by comparing the desorption and reaction yields at different wavelengths we can infer which electronic states are responsible for exciting the O_2 and CO. We found that the adsorbates are stimulated by electrons from states far above the Fermi level compared with thermal energy scales ($k_B T$), [1-5] and therefore our data support the model of substrate excitation by nonthermalized electrons.

The lifetime of the excitation responsible for O_2 desorption can be investigated by measuring the yield of O_2 from two subpicosecond laser pulses as a function of the time interval between the pulses. These two-pulse correlation experiments show that the excitation has a lifetime of about 1 ps. This time interval has been attributed to the time required for the hot electrons to cool to the phonon temperature (Figure 2.24). [1, 2, 58, 60, 61] We argue below that the two-pulse correlation experiments have been misinterpreted; the correlation time reflects the time required for relaxation of adsorbate vibrational modes, rather than the substrate electron-phonon coupling time.

Several groups have shown that the desorption induced by subpicosecond laser pulses scales nonlinearly with respect to the laser pulse fluence. [1, 2, 56, 57, 60, 62-65] We also observe this nonlinearity when the fluence is greater than 10 μJ/mm^2. The desorption from $CO/O_2/Pt(111)$, induced with continuous light [33, 54] or nanosecond pulses, [57] scales linearly with fluence. We have discovered that subpicosecond laser pulses also induce yields linear in fluence when the fluence of the laser pulses is below 10 μJ/mm^2.

3.2 Operation of the mass spectrometer in pulse counting mode

The yield in the laser experiments is measured with a mass spectrometer operated in pulse counting mode to maximize the signal-to-noise ratio. Figure 3.1 shows the configuration of instruments. The ion signal is amplified with a channeltron electron multiplier. A discriminator placed after the channeltron rejects the low-amplitude noise. The bias on the channeltron, and the thresholds on the discriminator and the counters are adjusted to maximize the signal due to ions while minimizing the noise.

We make the adjustments while viewing the signals on an oscilloscope. To ensure that connecting the oscilloscope to the circuit does not change the signal, the oscilloscope must not change the impedance of the circuit. The circuit in Figure 3.1 is easy to diagnose because it is terminated with 50-Ω resistors at several locations. The signal can be analyzed at these locations with a 50-Ω input impedance oscilloscope.

The discriminator is designed to accept input pulses with amplitudes in the range 0.1 – 10 mV. Higher input signals cause the electronics to momentarily "freeze" and lose subsequent signals. We adjust the bias on the channeltron so that the input to the discriminator does not exceed 10 mV. Figure 3.2 shows that this can be accomplished by choosing a channeltron bias near 1800 V. We plotted a histogram of actual channeltron output pulse height at 1800 V channeltron bias: in a 7000 sample histogram there were no pulses with amplitude greater than 10 mV. When the channeltron bias is 1900 V, 4.4% of the pulses are greater than 10 mV.
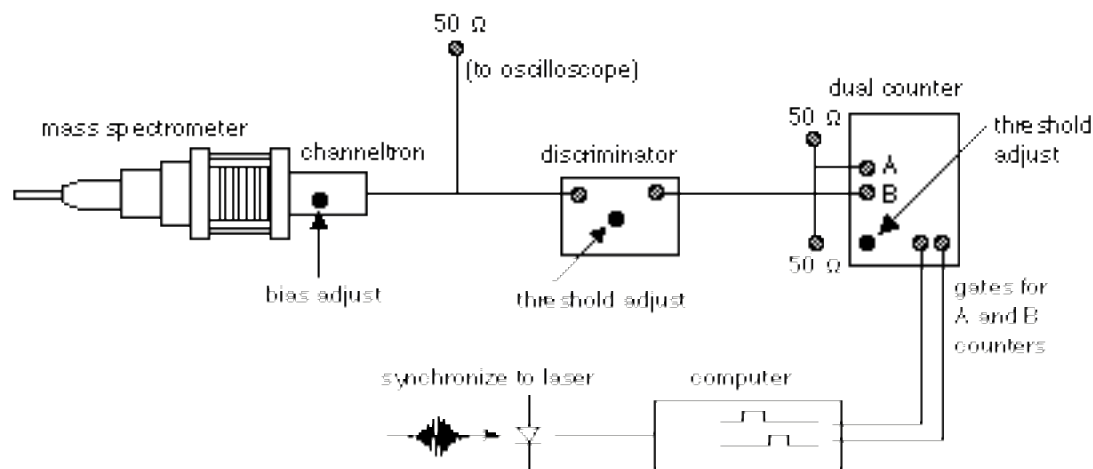
Figure 3.1 Schematic of the instruments used to measure the signal at the mass spectrometer in pulse counting mode. The ion signal from the mass spectrometer (UTI, 100C) is amplified by a channeltron (Galileo Electro-Optics, 4876) and sent to a discriminator (Modern Instrumentation Technologies), and then a dual counter (Ortec, 995). The gain of the channeltron is selected by adjusting the DC bias. Cables are split in several places and terminated in to 50-Ω resistors. An oscilloscope with 50-Ω input impedance can be connected in place of any of these resistors to monitor the signals without changing the total effective impedance on the cable.

The discriminator threshold is set to reject low-amplitude noise pulses from the channeltron. For every input pulse which exceeds the threshold, the discriminator sends a 10-ns duration TTL pulse to the pulse counter. The threshold is adjusted by turning a potentiometer on the discriminator circuit. Because the circuit does not provide a direct way to monitor the threshold level, we devised the following procedure to set the threshold in a reproducible manner. A particular channeltron bias is chosen, the mass spectrometer quadrupole filter is set to 50 amu, and the discriminator threshold is increased until the count rate drops to zero. This procedure uniquely identifies a setting of the potentiometer

with the chosen channeltron bias. Further adjustments of the threshold are specified with respect to this potentiometer setting.
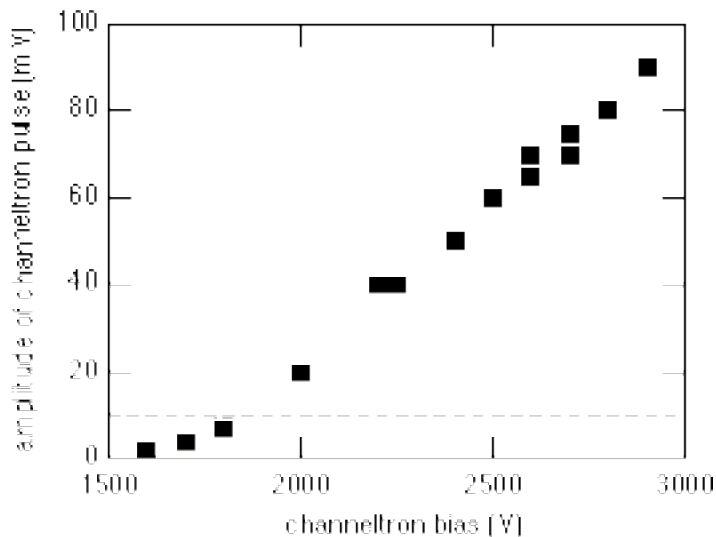
Figure 3.2 The amplitude of the typical pulses output from the channeltron increases with increasing DC bias applied to the channeltron. The dashed line indicates the maximum amplitude pulse which the discriminator is designed to accommodate.

Figure 3.3 shows the rate of discriminator output pulses as a function of discriminator threshold. At very low threshold the signal is enormous because the discriminator stops rejecting any noise pulses. A threshold of −9 on this scale was selected for the laser desorption experiments.

To confirm that the threshold and bias were chosen correctly, we measured the signal from background gases over a range of channeltron bias. Figure 3.4 shows that the count rate for CO_2 reaches a plateau near 1800 V channeltron bias.
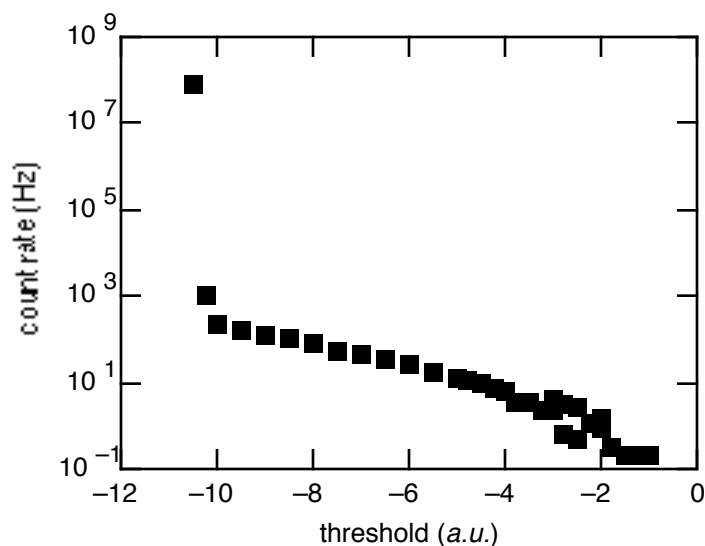
Figure 3.3 The output of the discriminator increases substantially for very low discriminator thresholds because the discriminator stops rejecting noise. The quadrupole filter of the mass spectrometer was tuned to 50 amu and the channeltron bias was 1800 V.
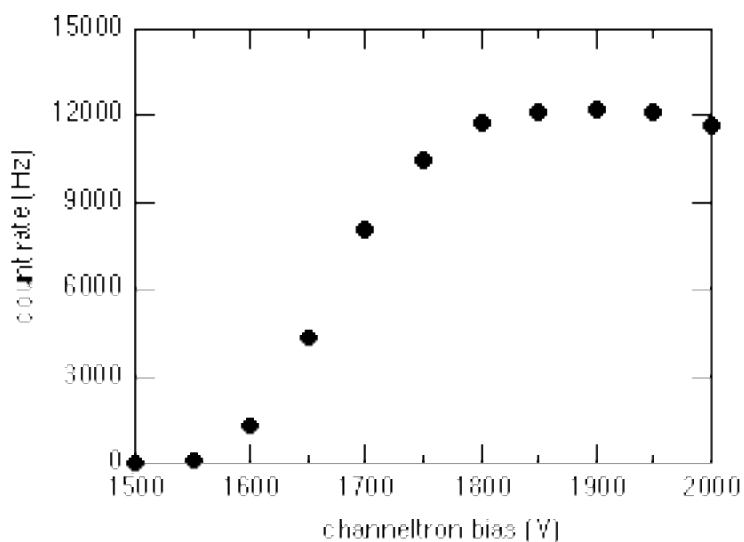
Figure 3.4 The rate of counting 44 amu ions from the CO_2 background as a function of channeltron bias at fixed discriminator threshold.

Another way to test the pulse counting electronics is to verify that it distinguishes between signal and noise. Figure 3.5 compares the count rate when the quadrupole filter on

the mass spectrometer is tuned to pass 44- or 50-amu ions. The counts when the filter is set to 50-amu are due to noise because there are very few 50-amu molecules in the chamber. The 44-amu signal is due to CO_2 in the chamber. As expected, the signal due to the CO_2 ions is substantially higher than the noise. The 10^2 ratio between them is not the signal-to-noise ratio for the laser desorption experiments. The true signal-to-noise ratio depends on the laser-induced yield and the other molecules in the chamber that have the same mass as the laser-desorbed species.
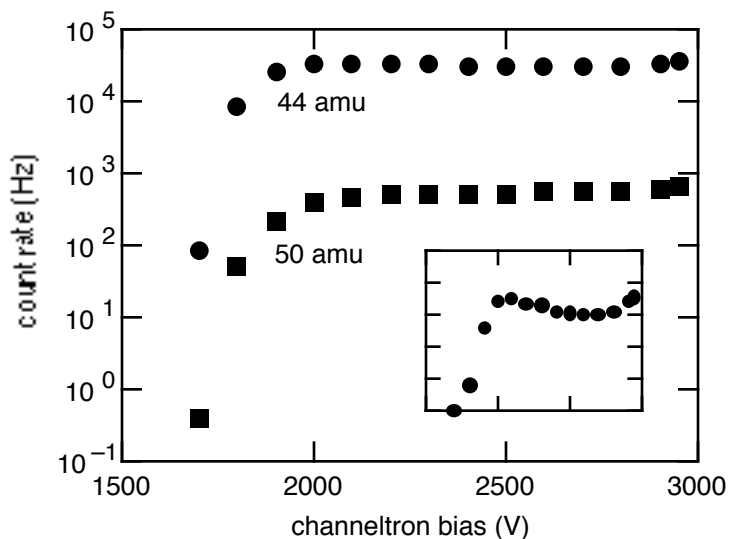
Figure 3.5 The count with the quadrupole filter set for 44- (●) and 50-amu (■) ions. The 44-amu signal due to ionized CO_2 from the chamber background is about 10^2 times larger than the noise. The inset shows the 44-amu signal on a linear scale, demonstrating the onset of discriminator saturation and channeltron ion feedback.

The inset in Figure 3.5 shows the count rate at 44 amu on a linear scale to show clearly that the rate rises to a maximum, decreases, and then rises again as the channeltron bias is increased. The decrease in the count rate is attributed to saturation of the discriminator when the channeltron bias becomes high enough that the channeltron output exceeds the maximum input of the discriminator (Figure 3.2). The increase in the count rate at high bias is attributed to ion feedback in the channeltron, caused by ionization of residual gas in the

channeltron by electrons arriving at the collector of the channeltron. The ions are accelerated back towards the input of the channeltron where they stimulate emission of electrons that then propagate back through the channeltron, producing a false count. The laser desorption experiments are conducted at a channeltron bias for which there is no ion feedback and for which the channeltron output is matched to the discriminator.

3.3 Time dependence of the ion signal

The desorption yield is measured correctly only if the rate at which molecules are ionized is below the rate at which the pulse counting electronics operates. In this section we explain how the maximum pulse counting rate was determined and show that the rate is fast enough to accurately measure the laser-induced desorption yield.

The simplest test of the counting rate is to admit a gas to the chamber at continuously increasing pressure and note when the detected signal stops increasing. Figure 3.6 shows that the count rate becomes nonlinear near 10 MHz and saturates near 14 MHz. This experiment took several minutes to complete. We therefore interpret 14 MHz as the maximum counting rate under conditions of constant signal throughput. We tested the count rate of the Ortec 995 counter under similar constant throughput conditions by connecting the counter to a square pulse train from a function generator. We confirmed that the counter operates at over 50 MHz, and therefore the counter is not responsible for the saturation observed in Figure 3.6.
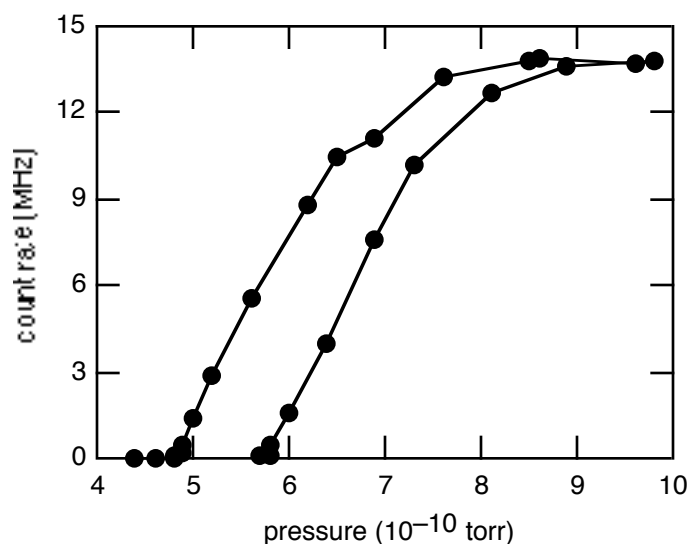
Figure 3.6 The count rate of 36 amu ions from $^{18}O_2$ admitted to the chamber. The hysteresis occurs because the gas phase $^{18}O_2$ does not reach equilibrium with the pumping during the time required to make these measurements.

Laser desorption sends a large flux of molecules to the mass spectrometer in a short time interval. To determine when the ions are detected as a function of delay following the laser pulse, we gated the counter with a 3 μs pulse beginning at an adjustable time with respect to the laser pulse. Figure 3.7 shows that the detected yield has a two component distribution. The fast component of 10^{-4} s duration (inset, Figure 3.7) is attributed to a burst of molecules arriving at the ionizer directly from the sample. The rapid decay of this signal is due to the escape of the molecules through a mesh surrounding the ionizer of the mass spectrometer. The long time-scale decay is attributed to the pumping of this yield from the chamber. If differential pumping of the mass spectrometer were available, it would greatly reduce this component of the distribution. Even with differential pumping, the distribution would not be the true time of flight distribution of the laser-desorbed molecules because the ionizer of the mass spectrometer ionizes molecules over an extended region and therefore does not capture a sample of the desorbed molecules with a single surface-to-ionizer flight time.
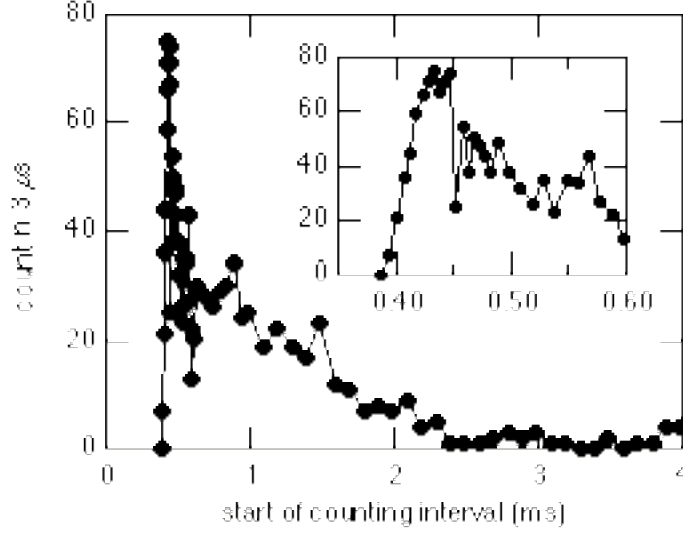
Figure 3.7 The counts attributed to laser desorption of O_2 from $O_2/Pt(111)$ as a function of delay with respect to the laser pulse. The total yield in the rapid decay component (inset) and the slow decay component is 1.3×10^4 counts. This is not a true time of flight distribution (see text).

The highest count rate observed in the inset of Figure 3.7 is 75 counts in 3 μs, or 25 MHz. Comparison of Figure 3.7 with Figure 3.6 shows that the pulse counting electronics operate more quickly during short-bursts than during continuous counting.

During the laser desorption experiments we ensure that the total yield from a single laser shot is no more than 3×10^3 counts, far below the 1.3×10^4 counts in Figure 3.7. Measurements similar to those of Figure 3.7 confirm that in a typical laser desorption experiment, the maximum signal is approximately 15 counts in 3 μs. From Figure 3.7 we know that the count rate can be at least 75 counts in 3 μs. We therefore conclude that the pulse counting electronics do not saturate during the laser desorption experiments.

3.4 Femtosecond laser system

The laser system consists of a Ti:Sapphire oscillator and a chirped-pulse-regenerative amplifier producing 800-nm, 0.5-mJ pulses at a 1-kHz repetition rate. Frequency-doubled 400-nm pulses are produced in a 1-mm long lithium barium borate (LBO) crystal yielding

0.2-mJ pulses. Sum-frequency mixing of the 800- and 400-nm pulses in a 0.3-mm long beta-barium-borate (BBO) crystal, yields 20-μJ pulses at 267 nm. The laser system is described in detail in another thesis. [66] Recent improvements to the laser system are described here.

Figure 3.8 shows the intensity autocorrelation of the laser pulses. The sharp edges on the main peak indicate that the pulses do not have a pedestal — there is very little low-intensity light on the leading or trailing edge of the peak of the pulse. The secondary peak about 4 ps from the main peak is attributed to a back-reflection in the autocorrelator. This assignment is based on the separation of the secondary peak from the main peak, the dependence of the secondary peak height on the direction of the laser polarization in the autocorrelator, and the insensitivity of the secondary peak to any adjustment of the oscillator or the amplifier.

The inset of Figure 3.8 shows the main peak from an autocorrelation corresponding to pulses of 130-fs duration. The laser system can be adjusted to produce pulses with durations as low as 70-fs. [1, 66] Pulses up to 10 picosecond duration are obtained by changing the path length in the pulse compressor; this adjustment stretches the pulse in time by imposing a frequency chirp but preserves the spectral bandwidth.
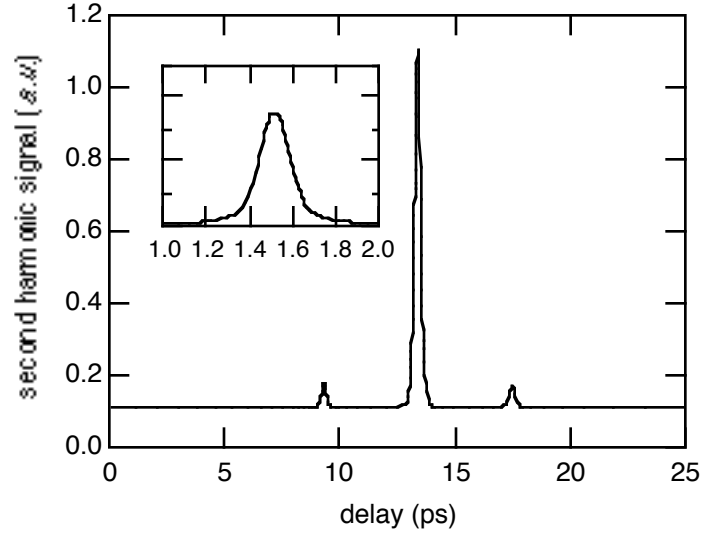
Figure 3.8 Intensity autocorrelation of the amplified 800-nm, *s*-polarized

pulses. The secondary peak about 4 ps from the main peak is an artifact of

the autocorrelator.

The autocorrelation in Figure 3.8 was obtained from pulses produced by a regenerative

amplifier containing a Pockel cell comprised of two anti-reflection coated electro-optic

crystals separated by an air gap. The Pockel cell in the earlier version of the amplifier was

comprised of two electro-optic crystals immersed in index-matching fluid. Figure 3.9 shows

that this older amplifier generated pulses with an extra pulse 5.6 ps from the main pulse.

The duration of the 400-nm pulses was determined by sum-frequency mixing the 400-

nm pulses with 800-nm pulses in 0.3-mm thick BBO to produce 267-nm pulses. A 400-nm

pulse duration of 0.3-ps was deduced from the 267-nm cross-correlation signal and the

measured 800-nm pulse duration. Similarly, the 267-nm pulse duration was determined by

difference-frequency mixing the 267-nm pulses with 400-nm pulses in 0.2-mm thick BBO

to produce 400-nm pulses. The duration of the 267-nm pulses was 0.26-ps.
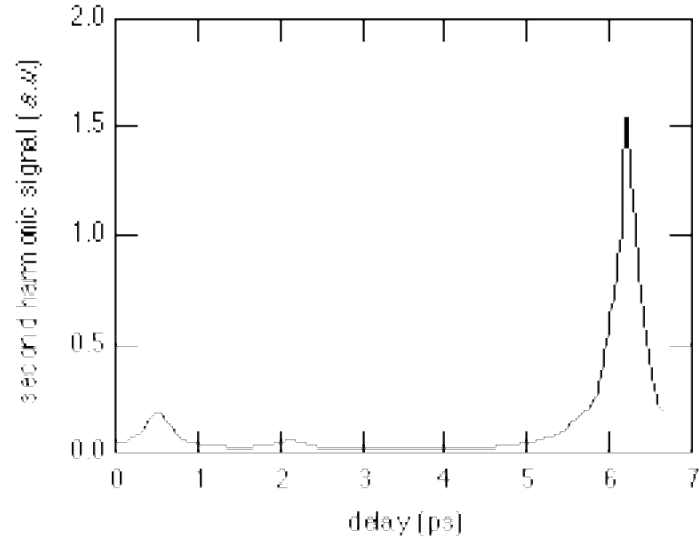
Figure 3.9 Intensity autocorrelation obtained from a *p*-polarized pulse-train produced by an older version of the amplifier. The peak about 5.6 ps from the main peak is attributed to a pulse created by reflections of the main pulse in the Pockel Cell. The secondary peak about 4 ps from the main peak is an artifact of the autocorrelator.

In the original design of the laser, the 500-μJ, 100-fs pulses were focused in air through the 1.5-mm aperture of a mechanical shutter. The data in Figure 3.10 show that after the focus, the spectrum of the pulses was distorted. We discovered that the spectrum is not distorted if the pulses are focused in argon gas, but it is distorted if the pulses are focused in nitrogen gas. These observations suggest that nonlinear interactions of the laser pulses with the nitrogen distort the spectrum. We solved the problem by modifying the layout of the laser amplifier so that the pulses are focused through the shutter before they are compressed. Figure 3.11 shows that the uncompressed, 0.1-ns pulses are not distorted.
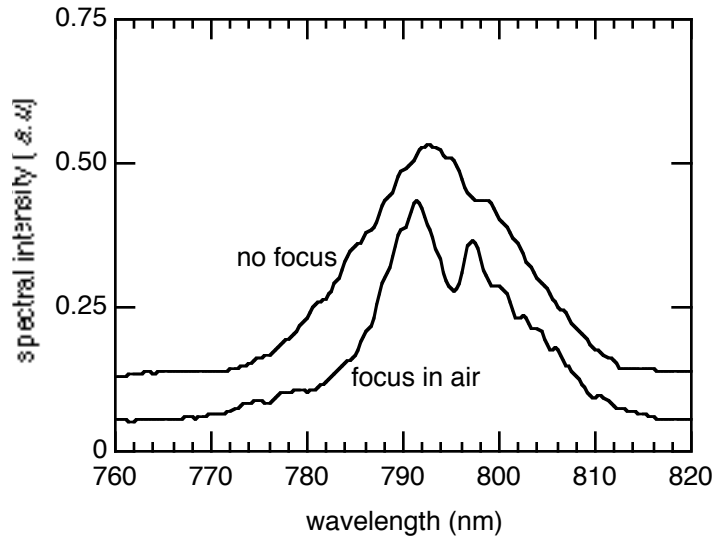
Figure 3.10 The spectrum of the laser pulses that pass through a focus in air is attenuated at 795 nm. Laser pulses that pass through air without focusing are not perturbed.
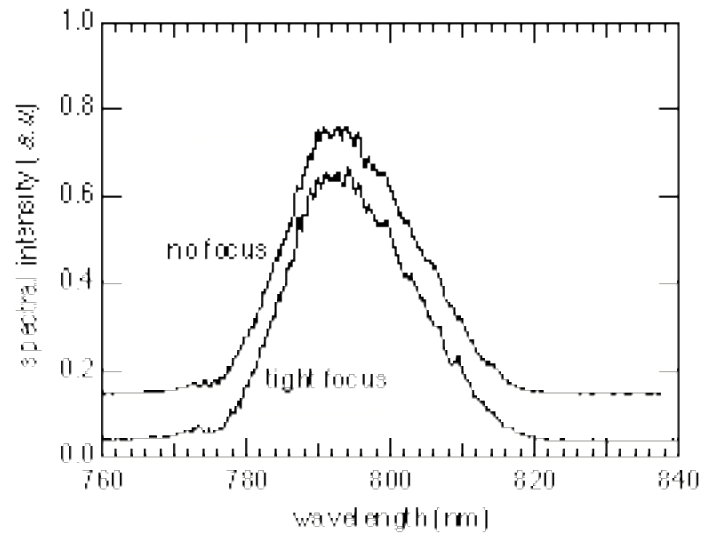
Figure 3.11 The uncompressed 0.3-ns duration pulses have the same spectrum with or without focusing. The uncompressed amplified beam can be focused through the shutter.

3.5 Low-intensity photochemistry

Light from an arc lamp can induce desorption of O_2 from $O_2/Pt(111)$. Figure 3.12 shows the dependence of the O_2 desorption yield on photon wavelength. [33] The yield increases with decreasing wavelength and there is no photodesorption at wavelengths longer than 550 nm. Figure 3.13 shows that the desorption rate is linear in fluence: $Y \propto F^1$. Irradiation also induces rearrangement of the O_2 molecules on the surface; temperature-programmed desorption following irradiation of $O_2/Pt(111)$ exhibits a broadened α-O_2 desorption peak compared with non-irradiated $O_2/Pt(111)$. [54, 67]
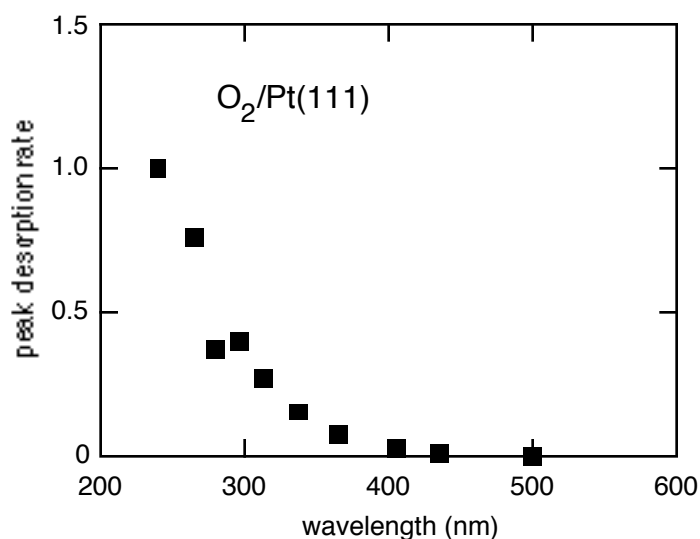
Figure 3.12 The rate of desorption of O_2 from $O_2/Pt(111)$ under irradiation with continuous light from an arc lamp. After [33]

A model called DIET, for desorption induced by electron transitions, explains the wavelength dependence of the data and the linear dependence of yield on fluence. It also very successfully accounts for electron-beam induced reactions. Figure 3.14 shows how electronic excitation of an adsorbate can cause it to acquire the translational energy required for desorption. In the electronic ground state the interaction of the adsorbate with the surface is described by the potential energy surface labeled PES_1. The reaction coordinate could be, for example, the distance between the adsorbate and the surface, or the alignment of the adsorbate with respect to the surface. The interaction of the adsorbate with the

substrate following electronic excitation of the adsorbate is represented by the potential energy surface labeled PES$_2$. In general, PES$_2$ does not have a minimum at the same reaction coordinate as PES$_1$. PES$_2$ could be purely repulsive, with no minimum at all.
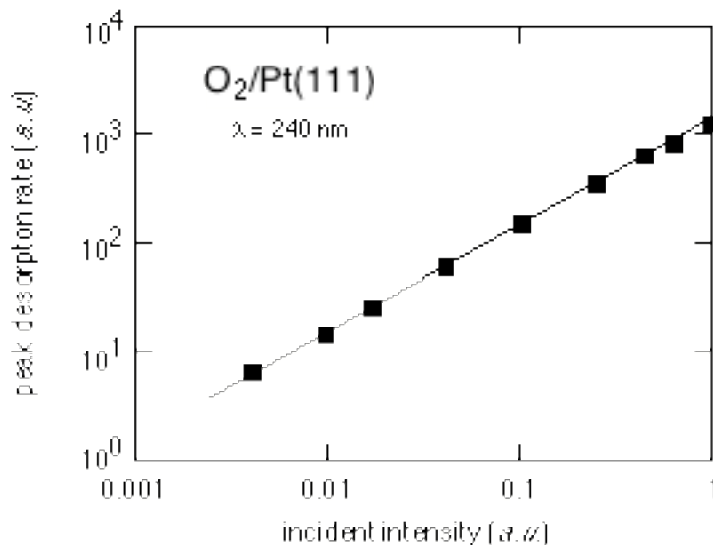
Figure 3.13 The rate of desorption of O_2 from O_2/Pt(111) induced with 240 nm irradiation, as a function of the incident intensity. The line has slope 1. After [33]

Electronic excitation of the adsorbate is represented by the vertical arrow from the minimum of PES$_1$. This transition is an example of a Frank-Condon transition. The transition could be caused by a photon exciting an electron within the O_2/Pt(111) complex; such an excitation does not change the overall charge on the adsorbate. The transition could also be the transfer of an electron from the substrate to the adsorbate, changing the charge on the adsorbate. When there is charge-attachment, the PES$_2$ would contain the influence of the interaction between the charged adsorbate and the image charge.
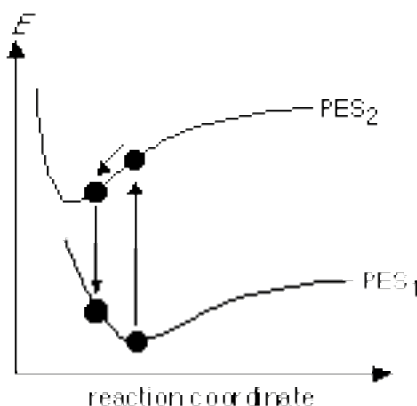
Figure 3.14 Desorption induced by electron transition (DIET) is explained in terms of two potential energy surfaces for the adsorbate-surface interaction.

An adsorbate excited to PES_2 accelerates toward the new potential energy minimum. When the electronic excitation relaxes, the adsorbate returns to PES_1, having acquired translational and potential energy. This energy accounts for desorption of the adsorbate.

Each photo-excitation of an electron and the possible subsequent excitation of an adsorbate acts independently of the other photo-induced excitations. This feature of the model accounts for the linear dependence of yield on fluence. The dependence of yield on wavelength reflects the need for photo-excited electrons to have energies appropriate to access available affinity levels of the adsorbates.

During irradiation of O_2/Pt(111) with an arc lamp, the fluence is kept low enough that the increase in surface temperature is only a few Kelvin: the surface temperature remains well below the 120 K temperature at which O_2 desorbs. According to the Fermi-Dirac function, Figure 2.10, the thermalized electron energies are near 20 meV. In contrast, the photon energy at, say, 400 nm, is about 3.2 eV. It is these nonthermal electrons, with energies that reflect the photon energy, that cause the transition depicted in Figure 3.14. After thermalization of the electrons, the energy of an individual photon is distributed among all the electrons, and ultimately, all the surface modes. After thermalization, there is no longer sufficient energy in any individual electron to induce desorption.

The situation could be different when a subpicosecond laser pulse excites the material. According to Figure 2.23, the subpicosecond laser pulses create a transient electron temperature far in excess of the temperature required for desorption of O_2 under equilibrium conditions. Could this hot, thermal distribution of electrons induce desorption? Our experiments are designed to address this question.

3.6 Surface femtochemistry experiments

We studied the photochemistry of $CO/O_2/Pt(111)$ using laser pulses from a 1-kHz regeneratively-amplified Ti:sapphire laser. The 100-fs, 800-nm pulses are frequency-doubled in a 1-mm thick lithium barium borate crystal and frequency-tripled in a 0.3-mm thick beta-barium borate crystal. The 267- and 400-nm pulses have 0.26- and 0.3-ps duration, respectively. The 800-nm pulses are chirped to 0.3 ps so the pulse durations at all wavelengths are similar.

The energy of each laser pulse is measured with a photodiode that is calibrated with a power meter. The response of the power meter varies less than 3% over the range 267–800 nm. To ensure that there is no nonlinear absorption in the platinum, we measured the fraction of the laser pulse energy absorbed into platinum. The measured absorption of the platinum is constant over the range of fluences used in the experiments, and is in agreement with the reflectivity calculated from the published dielectric function of platinum. [17] We also verified that the absorption of the chamber window does not depend on fluence. These results confirm that the laser energy absorbed in the platinum is a constant fraction of the pulse energy measured outside the vacuum chamber.

The spatial profile of the laser pulses is measured with an ultraviolet-sensitive CCD camera. The profile captured by the camera is fit well by a Gaussian function. The fluence incident on the camera is reduced to a level where the camera response is linear by reflecting the beam off the front surfaces of two pieces of glass and is further attenuated with neutral-density filters. To confirm the accuracy of the camera-based spatial profile measurement, we measured the spatial profile of a Helium-Neon laser with the camera and compared it with

the profile determined by scanning a pinhole through the beam while measuring the transmitted light with a photodiode. The camera and pinhole methods yield laser profiles that are identical to within 1%.

The absorbed laser fluence is determined from the energy absorbed in the platinum, and the spatial profile of the laser pulse, accounting for the 45° angle of incidence. The fluence varies over the profile of the laser spot; values quoted below refer to the absorbed fluence at the peak of the spatial profile. The tests described above confirm that there is no wavelength-dependent, nor any fluence-dependent systematic error in the calculation of absorbed fluence.

The experiments are conducted on a 12-mm diameter Pt(111) crystal in an ultrahigh vacuum chamber with a base pressure of 5×10^{-11} torr. The sample cleaning and analysis are described in Chapter 5. After cleaning, molecular oxygen and carbon monoxide are adsorbed to saturation on the platinum surface. [32, 33] Molecular oxygen is deposited on the platinum surface as soon as the temperature has fallen below 94 K after a cleaning cycle. Carbon monoxide is deposited after the oxygen. To reduce background pressure, all adsorbates are deposited using a tube of 12-mm diameter brought to within 3 mm of the platinum surface.

The laser-induced O_2 desorption yield and CO_2 reaction yield are measured with a quadrupole mass spectrometer operating in pulse-counting mode. We alternate between detecting O_2 and CO_2 on successive laser shots. Between shots, we translate the sample to an unirradiated part of the sample preparation. A potential difference of –90 V is applied between the sample and the ionizer of the mass spectrometer to prevent stray electrons from interacting with the sample. A tube of 4-mm inner diameter extends from the ionizer to the sample. This tube collects molecules desorbed from the surface within 14° of the surface normal. The ionizer is enclosed in mesh to allow the laser-induced desorption and reaction products to escape. Using a high-speed mechanical shutter, we reduce the laser

repetition rate to allow the gas-phase products to be pumped out of the chamber between successive laser shots.

The yield depends on the area of the sample preparation exposed to the laser pulses. To obtain an appreciable yield at low fluence, a large laser spatial profile of full-width-half-maximum up to 1 mm^2 is used. At high fluence, the spatial profile is decreased to as low as 0.05 mm^2 to reduce the absolute yield and avoid saturating the pulse-counting electronics. The yields reported below are divided by the laser spot size to allow comparison between runs taken with different laser spot sizes. Below 20 μJ/mm^2, less than 1% of the adsorbates is depleted by a single laser pulse; to increase the signal in this regime, we admit up to 10 pulses at a 1-kHz rate to one spot on the sample and the mass spectrometer measures the total yield.

3.7 Results

Figure 3.15 shows the yield of oxygen molecules obtained from CO/O$_2$/Pt(111) with 267-, 400-, and 800-nm laser pulses. Near 10 μJ/mm^2 there is a clear change in the dependence of the yield on absorbed laser fluence. Above 50 μJ/mm^2, the yield saturates because the pulse desorbs an appreciable fraction of the adsorbed oxygen. [1]
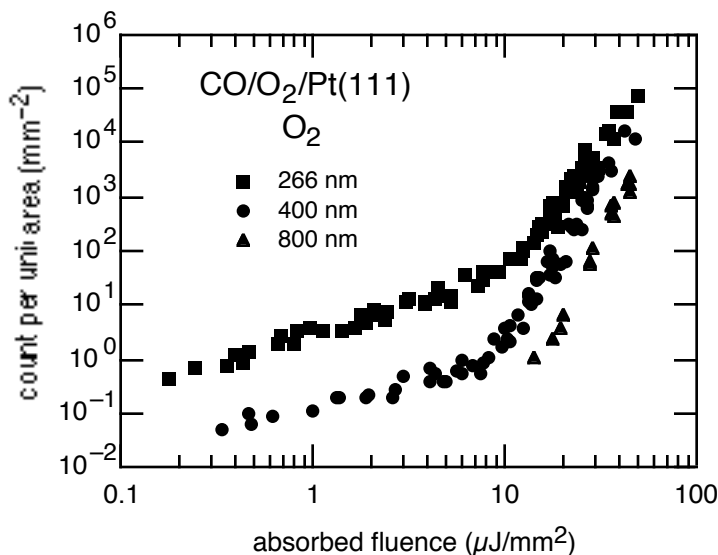
Figure 3.15 Yields of O$_2$ from CO/O$_2$/Pt(111) obtained with laser pulses of 0.3-ps duration at ▲ 800-, ● 400-, and ■ 267-nm wavelengths.

Below 10 μJ/mm^2 the yield from 267- and 400-nm pulses depends linearly on fluence. To determine the linear cross section in this regime, we measured the decreasing yield from a single spot on the sample as the surface coverage is depleted by 3000 laser pulses. The linear cross sections thus obtained are σ_{267} = (4 ± 2) × 10^{-19} cm^2 and σ_{400} = (4 ± 2) × 10^{-20} cm^2 for 267- and 400-nm pulses, respectively. We do not observe any linear dependence of yield on fluence for 800-nm laser pulses; continuous light sources with wavelengths longer than 600 nm also do not induce reaction [33].

Between 10 and 50 μJ/mm^2 the yield depends nonlinearly on fluence. The data can be described by a simple power law, $Y \sim F^p$, where $p > 1$ and F is the fluence absorbed in the platinum. As Table 3.1 shows, the exponent p decreases with decreasing wavelength.

The wavelength dependence of the yields is also apparent in a comparison of the absolute yields at a particular fluence. Table 3.2 summarizes the wavelength dependence of the yields at 1 and 30 μJ/mm^2. At both fluences, the yield increases substantially as the wavelength decreases.

Figure 3.16 shows the yield of carbon dioxide from the same sample preparation as Figure 3.15. The dependence of the CO_2 yield on fluence is similar to that of O_2. Table 3.3 summarizes the ratio of yield of O_2 to yield of CO_2. When using 267- or 400-nm pulses at fluences below 10 μJ/mm^2 (*i.e.*, in the linear regime), the yields of O_2 and CO_2 are the same. Above 20 μJ/mm^2, the yield of O_2 is substantially more than the yield of CO_2, and the ratio is smaller at shorter wavelengths. The ratios shown in Table 3.3 are not corrected for the small dependence of the mass spectrometer detection efficiency on species.
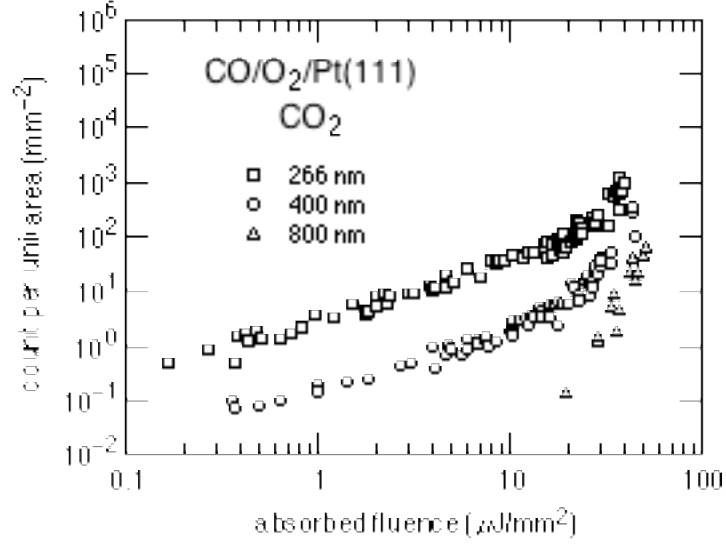
Figure 3.16 Yields of CO_2 from $CO/O_2/Pt(111)$ obtained with laser pulses of approximately 0.3-ps duration at $\triangle$ 800-, $\bigcirc$ 400-, and $\square$ 267-nm wavelengths.

Table 3.1 Wavelength dependence of the power law exponent. The yield is linear in fluence below 10 $\mu J/mm^2$, but very nonlinear in fluence above 10 $\mu J/mm^2$. There is no low-fluence yield with 800-nm laser pulses.

P	267 nm	400 nm	800 nm
$\leq 10\ \mu J/mm^2$	1.1 ± 0.1	0.9 ± 0.1	n.a.
$\geq 10\ \mu J/mm^2$	4.8 ± 0.5	6.0 ± 0.5	7.2 ± 0.5

Table 3.2 Wavelength dependence of the laser-induced yield. At all fluences studied, the yield increases with decreasing wavelength.

yield	267 nm	400 nm	800 nm
$1\ \mu J/mm^2$	3 ± 0.5	0.1 ± 0.02	0
$30\ \mu J/mm^2$	8000 ± 1500	2000 ± 500	120 ± 25

67

Table 3.3 Wavelength dependence of the ratio of O_2 to CO_2 yield. The ratio is one at fluences below $10\ \mu J/mm^2$, but O_2 desorption is favored over production of CO_2 at fluences above $20\ \mu J/mm^2$. At fluences above 20 $\mu J/mm^2$, the ratio is strongly wavelength dependent.

$O_2{:}CO_2$	267 nm	400 nm	800 nm
$\leq 10\ \mu J/mm^2$	1 ± 0.1	1 ± 0.1	n.a.
$\geq 20\ \mu J/mm^2$	25 ± 5	55 ± 15	70 ± 10

To explore the time dependence of the desorption, we measured the total desorption yield from two 80-fs laser pulses as a function of the delay $t_1 - t_2$ between them. The pulses are orthogonally polarized to avoid interference. The resulting two-pulse correlation is shown in Figure 3.17. The dashed line shows the total yield when the two pulses act independently, *i.e.*, when $t_1 - t_2 \to \pm\infty$. The dependence of the signal on $t_1 - t_2$ reflects the evolution of the substrate and adsorbate excitations responsible for desorption. The data show a 1.8 ps wide peak centered at $t_1 - t_2 = 0$ on top of broad wings. The broad wings are approximately 0.1 ns wide.
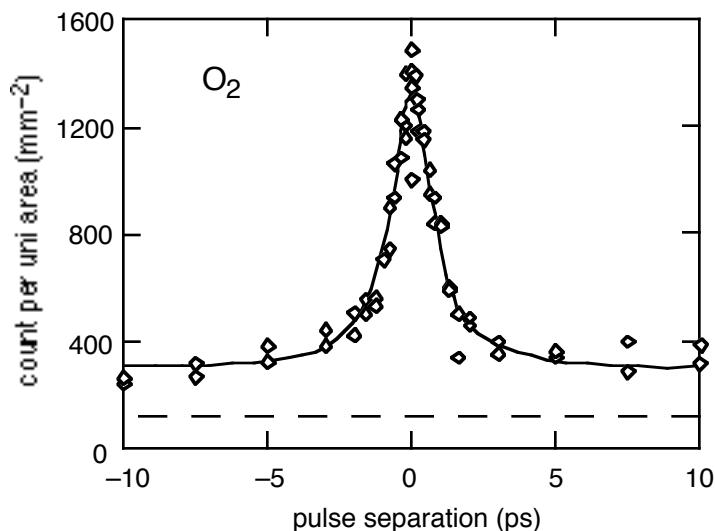
Figure 3.17 Desorption yield versus time delay $t_1 - t_2$ between two 80-fs excitation pulses at 800-nm for pulses of equal absorbed fluences. The dashed line denotes $Y(t_1 - t_2 = \pm \infty)$. The width of the central peak is 1.8 ps. The desorption yield is still enhanced after 75 ps. [1]

3.8 Interpretation of the results

The desorption and reaction yields at fluences below 10 $\mu J/mm^2$, shown in Figures 3.15 and 3.16, scale linearly in fluence. The cross sections are about 10^{-23} m^2 and increase with decreasing wavelength. The yield of O_2 and CO_2 obtained from $CO/O_2/Pt(111)$ with continuous light [33] or nanosecond-pulses [57] also scales linearly in fluence. The cross sections measured with these low-intensity sources are about 10^{-23} m^2 and increase with decreasing wavelength. These similarities suggest that the linear surface femtochemistry is due to the same mechanism responsible for the surface photochemistry induced with continuous-wave or nanosecond-pulsed light sources.

The excitation of $CO/O_2/Pt(111)$ with these low-intensity sources has been attributed to electronic transitions into normally-vacant orbitals of the O_2. [33] This new electronic configuration causes the adsorbate atoms to move, accumulating vibrational or translational energy that may lead to desorption or reaction. Two mechanisms for the electronic

transition have been proposed. The photon can stimulate a direct transition between orbitals in the $O_2/Pt(111)$ complex. [33] Alternatively, the photon may excite an electron to a state above the Fermi level in the Pt(111) band structure, from which it crosses into an orbital of the $O_2/Pt(111)$ complex. [68] Either way, the electron interacts with the O_2 while retaining a substantial portion of the initial photon energy. The surface photochemistry in the linear regime is therefore governed by electrons with a nonthermal distribution. The wavelength dependence of the cross section is due to the required matching of the energy of the photo-excited electron with the energies of the vacant O_2 orbitals.

Irradiation of a metal surface creates an electron distribution with thermal and nonthermal components. For intense subpicosecond laser pulses, the thermal distribution of electrons can reach several thousand Kelvin for a few picoseconds. [62] Several authors attributed the nonlinear dependence of yield on fluence, high desorption yields, and short excitation lifetimes to these transient hot electrons. [65, 69-71] The electron temperature depends on the pulse duration and the fluence absorbed in the platinum, but not on photon wavelength. [19]

Our experiments show three ways in which the nonlinear surface femtochemistry depends on wavelength. The power-law exponents summarized in Table 3.1 depend on wavelength, increasing from 4.8 ± 0.5 at 267 nm to 7.2 ± 0.5 at 800 nm. The desorption yields summarized in Table 3.2 are also wavelength dependent: at 30 $\mu J/mm^2$, the yield from 267-nm pulses is about 4 times that from 400-nm pulses, and about 65 times that from 800-nm pulses. The ratio between O_2 and CO_2 yields, summarized in Table 3.3, depends on wavelength, varying from 70 at 800 nm to 25 at 267 nm. The nonlinear femtochemistry of $CO/O_2/Pt(111)$ depends on wavelength, and so the thermalized electron distribution cannot be solely responsible for exciting the adsorbates. We attribute the wavelength dependence of the nonlinear surface femtochemistry on $CO/O_2/Pt(111)$ to interaction of the adsorbates with electrons from a nonthermal distribution.

The data from the two-pulse correlation experiments, Figure 3.17, show that the sample retains excitation from the first laser pulse for longer than 10 ps. This correlation time is longer than the electron-electron, electron-adsorbate, [63, 71] electron-lattice, [20, 62] and lattice-adsorbate [34, 35] relaxation times. The only remaining equilibration process is the cooling of the surface to the bulk, which occurs on roughly the same time scale as the decay of the wings. The correlation beyond 10 ps indicates that desorption is accomplished more easily from a pre-heated surface than from a cold surface.

We consider now the prominent 1-ps wide peak in Figure 3.17. [1, 58] Experiments show that in subpicosecond laser excitation of gold film, the nonthermal electron distribution persists for 0.5 ps. [21, 72] Though there are no published measurements of the electron-electron thermalization time for platinum, the thermalization time in platinum is likely less than the 1-ps correlation in Figure 57. It is therefore unlikely that the 1-ps correlation reflects the time for electrons to thermalize.

The 1-ps correlation in Figure 3.17 has been attributed to cooling of the thermalized electron distribution, [58, 60, 73] because, as Figure 2.24 shows, the electrons equilibrate with the lattice on a 1-ps time scale. Though the thermalized electron distribution may contribute to the laser-induced desorption and contribute to the 1-ps correlation, the wavelength dependence of our data indicates that thermalized electrons do not solely govern the desorption. The 1-ps correlation more likely reflects the time required for the adsorbates to dissipate the vibrational excitation induced by the first laser pulse. Indeed, the time scale for relaxation of vibrational excitation at a metal surface is approximately 1 ps. [34, 35]

3.9 Conclusions

We describe the subpicosecond-laser-induced desorption of O_2 and reaction to make CO_2 in $CO/O_2/Pt(111)$ as follows. When the laser-pulse fluence is below 10 $\mu J/mm^2$, the reaction is due to the same mechanism as surface photochemistry induced with continuous-wave and nanosecond pulses (section 3.5). Above 10 $\mu J/mm^2$, another excitation

mechanism dominates the reaction; yields are nonlinear in fluence and depend on wavelength. The thermalized electron distribution depicted in Figure 2.24 does not cause the desorption and reaction. Models need to account for the nonthermal electrons to predict the wavelength dependence of our data. This result implies that previously published two-pulse correlation data must be re-interpreted. The short, 1-ps correlation is due to relaxation of vibrational excitation of the adsorbates between laser pulses, and not due to cooling of the electrons to the bulk phonon temperature.

The transition between linear and nonlinear dependence of yield on fluence is of theoretical interest. The linear dependence of yield on fluence is due to electrons stimulating adsorbates independently of the other excited electrons. Above the transition fluence, the nonlinearity indicates that cooperative action of the photo-excited electrons dominates the linear process. These cooperative effects have been described as a frictional coupling between the substrate electrons and the adsorbates, [70] and as a repeated excitation of the adsorbate within the time required for cooling of the adsorbate vibration [71].

High fluence, subpicosecond laser pulses could be used to desorb a sample of the adsorbates on a surface to probe the surface coverage with subpicosecond time resolution. One could imagine recording the changing adsorbate composition during a surface reaction. In principle, the efficient desorption could also be used to reduce surface coverage and increase reaction rate in a catalytic process in which site blocking inhibits the reaction.

If subpicosecond laser pulses could not induce reaction with an efficiency at least comparable to the desorption efficiency, then it would be difficult to study the dynamics of a surface reaction with subpicosecond-time resolution. Our results suggest that it will be possible to study the dynamics of surface photochemistry by limiting the subpicosecond-laser pulses to low fluence, and thereby not desorbing all the reactants.

IV

Reaction pathways
in surface femtochemistry

4.1 Introduction

In section 2.16 we used isotopic labeling to interpret the temperature-programmed desorption data in Figure 4.1. Intact O_2 molecules desorb at 140 K in a process called molecular desorption. Some O_2 dissociates rather than desorbing. The O_2 yield at 750-K is called recombinative desorption because these O_2 molecules are formed when two atoms recombine on the surface. In this chapter we study the subpicosecond-laser-induced desorption of O_2 from $CO/O_2/Pt(111)$ to determine whether the pathway is molecular or recombinative.

In the laser-induced desorption experiments, it is difficult to intuitively predict the pathway because conditions are far from thermal equilibrium. According to the simulation in section 2.10, a subpicosecond laser pulse heats the electrons in a metal to well over 10^3 K, while the phonons are only heated to about 10^2 K. When the electron temperature is so much higher than the temperatures for both molecular and recombinative desorption, which pathway will prevail? We use isotopic labeling to distinguish between these pathways.
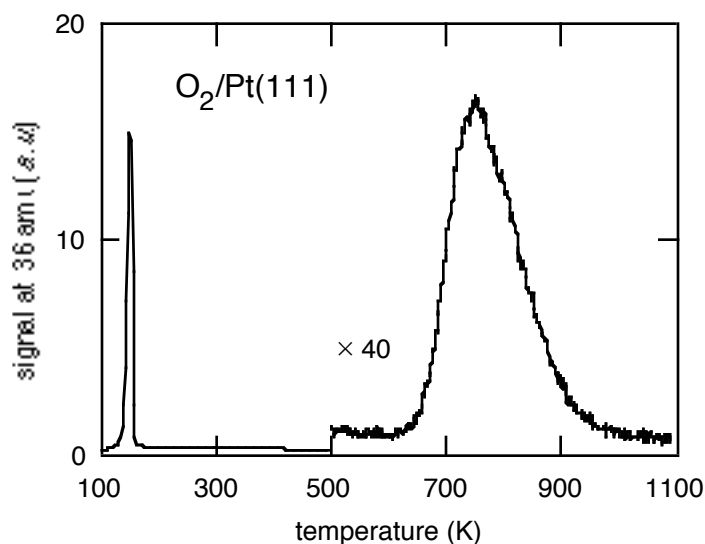
Figure 4.1 The molecular ($\approx$ 140 K) and recombinative ($\approx$ 750 K) thermal desorption of O_2 from O_2/Pt(111). These are analogous to the molecular and atomic reaction pathways studied under subpicosecond laser irradiation.

We also studied the pathway by which CO becomes CO_2 in CO/O_2/Pt(111). One might expect the O_2 to dissociate before reacting with the CO because the O–O bond is already stretched by electrons from the platinum (section 2.17). In fact, oxygen dissociation is so important that it is common to call the molecularly adsorbed O_2 species a precursor — that is, a precursor to atomic oxygen. Another possibility is that intact O_2 interacts with CO. We used isotopic labeling to investigate whether an intact oxygen molecule interacts with CO, or whether the oxygen dissociates first.

In this chapter we examine the reaction pathway for O_2 desorption and CO_2 production from CO/O_2/Pt(111) induced with high-intensity subpicosecond pulses. The experiments exploit isotopic labeling of the oxygen atoms to distinguish between atomic,

$$O_2(ad) \rightarrow 2O^* \rightarrow O_2(g) \tag{4.1}$$

$$CO(ad) + O_2(ad) \rightarrow CO(ad) + 2O^* \rightarrow CO_2(g) + O(ad)$$

and molecular

$$O_2(ad) \rightarrow O_2(g) \tag{4.2}$$

$$O_2(ad) + CO(ad) \rightarrow [CO_3]^{\ddagger} \rightarrow O(ad) + CO_2(g)$$

74
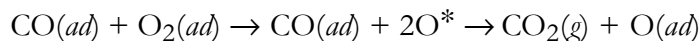
pathways. The data show that the O_2 desorbs as an intact molecule, and the data place constraints on the nature of the transition states in production of CO_2.

4.2 Evidence for reactive oxygen atoms on Pt(111)

If the atoms released by dissociation of O_2 have a high translational energy then the atoms should interact with coadsorbates. An experiment showed that irradiation of X/O_2/Pt(111), (X = Kr, Xe, Ar), causes desorption of the noble gas. [74] The desorption cross section is comparable to the O_2 dissociation cross section. In contrast, irradiation of X/Pt(111) does not cause desorption of the noble gas. The noble gases desorb from X/O_2/Pt(111) with an angular-distribution peaked 35° from the surface normal, suggesting that they receive a lateral impulse while desorbing. These observations suggest that the noble gas desorption is caused by an oxygen atom released by O_2 dissociation. The translational energy of the oxygen atom accounts for the desorption of the noble gas at a 35° angle. [74]

The scanning tunneling microscope (STM) provides additional evidence that dissociation of O_2 molecules produces energetic oxygen atoms. The STM can measure the separation between oxygen atoms following thermal dissociation of O_2 from O_2/Pt(111). [36] Table 4.1 shows that most of the resulting oxygen atoms pairs are found two lattice constants apart, and some of the atom pairs are separated by 3 lattice constants. The authors interpret this as evidence that thermal dissociation of O_2 creates energetic oxygen atoms which translate along the surface before they equilibrate with the surface. These energetic atoms are sometimes called *nascent* atoms. [33]

75

Table 4.1 The separation of the oxygen atoms from thermal dissociation of $O_2/Pt(111)$. Distances are in units of the platinum lattice constant. Data from Ertl *et al.* [36].

separation (latt. const.)	1	$\sqrt{3}$	2	$\sqrt{7}$	3
probability (%)	7.3	21.8	56.4	12.7	1.8

Before the STM was available, Matsushima studied the pathway to thermal oxidation of CO in $CO/O_2/Pt(111)$. [38] Figure 4.2 shows results of temperature programmed reaction of $CO/O_2/Pt(111)$. Matsushima argued that the yield of CO_2 at 140 K is due to reaction of CO with an atom released by thermal dissociation of O_2, Equation 4.1. The yield of CO_2 at 140 K in Figure 4.2 does coincide with the dissociation of O_2 from $O_2/Pt(111)$ in Figure 4.1. Also, there is no production of CO_2 at 140 K when CO is coadsorbed with atomic oxygen, $CO/O/Pt(111)$, [37] and isotopic labeling confirms that the CO reacts with oxygen atoms originating on O_2 molecules, and not with oxygen atoms pre-adsorbed to the surface. [38] Though Matsushima's results are consistent with CO oxidation by the pathway in Equation 4.1, he did not provide evidence to rule out interaction of CO with an intact, nonequilibrated O_2 molecule.

Irradiation of $N_2O/O/Pt(111)$ with 193-nm laser pulses produces O_2 and N_2. [75] Isotopic labeling showed that the O_2 is formed from a preadsorbed oxygen atom and an oxygen atom from the N_2O. The N_2 desorbs with a bimodal distribution of kinetic energies. The authors correlated the production of O_2 with the observation of the energetic N_2 product, and argued that when the N_2O dissociates to produce an energetic N_2, the oxygen atom must also be energetic to conserve momentum. It is this energetic oxygen atom that interacts with the preadsorbed oxygen atom to produce O_2. If the O_2 were formed from a direct reaction between N_2O and O, there would be no correlation between the production of the energetic N_2 species and the yield of O_2.
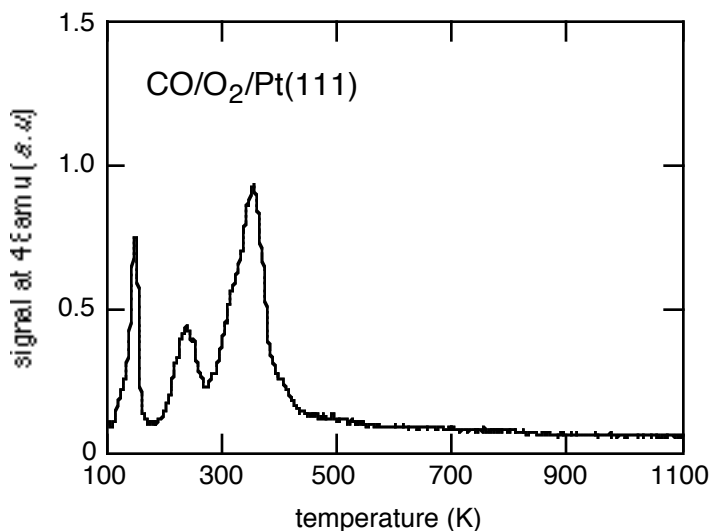
Figure 4.2 Temperature programmed reaction spectroscopy of $CO/O_2/Pt(111)$ showing production of CO_2 beginning at 140 K.

4.3 Experimental evidence for reaction of oxygen in molecules

Irradiation of $CO/N_2O/Pt(111)$ at 47 K with an arc lamp (200-1000 nm) induces reaction to make CO_2. [76] When the adsorbate coverage is high, CO_2 desorbs during irradiation. If irradiation is interrupted while the coverage of N_2O is still high, then TPRS of the sample reveals CO_2 desorption at 85 K, but not at higher temperatures. This signal at 85 K is attributed to desorption of CO_2 that formed during irradiation of the sample. If irradiation is interrupted after the N_2O coverage is reduced to 55% of the initial coverage, TPRS reveals a CO_2 signal at 270 K. This signal is attributed to β-CO_2 produced by a thermal reaction between CO and atomic oxygen fragments from photodissociated N_2O.

What do these results suggest about the chemical pathway to CO_2 formation? If dissociation of N_2O is the first step in the formation of CO_2, it is unlikely that all the oxygen atoms produced are captured by carbon monoxide. The oxygen atoms that escape reaction should equilibrate with the surface and appear as β-CO_2 in post-irradiation temperature programmed reaction scans. However, the β-CO_2 is only observed following very long exposures. The authors therefore conclude that until the surface coverage is

substantially reduced, CO oxidation occurs in a reaction process where the N–O bond breaking and O–C bond formation take place simultaneously. Such a process is called a concerted reaction.

4.4 Reaction pathway in the photochemistry of CO/O$_2$/Pt(111)

The photo-induced oxidation of CO in CO/O$_2$/Pt(111) has been attributed both to interaction of CO with oxygen atoms released by O$_2$ dissociation [33], and interaction of CO with excited oxygen molecules. [77] Under cw irradiation, the cross sections for desorption of O$_2$ and reaction to produce CO$_2$ have identical dependence on wavelength. [33] This similarity suggests that the same electronic excitation of the O$_2$ is responsible for both desorption and reaction, but it does not indicate whether O$_2$ interacts with CO before or after dissociation. Yates *et al.* carefully measured the cross sections for O$_2$ desorption and dissociation and concluded that the amount of dissociation of O$_2$ is consistent with dissociation of O$_2$ prior to reaction with CO. [67] Prior to the work of Yates *et al.*, Ukraintsev and Harrison published estimates of the cross sections which indicated that there is not sufficient dissociation to account for the observed CO$_2$ yield, but they did not describe the procedures used to measure the cross sections. The cross sections measured by Yates *et al.* are probably more reliable, but they do not prove that CO oxidizes by an atomic mechanism — they are merely consistent with an atomic mechanism.

The reaction mechanism under subpicosecond laser excitation is very different from that with longer pulses. [57] For example, CO$_2$ production is readily observed at 800 nm, [1] well beyond the 550-nm threshold [33] for CO$_2$ production with light of nanosecond or longer duration. The reaction pathway which leads to O$_2$ desorption or CO$_2$ production under high-intensity subpicosecond pulse irradiation could be different than the pathway under cw irradiation.

4.5 Surface femtochemistry experiment with isotopic labeling

The experiments are conducted on a 12-mm diameter Pt(111) crystal in an ultrahigh-vacuum chamber with a base pressure of 5×10^{-11} torr. The sample cleaning and analysis of its composition are described in chapter 5. After cleaning, a saturation coverage of molecular oxygen, atomic oxygen, or carbon monoxide is adsorbed on the platinum surface. Molecular oxygen is deposited directly after a cleaning cycle, as soon as the platinum temperature has fallen to 94 K. At this temperature there is no thermal dissociation of the oxygen. To coadsorb CO and O_2, carbon monoxide is deposited after the oxygen. A coverage of atomic oxygen is obtained by exposing the platinum surface to molecular oxygen at a surface temperature of 250 K. [32] The surface is then further cooled before depositing any coadsorbates. Isotopic mixtures of $^{16}O_2$ and $^{18}O_2$ are prepared by mixing the isotopes outside the chamber and then depositing the isotopic mixture as in a regular O_2/Pt(111) preparation. To reduce background pressure while still obtaining saturation coverage, all adsorbates are deposited using a tube of 12-mm diameter that is brought to within 3 mm of the platinum surface. We verified the coverages using temperature programmed reaction spectroscopy and LEED. All laser experiments are performed at a base temperature of 84 K.

We studied the photochemistry of CO/O_2/Pt(111) using the frequency-tripled pulses of a regeneratively amplified Ti:sapphire laser at 267 nm. The frequency-tripled output of the laser consists of a 1-kHz train of 0.26-ps pulses of up to 25 μJ per pulse. The pulse duration was determined by difference-frequency mixing the pulse with the 800-nm fundamental in a thin BBO crystal. [78] The energy of each laser pulse is measured with a calibrated photodiode. This energy reading is converted into absorbed fluence taking into account spatial profile (determined using a CCD camera), angle of incidence, platinum reflectivity, and absorption and reflection losses of the vacuum chamber window. The fluence varies over the profile of the laser spot; values quoted below refer to the local absorbed fluence at the peak of the spatial profile.

For each laser pulse, the reaction yield at one mass-to-charge ratio is measured with a quadrupole mass spectrometer. The mass spectrometer has a tube of inner diameter 4 mm that extends from the ionizer to the sample. Nearly the entire solid angle at the opening of the tube is filled by the Pt(111) crystal. A negative bias of 90 V between the sample and the chamber prevents electrons escaping the ionizer from disturbing the surface preparation. Using a high-speed mechanical shutter, we reduce the laser repetition rate to 2 Hz to allow the gas-phase products to be pumped out of the chamber. The background levels, measured 50 ms before each laser pulse, do not change over the course of an experiment. The detection limit for each mass-to-charge ratio depends on the background present in the chamber at that mass and on the signal due to cracking of higher mass species in the mass spectrometer ionizer. Counts attributable to the background in the vacuum chamber are subtracted from the data.

4.6 Results of the surface femtochemistry experiments

Figure 4.3 shows the yields of O_2 and CO_2 from $CO/O_2/Pt(111)$. Each data point represents the yield from a single laser pulse at a fresh (not previously irradiated) location on the platinum. The data are normalized to the laser spot size to allow comparison between data runs taken with different spot sizes. Note the nonlinear relationship between yield and fluence characteristic of photochemistry initiated with subpicosecond laser pulses at fluences above 10 μJ/mm^2. [2, 56] This chapter focuses on data obtained in this nonlinear regime. We measured reaction yields for several combinations of reactants and isotopes to determine the reaction pathway in the nonlinear regime.
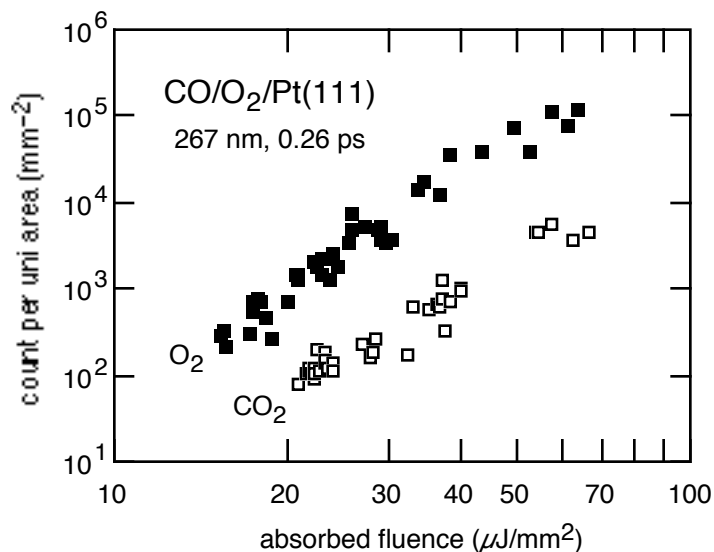
Figure 4.3 Laser-induced (267 nm, 0.26 ps) yields of O_2 and CO_2 from $CO/O_2/Pt(111)$. Each data point represents the yield from a fresh spot on the surface preparation.

Table 4.2 summarizes the yields from various surface preparations. The shading indicates which species are deposited on the surface before irradiation. As Figure 4.3 shows, the ratio of the CO_2 and O_2 yields is constant between 30 and 80 $\mu J/mm^2$; for all sample preparations, the product ratios vary little over this fluence range. The values in the Table correspond to the laser-induced yields at a fluence of 30 $\mu J/mm^2$ and are normalized to the yield of $C^{18}O_2$ from $C^{18}O/^{18}O_2/Pt(111)$. Where a maximum yield is given, the yield is below our detection limit for that species and sample preparation.

We first verified that there is no CO_2 production from a surface prepared with just CO. As the data in column 1 of Table 4.2 show, there is no measurable CO_2 yield within the detection limit. We do, however, observe a small CO yield.

Table 4.2 Relative yields from 267-nm, 0.26-ps laser pulses at 30 μJ/mm^2. There is a column in the table devoted to each sample preparation. The products detected are listed on the left-most column. The numbers in each row indicate the relative yields, normalized to the yield of CO_2 from $CO/O_2/Pt(111)$.

	1	2	3	4	5	6	7
	C^{18}O	C^{18}O/^{18}O	C^{18}O/^{18}O$_2$	C^{16}O/^{18}O$_2$	^{16}O$_2$/^{18}O$_2$	^{16}O$_2$/^{18}O	^{18}O
^{18}O		<0.2^a					<0.2^a
^{16}O$_2$					80 ± 5	15 ± 5	
^{18}O^{16}O					0.5 ± 0.2	0.05 ± 0.02	
^{18}O$_2$		0 ± 0.001^b	25 ± 5	25 ± 5	40 ± 10		0 ± 0.001^b
C^{16}O							
C^{18}O	0.03 ± 0.01	0.5 ± 0.2	<0.2^c				
C^{16}O^{18}O				1 ± 0.2			
C^{18}O$_2$	0 ± 0.001^b	0.01 ± 0.005	1 ± 0.2	0.01^d			

^{a}signal attributed to water background

^{b}detection limit

^{c}signal attributed to cracking of CO_2

^{d}signal attributed to isotopic impurity in surface preparation

Column 2 shows that, in contrast to experiments with low intensity irradiation, [55] some CO_2 is produced from reaction of carbon monoxide coadsorbed with oxygen atoms. We also observe CO desorption for this surface preparation. The oxygen, however, does not desorb as either atomic or molecular oxygen.

Columns 3 and 4 summarize yields from a surface preparation of carbon monoxide coadsorbed with oxygen molecules. We used C^{18}O and C^{16}O isotopes to see if the original oxygen atom in the CO gets replaced in the formation of CO_2. The yield of C^{18}O$_2$ reported in column 4 can be attributed to isotopic impurities in the surface preparation and thus we

find no evidence for oxygen replacement in the subpicosecond-laser-induced CO_2 formation.

The data in column 3 allow us to establish that the CO yield reported in columns 1 and 2 is not due to cracking of CO_2 in the mass spectrometer. In the experiments of column 3, the signal at 30 amu is 0.2 (20% of the CO_2 signal). This gives an upper limit of 20% for the probability of cracking of the laser-produced CO_2 in the ionizer. Thus in column 1, the maximum amount of signal at 30 amu that can be attributed to cracking of CO_2 is 20% of 0.01, which is well below the observed signal.

The experiments summarized in column 5 address whether there is exchange of oxygen atoms between $^{18}O_2$ and $^{16}O_2$ during laser-induced desorption from $(^{18}O_2,^{16}O_2)/Pt(111)$. The observed yield of $^{16}O^{18}O$ is 240 times smaller than the yield of $^{18}O_2$ or $^{16}O_2$. We find therefore no evidence for exchange of oxygen atoms between oxygen molecules under subpicosecond laser irradiation.

In column 6 we investigate exchange of oxygen atoms between molecular $^{16}O_2$ and coadsorbed atomic ^{18}O. Again we obtain a yield of $^{16}O^{18}O$ that is much smaller than the yield of $^{16}O_2$. This result contrasts sharply with the observation of a reaction between oxygen atoms from the photodissociation of N_2O and coadsorbed oxygen atoms. [75]

Column 7 shows that there is no laser-induced recombination of atomic oxygen on the surface. As in the case of coadsorbed CO and O (column 2), there is no detectable desorption of atomic oxygen.

The small $C^{18}O_2$ and $^{16}O^{18}O$ yields in columns 4–6 of Table 4.2 are due either to laser-induced processes or to isotopic impurities in the surface preparation. We therefore compared the laser-induced yields with thermal yields obtained by temperature programmed reaction spectroscopy (TPRS). Figure 4.1 shows a TPRS scan for saturation coverage of O_2 on platinum. As the temperature is raised, some of the oxygen molecules desorb and some dissociate into atoms. The large, narrow peak at 140 K (α-peak) in Figure 4.1 is due to desorption of intact oxygen molecules; the broad peak around 750 K (β-peak) is due to

atoms that recombine and then desorb as O_2 molecules. [32] To determine the thermal yield of oxygen, we measured the areas under the α-peaks of the various isotopes of O_2 for $(^{18}O_2, ^{16}O_2)/Pt(111)$ and $^{16}O_2/^{18}O/Pt(111)$ surface preparations. Thermal CO_2 yields were obtained by integrating the areas under corresponding CO_2 TPRS scans for a $C^{16}O/^{18}O_2/Pt(111)$ sample preparation. The thermal yields are reported in Table 4.3, labeled and normalized within each column for easy comparison to Table 4.2. The $C^{18}O_2$ and $^{16}O^{18}O$ yields in Table 4.2 are comparable to those in Table 4.3. It is therefore likely that the small $C^{18}O_2$ and $^{16}O^{18}O$ yields reported in Tables 4.2 and 4.3 are due to isotopic impurities.

To determine if high-intensity subpicosecond laser pulses cause photodissociation of oxygen, we irradiated the entire surface of a saturated [32] 0.44 ML $^{18}O_2/Pt(111)$ preparation and then determined the remaining surface coverage with a post-irradiation [79] temperature programmed reaction scan. Figure 4.4 shows the temperature programmed reaction scan for $^{18}O_2$ following irradiation of the $^{18}O_2/Pt(111)$ surface with 55 $\mu J/mm^2$, 800-nm pulses. We used 800-nm pulses because there is no linear photo-dissociation of O_2 at that wavelength. [33, 54] Any photo-dissociation at 800 nm must therefore be due to the mechanism responsible for nonlinear chemistry. However, we observe no desorption of α-O_2 or β-O_2 (Figure 4.4). This indicates that no detectable amount of oxygen molecules or oxygen atoms is left on the surface after irradiation.

Table 4.3 Summary of relative temperature-programmed desorption yields. There is a column devoted to each sample preparation. The products detected are listed in the left-most column. The numbers in the table indicate the relative yields of the molecules and their isotopic variations. In column 4, the yields are normalized to the $C^{16}O^{18}O$ yield; in columns 5 and 6, the yields are normalized so that the $^{16}O_2$ yields match the corresponding values in Table 4.2.

	$C^{16}O/^{18}O_2$	$^{16}O_2/^{18}O_2$	$^{16}O_2/^{18}O$
	4	5	6
^{18}O			
$^{16}O_2$		80	15
$^{18}O^{16}O$		0.3	0.07
$^{18}O_2$		45	
$C^{16}O$			
$C^{18}O$			
$C^{16}O^{18}O$	1		
$C^{18}O_2$	0.01		

Does this mean that the laser pulses do not dissociate the oxygen molecules? It is possible that the laser dissociates a small fraction of the O_2 molecules, and that the O atoms are scavenged by background gas molecules that adsorb to the surface. For example, if $C^{16}O$ adsorbs during the experiment, it could react with atomic ^{18}O created by the laser and prevent this oxygen atom from appearing as β-O_2 during the temperature programmed reaction scan. Figure 4.4 shows a small amount of $C^{16}O^{18}O$. This very low CO_2 signal could be due to a thermally induced reaction on the sample mount. If, however, we attribute all of this signal to reaction on the platinum surface between laser-dissociated oxygen and background contamination, we obtain an upper limit for laser-induced dissociation of 1.8% of the initial O_2 coverage.
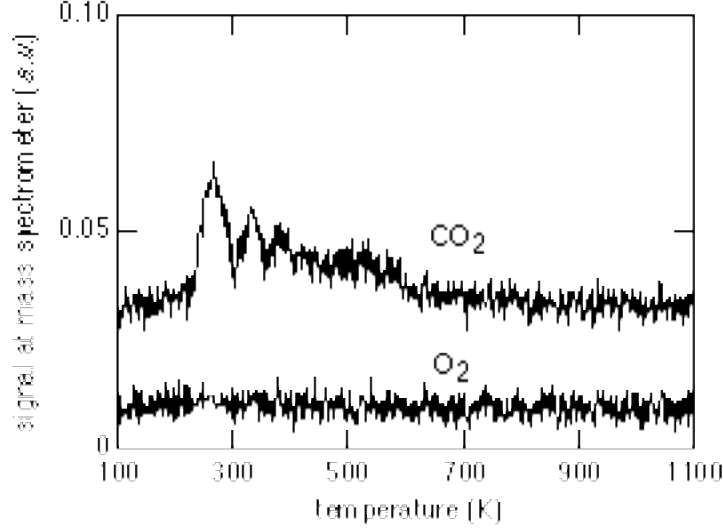
Figure 4.4 Temperature-programmed desorption following irradiation of an O_2/Pt(111) sample with 800-nm, 55-μJ/mm^2 pulses.

4.7 Discussion of the results

Let us now examine different pathways that can lead to O_2 desorption and CO oxidation. First we consider an atomic pathway — oxidation of CO due to interaction with an oxygen atom:

$$O_2(ad) \rightarrow 2O^* \tag{4.3}$$

$$O^* + CO(ad) \rightarrow CO_2(g)$$

The observed ratio of CO_2 formation to O_2 desorption at 800 nm is 1:70 and so, if each time an oxygen molecule dissociates both atoms react with CO, then the ratio of O_2 dissociation to desorption must be about $1/140 \approx 0.7\%$. This is below the upper limit of 1.8% we established for the probability of O_2 dissociation and so we cannot rule out an atomic pathway even though such a pathway would require an efficiency of at least $0.7/1.8 \approx 40\%$ for the capture of the oxygen atoms by CO.

Dissociation of O_2 could also lead to other reactions. However, we observe no recombination of oxygen atoms back to O_2 (column 5, Table 4.2) and no reaction of the dissociation fragments with coadsorbed oxygen atoms (column 6, Table 4.2). So, if

dissociation occurs, we must conclude that the fragments of oxygen dissociated with subpicosecond laser pulses do not react with other oxygen atoms or molecules, in sharp contrast to the oxygen atom formed in the photodissociation of N_2O. [75] The required high capture efficiency of oxygen atoms, and the absence of other reactions between these oxygen atoms and other coadsorbates, suggest that the atomic pathway is not likely to account for the CO_2 yield.

Next we consider a molecular pathway — CO oxidation by direct interaction with an oxygen molecule:

$$O_2(ad) \rightarrow O_2{}^* \tag{4.4}$$

$$O_2{}^* + CO(ad) \rightarrow [CO_3]^{\ddagger} \rightarrow O(ad) + CO_2(g)$$
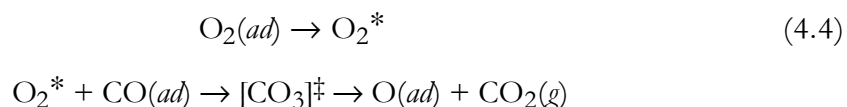
In this scheme, the carbon dioxide is produced not via dissociation of oxygen but through a CO_3 intermediate. A stable CO_3 species has been observed on Ag(110), [80] but has not been reported on Pt(111). In fact, we observe no exchange of the oxygen atom originating on the CO molecule to better than 1 part in 100 (column 4, Table 4.2). Therefore, if CO is oxidized by the molecular pathway, the oxygen atoms of the intermediate must be highly inequivalent and the intermediate is constrained to dissociate into CO_2 and O without eliminating the oxygen initially present on the CO.

It is also possible that the reaction between oxygen and carbon monoxide occurs in a concerted process without involving an equilibrated CO_3 intermediate; instead the O_2 and CO may interact so that the O–O bond is stretched as a new O−CO bond is formed.

Let us next turn to the desorption of oxygen. Suppose the oxygen molecules dissociate and oxygen atoms then recombine to give O_2:

$$O_2(ad) \rightarrow 2O^* \tag{4.5}$$

$$2O^* \rightarrow O_2(g)$$

Such a pathway should lead to mixing of oxygen isotopes in $(^{16}O_2, {}^{18}O_2)/Pt(111)$, but we do not observe this experimentally (column 5, Table 4.2). Furthermore, if they fail to recombine, the oxygen atoms should equilibrate with the surface. However, we observe

very few oxygen atoms in the post-irradiation temperature-programmed desorption experiments. This observation also excludes the possibility [81] that oxygen desorption is caused by displacement due to nearby chemisorption of atomic oxygen. Our observations therefore show that the observed O_2 products are due to desorption of intact molecules.

Columns 1 and 2 of Table 4.2 show that there is yield of CO from CO/Pt(111) and of CO and CO_2 from CO/O/Pt(111) when stimulated with 0.26-ps, 267-nm laser pulses. These yields could be due to thermal desorption induced by laser heating of the phonon modes, or they could be due to laser-excited electrons.

4.8 Conclusions

Our results show that the oxygen molecules desorb from O_2/Pt(111) without exchange of atoms between molecules, like the α-O_2 product in thermal chemistry. We observe no yield of O_2 from O/Pt(111) nor from a reaction between a fragment of O_2 and a coadsorbed, equilibrated oxygen atom in O_2/O/Pt(111).

Our results show that if the CO oxidizes by the atomic pathway, then the capture of oxygen atoms by the CO must be highly efficient. In view of the required high efficiency ($\approx$ 40%) and the absence of other reactions with coadsorbates, however, the atomic pathway is not likely to account for the observed CO_2 yield. If the CO oxidizes by the molecular pathway, then our isotope exchange experiments show that the intermediate has very inequivalent oxygen atoms.

V

Laser-induced oxidation of impurities in platinum

5.1 Introduction

Many papers published between 1974 and 1980 discussed a phase of oxygen on Pt(111) attributed to a platinum-oxide. [82] Annealing the sample at about 1000 K in oxygen created the oxide, which was stable to well over 1300 K. [32, 82] The announcement of such a stable platinum-oxide phase created, "a certain air of spectacle" [82] because thermodynamic data indicate that platinum-oxide is not stable at such high temperatures. It was eventually demonstrated that the oxygen was bound not to platinum, but to silicon segregated on the surface. [82, 83] We have observed an analogous reaction between O_2 adsorbed on a Pt(111) surface and impurities in the sample when the sample is irradiated with 100-fs laser pulses.

The data in Figure 5.1, from Gland *et al.*, show temperature-programmed desorption from a Pt(111) surface that was annealed at high temperature in oxygen. Molecular and recombinative desorption yield oxygen at 140 and 750 K, respectively. When Figure 5.1 was published, the yield of O_2 at 1400 K was attributed to decomposition of a platinum-oxide formed during the anneal. [32] Electron-energy-loss (EELS) data from the annealed

sample exhibited a 760 cm^{-1} vibration that was attributed to phonon modes of platinum-oxide. [32] Ion scattering data from the annealed sample showed that the high-temperature oxygen species is bound beneath the platinum surface. [84]
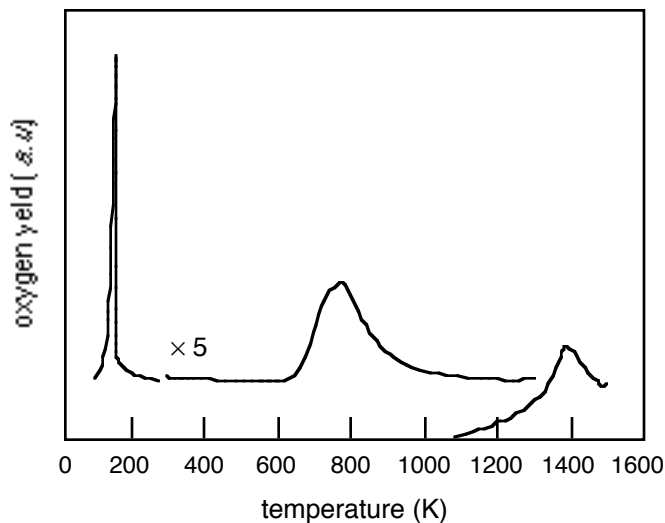
Figure 5.1 Temperature-programmed desorption of a Pt(111) sample after 100 Langmuir exposure to oxygen at 1200 K. The feature near 1400 K was attributed to decomposition of a platinum-oxide. After [32].

Two groups from Jülich, Germany noticed that on one sample it was not possible to produce the "platinum-oxide", while it was easy to make it on another sample that was known to be contaminated with silicon. [82, 83] To confirm that the "platinum-oxide" is related to the silicon contamination, they deposited silicon onto the surface of the sample that did not exhibit "platinum-oxide", and then allowed the silicon to diffuse into the near-surface region by annealing the sample in vacuum. They were then able to create the "platinum-oxide" by annealing the sample in oxygen. They explored this phenomenon using Auger spectroscopy and ion scattering and conclusively demonstrated that the "platinum-oxide" was in fact an oxide of silicon, probably SiO_2. [82, 83] They concluded that "… a truly clean platinum crystal will not form an oxide layer under vacuum conditions at high temperature". [82]

What if the sample is not "truly clean", but only appears to be clean? One of the German groups had a platinum sample that, according to Auger spectroscopy, remained clean even after annealing for 30 minutes in ultra-high vacuum at 873 K. [82] However, annealing for 30 minutes in O_2 at 873 K yielded so much SiO_2 that the silicon and oxygen atoms were clearly visible with Auger spectroscopy. Silicon diffusion explains these results: when the sample is annealed in vacuum, silicon atoms that diffuse to the surface return to the bulk, but when the sample is annealed in O_2, the silicon atoms can be trapped at the surface by reaction with oxygen. According to this model, samples which initially have negligible surface contamination can yield substantial amounts of SiO_2.

In these thermally-activated reactions, continuous dissociative adsorption of O_2 provides a steady-state coverage of oxygen atoms. We have created a similar "oxide" under UHV conditions by irradiating an $O_2/Pt(111)$ surface with 100-fs laser pulses. We use temperature-programmed desorption to analyze the irradiated samples; there is oxygen desorption above 1000 K attributed to thermal decomposition of laser-induced impurity-oxides. It is remarkable that the laser pulses that can so efficiently induce desorption of O_2 can also induce reaction of the O_2 with a low-density contaminant.

5.2 Analysis of the platinum Auger spectrum

Researchers writing about photochemistry on Pt(111) usually claim that sample purity was verified using Auger spectroscopy. However, only rarely [67] do they publish the Auger spectrum and discuss the criteria with which it is analyzed. Phosphorus contamination actually produces an extra peak in one paper, blatantly contradicting the author's claim that all the peaks in the spectrum are due to platinum. [84] In 1985, Mundschau and Vanselow surveyed 70 papers that discussed the reconstruction of ostensibly clean Pt(100). [85] Not one paper contained an Auger spectrum that provided unequivocal evidence of a clean sample. Here we summarize Mundschau and Vanselow's criteria for analyzing Auger spectra from platinum samples and assess the cleanliness of the samples used in the research described in this thesis.

Figure 5.2 shows the Auger spectrum of platinum from the *Handbook of Auger Electron Spectroscopy.* [30] The major peaks, which together could be called the signature of platinum, are labeled. The peaks that are the signatures of common contaminants of platinum are listed in Table 5.1. The Auger signatures of most contaminants are clearly resolved from the peaks due to platinum. Silicon and sulfur are difficult to detect on platinum because their signatures at 92 eV and 152 eV overlap with platinum peaks. A sample can be declared free of sulfur only if the platinum 150- and 158-eV peaks are clearly resolved, as in Figure 5.2. [85] A sample is free of silicon only if the ratio of the height of the 93-eV peak to the height of the 168-eV peak is no larger than is shown in Figure 5.2. [85] To make this comparison, the spectrum must be collected at one gain setting over the range 80 – 180 eV.

Some contaminants are difficult to detect if they are present as an oxide. When calcium, silicon, iron, aluminum, or phosphorus oxidize, their Auger peaks split and shift, making them difficult to detect and identify. It is particularly difficult to avoid forming phosphorus oxide because phosphorus reacts with even 10^{-10} torr oxygen when exposed to an electron beam. When contaminants are oxidized, it may be easier to detect the oxygen than the contaminant. Fortunately, the oxides of platinum are not stable above 900 K, [84] which implies that if the 503-eV signature of oxygen is present after anneal above 900 K, then the oxygen must be bound to an impurity.

Figure 5.2 The Auger spectrum of platinum. Platinum has a more complicated spectrum than most elements. After [30].

Table 5.1 The primary peaks in the Auger spectra of elements that are common contaminants of platinum. Contaminants after [85]; peaks after [30].

common contaminants of platinum	primary Auger peaks	
carbon	272	
phosphorus	120	
silicon	92	
calcium	291	294
aluminum	68	
iron	47	
copper	60	58
sulfur	152	

In summary, the Auger spectrum from clean platinum has the following characteristics: the 150- and 158-eV peaks are clearly resolved (sulfur test); the ratio of the 93-eV peak to the 168-eV peak is as shown in Figure 5.2 (silicon test); there is no 503-eV signature of oxygen following anneal at 900 K (oxide test); no peak listed in Table 5.1 due to carbon, calcium, aluminum, copper, phosphorus, or iron is present.

The ultra-high vacuum chamber used for the experiments described in this thesis is equipped with one instrument for both LEED and Auger (Omicron *Spectaleed 4-grid RFA*). The electron spectrometer is a retarding field analyzer, providing economical Auger capability, though it has far less sensitivity and resolution than the instrument used to obtain the spectrum in Figure 5.2. Figure 5.3 shows Auger spectra from our platinum sample (Princeton Scientific) obtained with the retarding field analyzer. Spectrum *a* was obtained from a dirty sample. Spectra *b* and *c* were obtained following successive cleaning operations described below. The substantial noise that is especially apparent in the 300 – 400 eV range is typical.

Peaks near 270 and 120 eV in Figure 5.3*a* indicate contamination by carbon and phosphorus. Poor resolution of the 150- and 158-eV peaks suggests that the surface is contaminated with sulfur. There may be slight contamination by silicon, but it is difficult to be sure because the baseline plummets at small energies. Elements used in the sample mount, heater body, and thermocouples are listed in Table 5.2. None of these elements is apparent in (*a*), though Auger spectroscopy cannot rule out contamination by gold because the spectra of gold and platinum are very similar. The sulfur and phosphorus must come from the bulk of the crystal because neither of these has ever been admitted to the chamber. Carbon contamination could come from the bulk, or from decomposition of organic compounds used in previous experiments.

The distinct peak near 140 eV in Figure 5.3*a* cannot be attributed to any known contaminant of platinum, nor to any of the elements which comprise the sample mount, heater body, and thermocouples. The only elements which have strong Auger signatures at 140 eV are europium and gadolinium. However, these elements would introduce peaks of roughly comparable intensity to the 140-eV peak at 145 and 108 eV respectively, neither of which is apparent in Figure 5.3*a*. The 140-eV peak does not shift to another energy as the energy of the primary beam is modulated, proving that the peak is not due to primary electrons inelastically scattered from the surface. The 140-eV peak is also not dependent on

the modulation frequency of the spectrum analyzer. These control experiments suggest that Auger electrons cause the 140-eV peak, but it is not possible to conclusively attribute it to europium or gadolinium without being able to resolve other peaks in their Auger signatures. The 140-eV peak may be chemically shifted, further complicating the assignment.
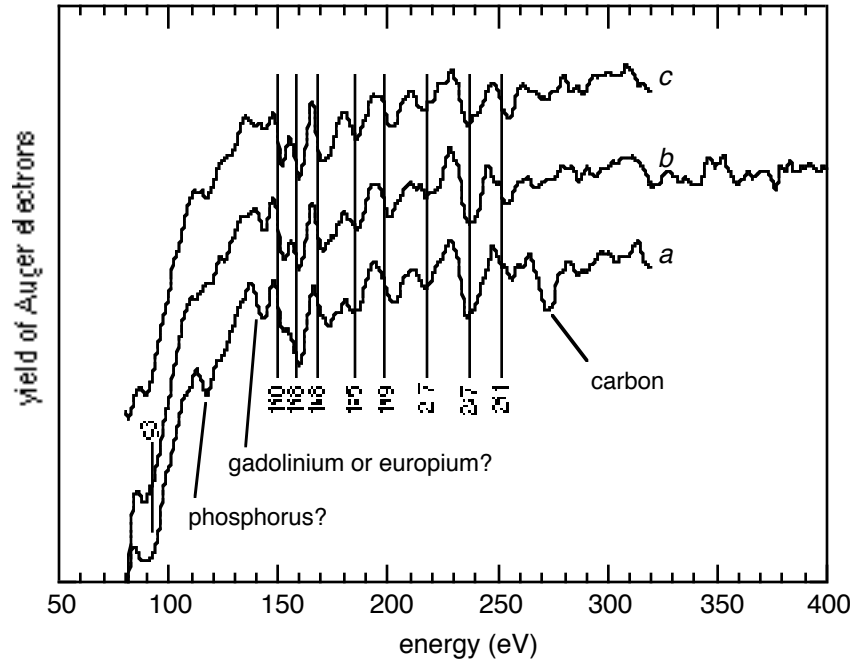
Figure 5.3 Auger spectra of platinum (*a*) after heating at 4 K/s to 1075 K and cooling to 90 K following eight weeks in the 8×10^{-11} torr background of the chamber, (*b*) after 3 minutes neon ion sputtering at 90 K followed by 3 minutes anneal at 1100 K in vacuum, and (*c*) after 15 minutes anneal in 5 $\times$ 10^{-8} torr oxygen at 1000 K followed by 2 minutes anneal in vacuum. Vertical lines indicate the energies where peaks due to platinum are expected. [30] Features due to contaminants in (*a*) are labeled.

Table 5.2 The primary peaks in the Auger spectra of elements that are used in the sample mount, heater body, or thermocouples. Peaks after [30].

elements near the sample	primary Auger peaks		
tantalum	179	166	171
tungsten	179	169	163
gold	239	160	150
chromium	529	489	36
molybdenum	186	221	

Figure 5.3*b* shows that the sample is substantially improved by neon ion sputtering for 3 minutes at 90 K, followed by anneal for 3 minutes in vacuum. The 150- and 158-eV peaks are resolved, indicating reduced sulfur contamination. The 92-eV peak is smaller than it was before sputtering, likely due to removal of silicon. The carbon and phosphorus peaks are gone. The unassigned 140-eV peak is smaller than it was before sputtering. In the 500-eV region of the spectrum, where the signature of oxygen would be expected, no peak is resolved above the noise.

The sample was further treated by 15 minutes anneal in 5×10^{-8} torr oxygen at 1000 K followed by 2 minutes anneal at 1100 K in vacuum. Figure 5.3*c* shows that a fraction of the phosphorus contamination has returned, consistent with reports that annealing platinum causes phosphorus to move from the bulk to the surface. [85] The 140-eV peak is much smaller than it was before the oxygen anneal. It is not possible to conclude that this contaminant is gone, however, because it may still be present as an oxide that contributes a broad distribution of electrons to the spectrum.

Was the Auger spectrum of Figure 5.3*b* obtained from a clean platinum surface? There is no longer any detectable carbon or phosphorus, and it is not likely that phosphorus is disguised as an oxide because no oxygen was admitted to the chamber between spectra *a* and *b*, or indeed for several weeks. The surface now passes the test to be declared free of sulfur. The peak at 93-eV is small enough to rule out contamination by silicon, even after correcting for the steep slope of the baseline. The remaining 140-eV peak, however, may

indicate that the surface is contaminated by europium or gadolinium, or some other element disguised by a chemical shift. The experiments described throughout this thesis were conducted on the surface when the 140-eV peak is present in the Auger spectrum.

The yields in temperature-programmed desorption (TPD) depend on sample impurities. For example, there is no β-O_2 desorbed from O_2/Pt(111) when the sample is contaminated. On the platinum samples used in the experiments described in this thesis, the TPD of oxygen, carbon monoxide, methyl iodide, ethylene, and benzene all match published spectra. The temperature programmed reaction spectroscopy of carbon monoxide coadsorbed with either molecular or atomic oxygen agree with published data. Furthermore, almost all authors report the same cleaning procedure for platinum: sputtering, anneal in oxygen, and anneal in vacuum. These observations suggest that our sample is similar to samples in other laboratories. This similarity alone does not guarantee sample cleanliness, considering the poor record in the literature for documenting sample composition.

5.3 Crystal defects

Low energy electron diffraction (LEED) directly indicates the surface order. The LEED pattern from the clean sample, Figure 5.4*a*, shows the quasi-sixfold symmetry of the (111) crystal surface. The diffraction pattern of the surface with an atomic oxygen overlayer, O/Pt(111), is shown in Figure 5.4*b*. It contains spots due to the platinum atoms and spots due to a p(2×2) overlayer. The patterns do not change as the sample is translated normal to the primary beam. Both diffraction patterns indicate good crystal structure. [67]
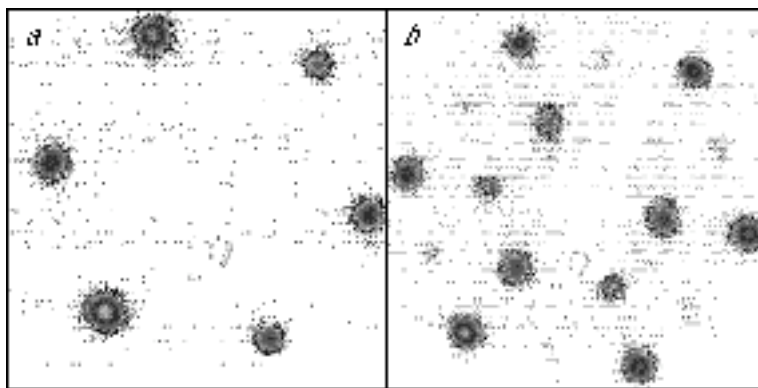
Figure 5.4 Low energy electron diffraction (LEED) from (*a*) clean Pt(111) with primary electron beam energy 110 eV, and (*b*) O/Pt(111) with beam energy 66 eV. The electron gun obscures one of the spots in the O/Pt(111) diffraction pattern. These images are false color digital photographs converted to greyscale; intensity analysis of these images is not possible.

The binding energy of O_2 on platinum depends on the structure of the platinum atoms at the binding site. In a temperature-programmed desorption experiment, the yield therefore reflects the structure of the platinum surface. Figure 5.5*a* shows the temperature-programmed desorption of 0.5 ML O_2/Pt(111). In addition to the well-known yields of α-O_2 and β-O_2, there is yield of O_2 at 230 K. This signal is most likely due to molecular oxygen desorbed from defect sites on the Pt(111) surface. The yield at 230 K corresponds to 0.004 ML O_2. The density of defects could be higher than 0.004 ML, however, because there may be additional defect sites to which the O_2 does not bind. The α-O_2 and β-O_2 peaks have no shoulders, suggesting that they are each due to oxygen desorbed from a single type of binding site.

Figure 5.5*b* shows temperature-programmed desorption from 0.02 ML O_2/Pt(111). There is no yield of O_2 at 230 K. If the O_2 that initially adsorbs on the clean surface occupies the 230 K binding sites first, then it must diffuse to the α-O_2 sites between adsorption at 90 K and desorption of α-O_2 at 140 K. It is more likely that the O_2 occupies

the 140- and 230-K binding sites in proportion to their density. In either case, the data of Figure 5.5 suggest that the density of surface defects is low.
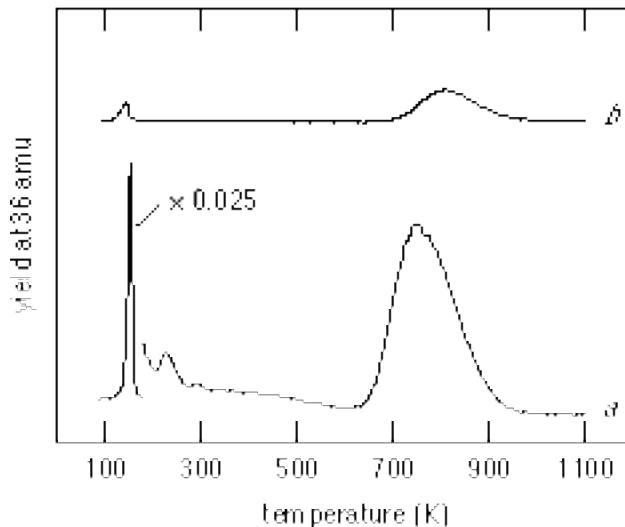
Figure 5.5 Temperature-programmed desorption of $O_2/Pt(111)$ for (*a*) a saturated, 0.5 ML sample preparation and (*b*) a small 0.02 ML coverage of O_2. The yield at 230 K is assigned to desorption of 0.004 ML O_2 from defect sites. There is no scale change in (*b*).

5.4 Subpicosecond-pulsed irradiation of $O_2/Pt(111)$

We conducted experiments on the Pt(111) sample described in the preceding two sections. The sample is cleaned daily with the following procedure: 10 minutes of neon ion sputtering at 800 K, 5 minutes anneal at 1100 K in vacuum, 10 minutes anneal at 500 K in 5×10^{-8} torr $^{16}O_2$, and a flash at 4 K/s to 1100 K. A saturation coverage of $^{18}O_2$ is applied to the surface when the temperature has fallen to 100 K. When several trials are conducted in one day, the anneal in oxygen and the subsequent flash to 1100 K are repeated between trials. In addition to the daily cleaning procedure, the sample is periodically cleaned with 10 minutes of neon ion sputtering at 90 K.

We irradiate the $O_2/Pt(111)$ samples with the 800- and 267-nm output of an amplified Ti:sapphire laser. The 800-nm pulses have 100-fs duration, and the 267-nm pulses have 0.3-ps duration. The sample is exposed to 1000 pulses per second of not more than

150-μJ energy per pulse. The laser pulses have a 500-μm wide spatial profile and are incident 45° from the surface normal. The sample is continuously translated at 350 μm/s to irradiate the entire sample. Each part of the sample is exposed to approximately 2000 laser pulses. Fluences specified below are the fluence absorbed in the platinum for each of the 2000 laser pulses. We monitored sample temperature during irradiation to ensure that the laser pulses do not increase the bulk temperature above 92 K.

5.5 Results of the irradiation

Traces (*b-e*) of Figure 5.6 show the yield of O_2 in temperature-programmed desorption following irradiation of a saturated O_2/Pt(111) sample. For comparison, Figure 5.6*a* shows the temperature-programmed desorption from a saturated O_2/Pt(111) sample without irradiation. Irradiation reduces the total coverage of oxygen. In two of the curves in Figure 5.6, oxygen desorbs above 1000 K. We call the oxygen that desorbs above 1000 K "γ-O_2".

The yield of γ-O_2 is insensitive to the laser wavelength, but does depend on the laser fluence. Figure 5.6*d* was obtained after irradiation of the sample preparation with 50-μJ/mm^2 pulses: γ-O_2 has never been observed following irradiation at fluences less than or equal to 50 μJ/mm^2. Traces (*b*) and (*e*), which do exhibit γ-O_2, were obtained after irradiation with fluences near 70-μJ/mm^2. The yield of γ-O_2 is approximately 10% of the yield of β-O_2 from the unirradiated sample (*a*). The yields of γ-O_2 are not very reproducible — sometimes a sample irradiated with approximately 70 μJ/mm^2 does not yield any detectable γ-O_2.

As a general rule, irreproducible results may be related to sample impurities. To see if oxygen remaining on the sample after cleaning causes the γ-O_2, we compared the yields of $^{18}O_2$ and $^{16}O^{18}O$ following irradiation of $^{18}O_2$/Pt(111). Any oxygen remaining on the surface after cleaning would be the ^{16}O isotope, because the sample is annealed in $^{16}O_2$ as part of the cleaning process. Figure 5.6*c* shows that there is only a small yield of $^{16}O^{18}O$. There is no yield of $^{16}O_2$ (not shown). We conclude that the most of the oxygen that

becomes γ-O_2 originates with the O_2 that is deliberately applied to the sample after cleaning.

Figure 5.7 shows the results of experiments that further investigate the possible role of crystal impurities and defects. We deliberately created defects in the surface by sputtering the clean sample for two minutes at 90 K. We then applied oxygen at 250 K. Figure 5.7b shows that the oxygen desorbs from the defected surface on the low-temperature side of the signal due to β-O_2. To see if the laser creates defects in the surface, we irradiated a clean surface with 70-μJ/mm^2 pulses, and then applied oxygen at 250 K. Figure 5.7c shows that there is no yield of oxygen that can be attributed to desorption from defect sites, suggesting that the irradiation did not create defects.

The yield of β-$^{18}O_2$ from the pre-irradiated surface (Figure 5.7c) is only 65% of the yield of β-$^{18}O_2$ from the non-irradiated surface (Figure 5.7a). Could the laser-induced heating of the surface reduce the stickiness? To investigate the influence of heating the clean surface prior to applying oxygen, the sample was annealed for 1 hour at 1100 K in vacuum. After the sample cooled to 100 K, we applied molecular oxygen. Figure 5.7d shows that only a very small amount of α-O_2 stuck to the sample, suggesting that annealing contaminates the sample. Indeed, the Auger spectrum in Figure 5.8b confirms that this annealed surface is contaminated with silicon, phosphorus, carbon, and possibly calcium.

Curve (e) in Figure 5.7 shows that a clean sample annealed for 10 minutes at 1000 K in oxygen does not yield γ-O_2. The β-O_2 in Figure 5.7e is attributed to oxygen that adsorbed to the surface from the chamber background as the sample cooled after the anneal.
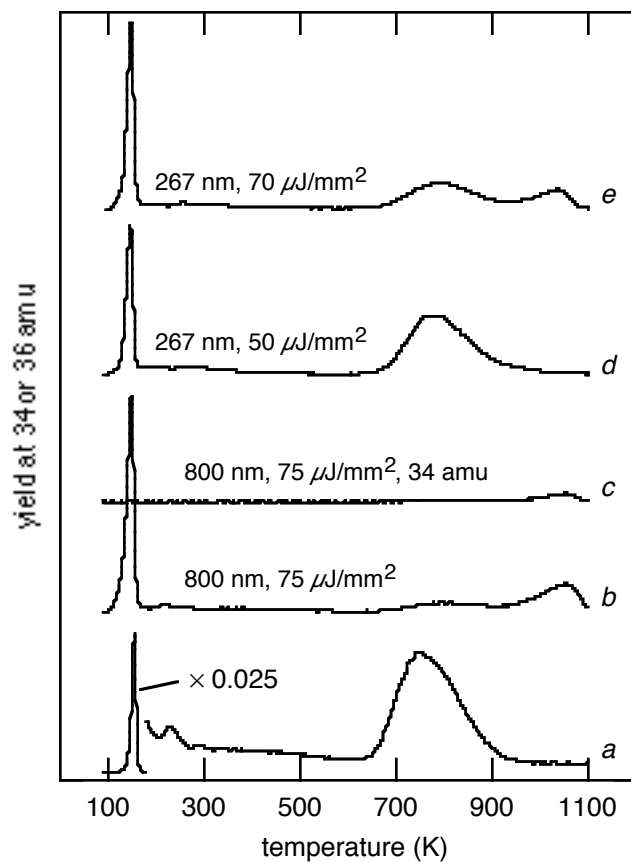
Figure 5.6 Temperature-programmed desorption of a saturated $^{18}O_2/Pt(111)$ surface (*a*) before irradiation, and (*b*–*e*) following irradiation with many subpicosecond laser pulses at the wavelengths and fluences indicated. Curve (*c*) represents the yield of $^{16}O^{18}O$; other curves represent the yield of $^{18}O_2$. There is a scale change in (*a*).
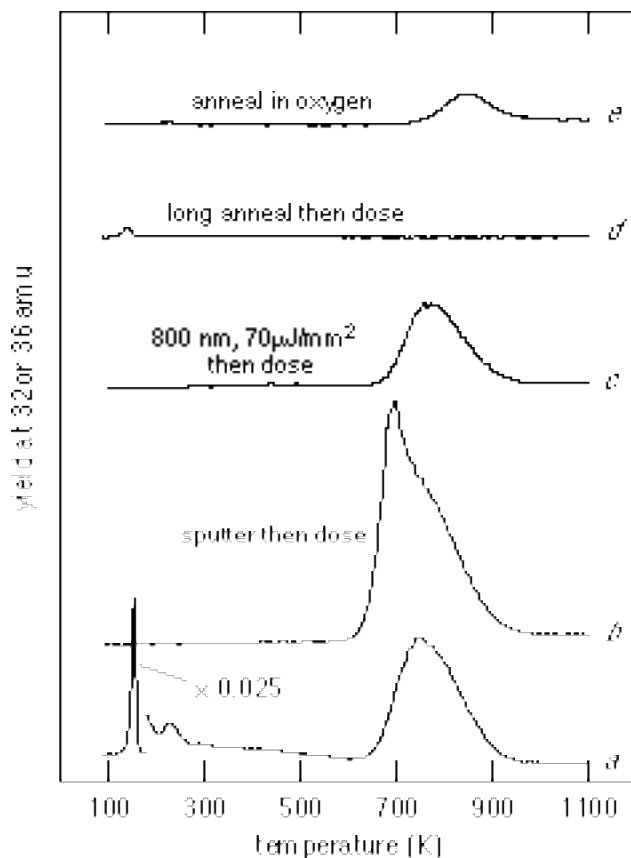
Figure 5.7 Yields of molecular oxygen in temperature-programmed desorption from various imperfect Pt(111) surfaces compared with (*a*) the reference TPD. In (*b*) the surface was sputtered for 2 minutes at 90 K before oxygen was applied at 250 K. In (*c*) the clean platinum surface was irradiated and then oxygen was applied to the sample at 250 K. In (*d*) the clean platinum was annealed for 1 hour at 1100 K in vacuum before oxygen was applied to the sample at 100 K. In (*e*) the clean platinum was annealed for 10 minutes at 1000 K in 5×10^{-8} torr $^{16}O_2$, then cooled to 90 K before the TPD experiment.
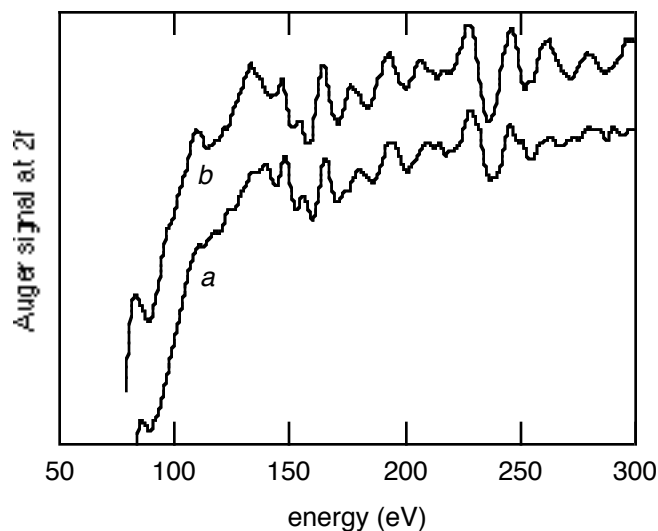
Figure 5.8 The Auger spectrum of (*a*) the clean sample and (*b*) the sample after a one hour anneal at 1100 K in vacuum. The spectrum after the one hour anneal shows that the sample is contaminated by silicon (92 eV), phosphorus (120 eV), carbon (272 eV), and possibly calcium (291 eV).

Figure 5.9*a* shows the LEED pattern from O_2/Pt(111) after irradiation of the entire surface with 800-nm, 75-μJ/mm^2 pulses. There are three components of the diffraction pattern: six features due to the Pt(111); twelve features with an approximately p(2 × 2) pattern (compare with Figure 5.4*b*); and a diffuse background that smudges the peaks. To see if any of these features can be attributed to the portion of the molecular oxygen overlayer that was not desorbed by the laser, we obtained a LEED pattern from O_2/Pt(111) without irradiation. Figure 5.9*b* shows that after about 15 minutes exposure to the 71 eV primary electron beam, the LEED pattern of O_2/Pt(111) has a large diffuse component but no clear p(2 × 2) pattern.

Figure 5.9 Low energy electron diffraction from $O_2/Pt(111)$ (*a*) after irradiation with 800-nm, 75-μJ/mm^2 pulses, and (*b*) without irradiation. The primary beam energies are (*a*) 80 eV and (*b*) 71 eV. These images are false color digital photographs converted to greyscale.
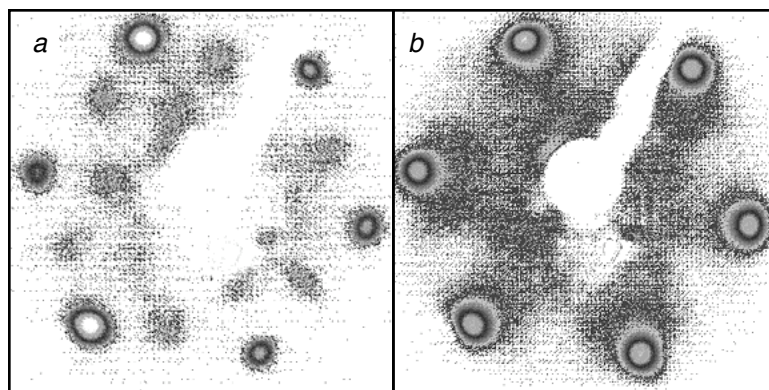
To investigate the possible role of electrons in the surface reaction, we exposed $O_2/Pt(111)$ to 40 eV electrons from the LEED/Auger electron gun for 50 minutes. No γ-O_2 was produced, confirming that the laser induces formation of γ-O_2. This result is not surprising because the γ-O_2 is only formed when the laser fluence is above 50 μJ/mm^2, indicating that the laser is responsible for the reaction.

5.6 Origin of the new thermal desorption feature

The experiments provide strong evidence that the γ-O_2 is not due to oxygen bound at defect sites. According to the LEED pattern of the clean Pt(111) crystal (Figure 5.4*a*) the sample is initially well-ordered. Though oxygen desorption from defect sites is apparent in the temperature-programmed desorption of $O_2/Pt(111)$ from an unirradiated surface (Figure 5.3*a*) the yield is small and the desorption occurs below 300 K. Defects deliberately created by sputtering contribute O_2 to the low-temperature side of the β-O_2 thermal desorption signal. In these two cases, the yield of O_2 from defects occurs far below the 1050 K onset of γ-O_2. Does the laser create surface defects? When a clean surface is irradiated before application of oxygen, the surface produces a smooth β-O_2 thermal desorption signal, suggesting that the laser does not create many surface defects. Finally, the

LEED pattern obtained from the irradiated surface (Figure 5.9*b*) contains sharp diffraction peaks due to atoms in the (111) crystal surface, confirming that the laser does not grossly disturb the crystal structure. For these reasons, crystal defects do not account for the γ-O$_2$.

Could the laser-induced excitation drive the oxygen beneath the top layer of platinum atoms to form a platinum oxide? While the γ-O$_2$ is detected near 1050 K, thermodynamic data show that neither PtO nor PtO$_2$ is stable above 900 K in ultra-high vacuum. [82, 83] The rate of desorption of the oxygen produced by decomposition of the platinum oxide could be limited by the rate of diffusion of the oxygen to the surface. [32] In this case, the oxygen would desorb at a higher temperature than the temperature at which it decomposes under equilibrium conditions. However, this model cannot account for the delayed onset of the oxygen desorption: decomposition of platinum oxide very close to the surface should lead to oxygen desorption as soon as the oxide is no longer thermodynamically stable. Furthermore, at the slow 4 K/s heating rate used in the temperature-programmed desorption experiments, the sample cannot get far from thermal equilibrium. The γ-O$_2$ is not due to decomposition of a platinum oxide.

The oxygen which becomes γ-O$_2$ during temperature-programmed desorption is not bound to the platinum surface at crystal defects, and it is not bound to platinum beneath the surface. The only remaining possibility is that the oxide of an impurity dissociates to produce γ-O$_2$. We saw in section 5.1 that a similar reaction is thermally activated by annealing in oxygen a platinum sample contaminated with silicon.

The impurity that reacts with the oxygen could be present at the surface before irradiation, or it may diffuse to the surface when the laser heats the near-surface region. According to the data in Figure 5.7*c*, the saturation oxygen coverage on an irradiated sample is only 65% of the saturation coverage on a clean surface. This observation suggests that the surface is more contaminated after irradiation than before irradiation, since we know from Auger spectroscopy data (Figure 5.8*b*), and temperature-programmed desorption data (Figure 5.7*d*) that oxygen does not stick to a highly-contaminated surface. Contaminants

segregated on the surface could also account for the haze observed in the LEED pattern following irradiation (Figure 5.9*a*). These results suggest that at least part of the γ-O_2 can be attributed to impurities that segregate on the surface as a result of irradiation.

The yield of γ-O_2 is 10% of the yield of β-O_2 from a 0.25 ML p-(2×2) atomic-oxygen overlayer. If one oxygen atom is bound to one contaminant atom, then the density of impurities after irradiation is 0.025 ML. There could be oxides on the surface after irradiation that do not decompose below 1100 K, and are therefore not observed in the temperature-programmed desorption experiments. These stable oxides would not be counted in the 0.025 ML estimate of the impurity density. (These oxides would be removed by sputtering during sample cleaning.) The impurity responsible for γ-O_2 is not likely to be silicon because silicon oxides decompose near 1400 K. A species not detected by Auger spectroscopy could create the γ-O_2 because the 0.025 ML impurity density estimate is well below the expected sensitivity of the spectrometer.

5.7 The role of the laser pulses

We calculated the response of the platinum to the 70-μJ/mm^2, 100-fs laser pulses, assuming that the electron and phonon temperatures are independent but that the electrons always have a thermal distribution (section 2.10). We found that the electron temperature rises from 90 K to 3300 K during the first few hundred femtoseconds. Over the next few picoseconds the electron temperature falls while the phonon temperature rises to 400 K. At this point the electrons and phonons are equilibrated with each other, and they cool to the 90 K bulk temperature on a 0.1 ns time scale. This behavior is illustrated in Figure 2.24 for different laser parameters. The response of the platinum can be roughly divided into two stages: initially there is a high electron temperature and a low phonon temperature; in the second stage the electrons and phonons at the surface are at the same temperature and are warmer than the bulk of the crystal. Could the thermal energy available during either of these stages account for the formation of γ-O_2?

We were never able to form γ-O_2 under equilibrium conditions. For example, the sample is regularly annealed in oxygen at 500 K as part of the cleaning cycle, but this has never resulted in γ-O_2. The data in Figure 5.7e show that even when the sample is annealed in oxygen at 1000 K, no γ-O_2 is formed. If the γ-O_2 were created during the second stage of the substrate response to the laser pulse — the 0.1 ns period when the surface is hot — then we would expect to create γ-O_2 by annealing the sample in oxygen. The second stage of the substrate response does not account for the formation of γ-O_2.

During the first stage of the substrate response to the laser pulse the electron temperature reaches far above the 2045 K melting point of platinum. (The platinum doesn't melt, of course, because the phonons are cold.) These hot electrons may induce reaction between the adsorbed O_2 and an impurity from the surface or the bulk. The laser pulse may also directly excite the oxygen to induce reaction with impurities present at the sample surface.

5.8 Conclusions

We induced a reaction between O_2 adsorbed on Pt(111) and contaminants of the platinum by repeatedly irradiating the surface with 100-fs laser pulses at fluences above 50 μJ/mm^2. Some of the reactants originate beneath the platinum surface, showing that the laser allows substrate atoms to move.

In section 3.5 we discussed simulations of molecular dynamics at a surface. The adsorbates move on potential energy surfaces that depend, in part, on the configuration of substrate atoms (Figure 3.14). When the substrate atoms are moving, the potential energy surfaces must also change, complicating the molecular dynamics simulations.

The γ-O_2 is not formed under equilibrium conditions. We propose that the reaction requires a very high electron temperature, such as that found for a few picoseconds following excitation with a subpicosecond laser pulse. This elevated electron temperature

may promote formation of γ-O_2 by allowing reactants to diffuse to the surface, or by inducing reaction between oxygen and a reactant on the surface.

VI

Novel microstructuring of silicon with femtosecond laser pulses

6.1 Introduction

Fabrication of even a single layer of a semiconductor device using photolithography requires many steps. Two extensively-studied alternatives to photolithography are laser-assisted dry chemical etching and laser-induced ablation. [86, 87] Both alternatives have the potential to be simpler than photolithography, but experiments with lasers of picosecond duration or shorter have not been able to demonstrate sufficient speed and precision for either alternative to replace conventional photolithography. In this chapter we discuss the first application of femtosecond laser pulses to laser-assisted chemical etching. We have produced a striking surface structure on silicon wafers irradiated with 100-fs laser pulses in Cl_2 or SF_6 gas.

These gases are widely used to etch silicon. For example, liquid silicon reacts with Cl_2 gas to form silicon chloride vapor. Figure 6.1a shows how this reaction can be exploited to etch silicon by locally melting it with a laser pulse. [88] When the peak fluence in the laser profile is slightly above the threshold fluence for melting the silicon, the melted region can

be substantially smaller than the laser's spatial profile. This technique created 40-nm wide structures between 200-nm wide trenches using 350-nm light. [88]

Another chemical etching process requires halogen radicals. [89-91] Chlorine radicals react spontaneously with *n*-type silicon as shown in Figure 6.1*b*. First an electron from the substrate attaches to a chlorine radical and is drawn in to the silicon surface by a surface field. The resulting $SiCl_x$ compounds desorb. [90] The electrons in the substrate are essential to drive the reaction: undoped silicon does not react this way unless it is irradiated to generate free carriers. The etching of undoped silicon is spatially confined to irradiated regions.

A few studies have considered the interaction of chlorine with silicon under well-characterized, UHV conditions. [92, 93] A submonolayer of chlorine saturates the silicon at the surface. Irradiation results primarily in desorption of $SiCl_2$. [93, 94]
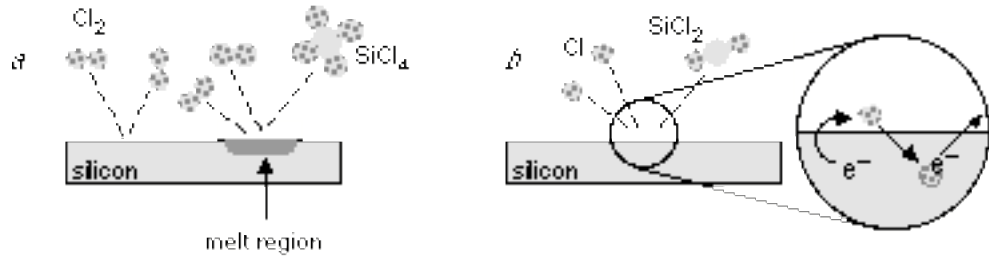

Figure 6.1 (*a*) Cl_2 reacts with liquid silicon, or (*b*) chlorine radicals react with solid silicon. The etching by the radicals is induced when substrate electrons ionize the radicals and the ions are drawn beneath the surface by the surface field.

At high fluences, laser-induced ablation creates structures in a surface, even without chemical reaction. Creation of holes and trenches has been demonstrated. When the laser is pulsed, the surface structures depend on the rapid heating of the surface and the steep spatial gradients of temperature normal to the surface. During re-crystallization, structuring into domains of approximately micrometer size is common. [95, 96] Other laser-induced structural transformation is well-known: amorphous silicon has been made crystalline; [97,

98] crystalline silicon has been made amorphous; [99] and the ultrafast surface melting following femtosecond laser-induced heating has been directly imaged. [100]

Here we describe the creation of arrays of sharp conical spikes by repeatedly irradiating silicon surfaces with femtosecond laser pulses in SF_6 or Cl_2. The spikes form spontaneously without the use of any masks. The production of sharp spikes using femtosecond laser pulses is in contrast to reports that femtosecond laser pulses can create very smooth holes, trenches, and cavities. [101-104] While there are reports that semiconductor, metal, and dielectric surfaces become structured when irradiated with lasers, [96, 105-109] there have been no reports of the sharp spikes we observe.

6.2 Motivation for applying femtosecond laser pulses to chemical etching and ablation

When one part of a semiconductor is irradiated with a laser pulse, neighboring parts of the sample can be damaged. [103] For example, experiments show that the heat from a laser can induce 80 nm migration of dopants. [110] Damage to surrounding regions is minimized if the laser energy is concentrated in a short pulse. In the extreme case of femtosecond laser pulses, energy is deposited in the irradiated region faster than diffusion can carry it away. In contrast, long pulses heat the surrounding regions because energy diffuses away from the irradiated region before the irradiated region reaches the desired temperature. This confined heating with femtosecond laser pulses may allow more precise laser-assisted surgery. [111, 112]

As we saw in Chapter 3, femtosecond laser pulses have a high cross section for photo-induced reaction compared with low-intensity sources. Figure 6.2 reproduces data showing the yield of O_2 desorbed from $CO/O_2/Pt(111)$ by 300-fs, 400-nm laser pulses. The line is an extrapolation of the yields due to the DIET mechanism responsible for low-intensity, linear photochemistry. The observed yield with the femtosecond laser pulses is more than three orders of magnitude greater than the yield with longer pulses. We began these

experiments in part because we wondered if laser-assisted chemical etching is as sensitive to laser intensity as laser-induced desorption.
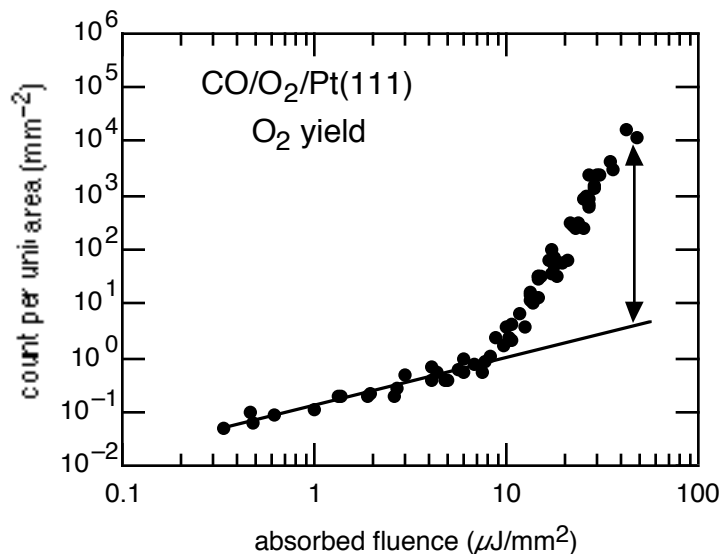

Figure 6.2 The yield of O_2 desorbed from $CO/O_2/Pt(111)$ by 300-fs, 400-nm laser pulses. At high fluences the yield is more than 3 orders of magnitude larger than the extrapolated low-fluence yields.

Femtosecond laser pulses can induce structural transformations in semiconductors which have no counterpart in metals. Consider a semiconductor in which a laser pulse has transferred many electrons from the bonding orbitals to the conduction band. This transition severs the bonds that maintain the crystal lattice, allowing the ions to move. [113] Even at thermal velocities characteristic of the cold lattice, the ions can reach a liquid-like coordination in only a few hundred femtoseconds. This mechanism has been called cold melting, or plasma annealing [114]. Cold melting only occurs when the laser pulse energy is deposited very rapidly. Laser pulses with durations comparable to the timescale for electrons to emit phonons gradually heat the phonon modes, resulting in a traditional thermal melting. The structuring of silicon with femtosecond laser pulses reported in this chapter is conducted at laser fluences for which cold melting is possible.

6.3 Creation of the spikes with femtosecond laser pulses

The Si(100) wafers are *n*-type (arsenic doped) with resistivity less than 5×10^{-5} Ωm. The wafers are cleaned with trichloroethylene, rinsed in acetone, and then rinsed in methanol. The wafers are mounted on a 3-axis translation stage in a vacuum chamber with a base pressure less than 10^{-4} torr. The chamber is backfilled with 500 torr Cl_2, SF_6, N_2, or He.

The samples are irradiated with 500-μJ, 800-nm pulses from a regeneratively amplified Ti:sapphire laser. The pulses are compressed after amplification with a grating-pair compressor. The pulse duration may be varied from 100-fs to several picoseconds by adjusting the compressor. The autocorrelations used to measure pulse duration are smooth and free of pedestals. Except where noted, the laser pulses are incident normal to the sample surface. The laser pulses are focused with a 0.1-m focal-length lens. The spatial profile of the laser pulse is nearly Gaussian, with a 200-μm beam waist at the sample and a fixed fluence (energy per unit area) of 10 kJ/m^2 at the center of the spatial profile. Each spot on the sample surface is exposed to a run of 500 laser pulses. We translate the sample by approximately 1 mm between runs. Following irradiation, the sample is analyzed with a scanning electron microscope (SEM). The SEM micrographs are obtained from a point-of-view normal to the sample surface (0°), parallel to the sample surface (90°) or in between (45°). Samples analyzed parallel to the surface are first cleaved to bisect the laser-induced surface structure. The surface structures resulting from the irradiation are reproducible.

6.4 Description of the spikes

Figure 6.3 shows the sharp conical spikes produced in 500 torr SF_6 viewed at an angle of 45° from the surface normal and viewed parallel to the surface of a cleaved sample. The spikes are roughly aligned in rows. When these spikes are created, they point perpendicular to gravity. The spikes, which are up to 40-μm tall, have cross section of about 6×10 μm^2 near the base tapering down to a diameter of about 0.8-μm near the tip. The spikes, the

tops of which are approximately at the same level as the surrounding surface of the wafer, are capped by a 1.5-μm ball.

Figure 6.4*a* and 6.5*a* show the sharp spikes of Figure 6.3 at a lower magnification. The spike size varies across the irradiated region, reflecting the spatial profile of the laser pulse. In regions of low fluence, towards the edges of the figure, the spikes are smaller and denser than in the center. We obtained similar sharp spikes in 500-torr Cl_2 gas. Irradiation in vacuum produces blunt spikes with irregular sides and rounded tops, as shown in Figures 6.4*b* and 6.5*b*. In the central region, the spikes taper towards the top, reaching 3–5 μm diameter. We obtained similar blunt spikes in 500-torr N_2, or He.

As Figures 6.4 and 6.5 show, the influence of the ambient gas on surface morphology is striking. The spikes are sharper and narrower in SF_6 or Cl_2 than in vacuum. At the low-fluence edges of the figure, it is especially clear that irradiation in SF_6 or Cl_2 results in a finer structure than irradiation in vacuum. Though the surface irradiated in vacuum, N_2, or He is very structured, it does not exhibit the sharp spikes produced in Cl_2 or SF_6.

The spikes are narrower in the top-to-bottom direction of Figure 6.5 than they are in the left-to-right direction. By rotating the polarization of the incident light, we determined that the narrower direction is always aligned with the laser polarization.

All of the results above are obtained with the laser pulses incident normal to the sample surface. We repeated the experiments with the laser pulses incident at 20° and 45° from the normal to the (100) surface. In all cases, the spikes point towards the laser beam; they do not point normal to the surface unless the laser pulses are incident normal to the surface. As further evidence of the independence of the spike formation on crystal axis, we produced spikes very similar to those shown in Figures 6.3, 6.4*a*, and 6.5*a* by irradiation of Si(111) at normal incidence in SF_6.

We also studied spike formation using doped Si(100) samples with dopant concentrations corresponding to resistivities in the range $5 \times 10^{-5} - 1 \times 10^1$ Ωm. However, even at the highest dopant concentration, the initial photo-induced carrier density of about

10^{27} m^{-3} exceeds the 10^{25} m^{-3} carrier density due to the dopants. Indeed, we did not find any dependence on dopant concentration.

Figure 6.6 shows a Si(100) surface after irradiation by 10 laser pulses at 1 kJ/m^2, one-tenth of the peak fluence used to irradiate the samples in Figures 6.3, 6.4, and 6.5. The surface is rippled with a spatial period approximately 60% of the wavelength of the laser. We observed very similar ripples beyond the regions shown in Figures 6.3, 6.4, and 6.5 where the laser fluence is approximately 1 kJ/m^2. These ripples are very different from the spikes observed in the high fluence regions of Figure 6.3, 6.4, and 6.5. The ripples are spaced by less than the laser wavelength, have a much smaller aspect ratio than the spikes, and are wave-like rather than conical.

6.5 Dependence of the spikes on laser pulse duration

The features in Figures 6.3, 6.4, and 6.5 were created with spikes of 100-fs duration. We investigated the dependence of spike size on laser-pulse duration by repeating the experiments with laser pulses between 100-fs and 10-ps duration. Figure 6.7 shows the square root of the mean area per spike (the average spike separation) as a function of the laser-pulse duration. The size of the spikes depends strongly on laser pulse duration: as the pulse duration increases from 100-fs to 500-fs, the size falls precipitously. Pulses of 500-fs duration or more produce features similar to those seen in the edges of Figures 6.4*a* and 6.5*a*.

6.6 How do the spikes form?

Other authors have observed rippling similar to that in Figure 6.6. [107, 108] The rippling has been attributed to scattering from surface roughness and to re-radiation from surface defect sites. [115, 116] Interference between all incident, radiated, or scattered electromagnetic fields causes periodic variation in substrate heating and ultimately periodic surface structure. The spikes observed in the high fluence regions of Figure 6.3, 6.4, and 6.5 are not similar to the ripples.

The asymmetry of the spikes shown in Figure 6.5 can be qualitatively explained by the polarization-dependence of the silicon absorption. The orientation of the laser polarization in Figure 6.5 is such that the sides of the features that face towards the top or the bottom of the page are irradiated with p-polarization, and the sides which face towards the left or right side of the figure are irradiated with s-polarization. Absorption in silicon is higher for p-polarization than for s-polarization. Therefore the sides of the spikes from which the most material has been removed (sides facing the top and bottom of the page) are also the sides which absorb the most light. According to this explanation for the asymmetry in the spikes, the spike formation is at least partly caused by direct local ablation or melting of the silicon by the laser light.
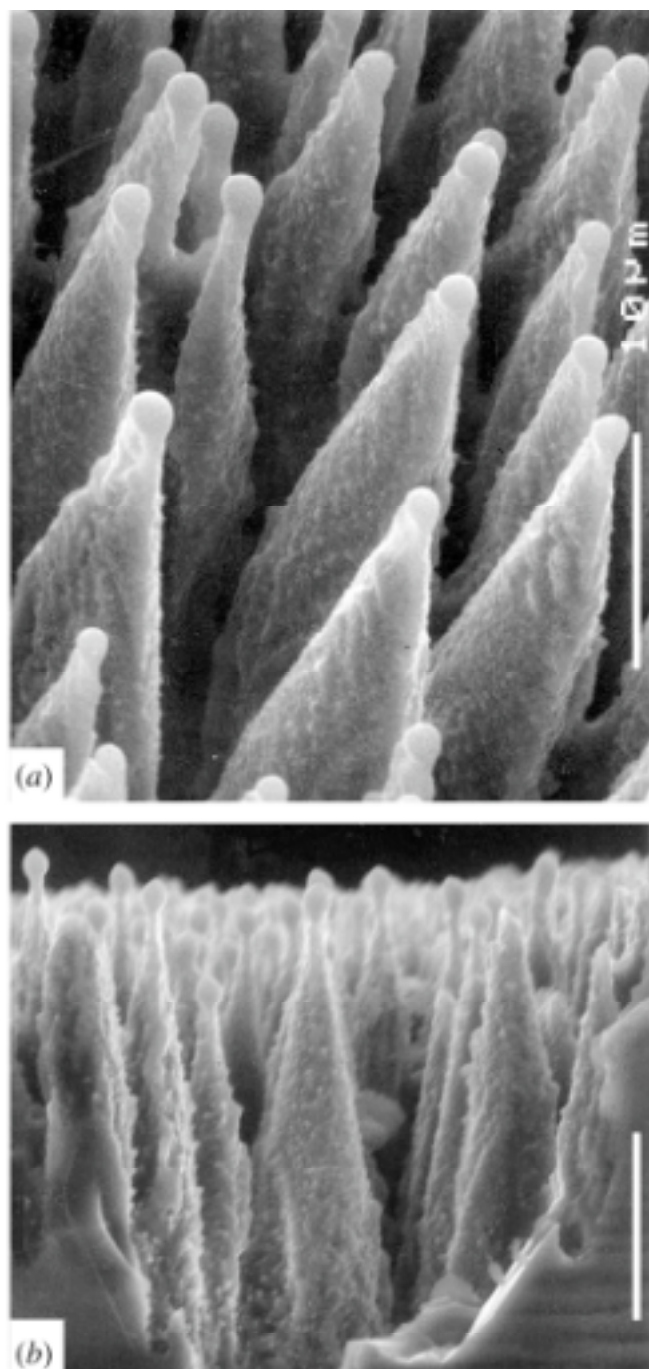
Figure 6.3 Sharp conical spikes produced on Si(100) by 500 laser pulses of 100-fs duration, 10 kJ/m^2 fluence in SF$_6$ at 500 torr viewed (*a*) 45° from the surface normal, and (*b*) parallel to the surface. The scale bars represent 10 μm.
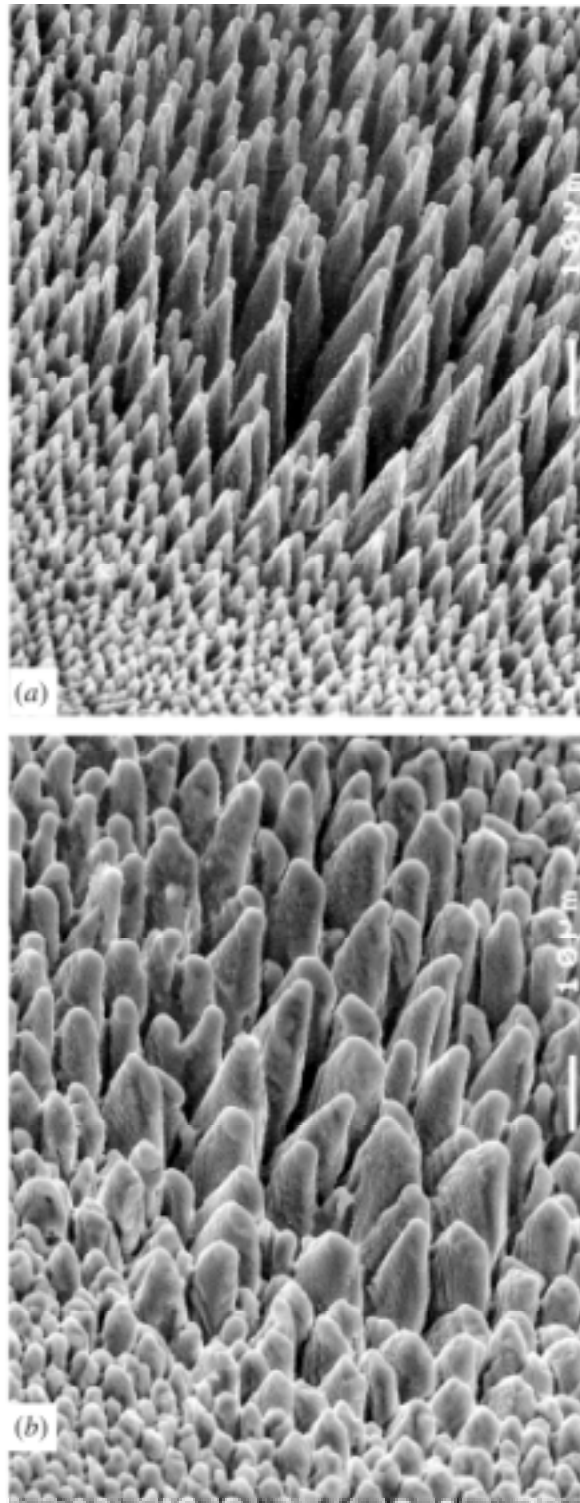
Figure 6.4 Comparison of Si(100) surfaces irradiated in the presence of (*a*) SF$_6$ and (*b*) vacuum viewed at an angle of 45° from the surface normal. The laser spot size is 200 μm in diameter. The scale bars are 100 μm.
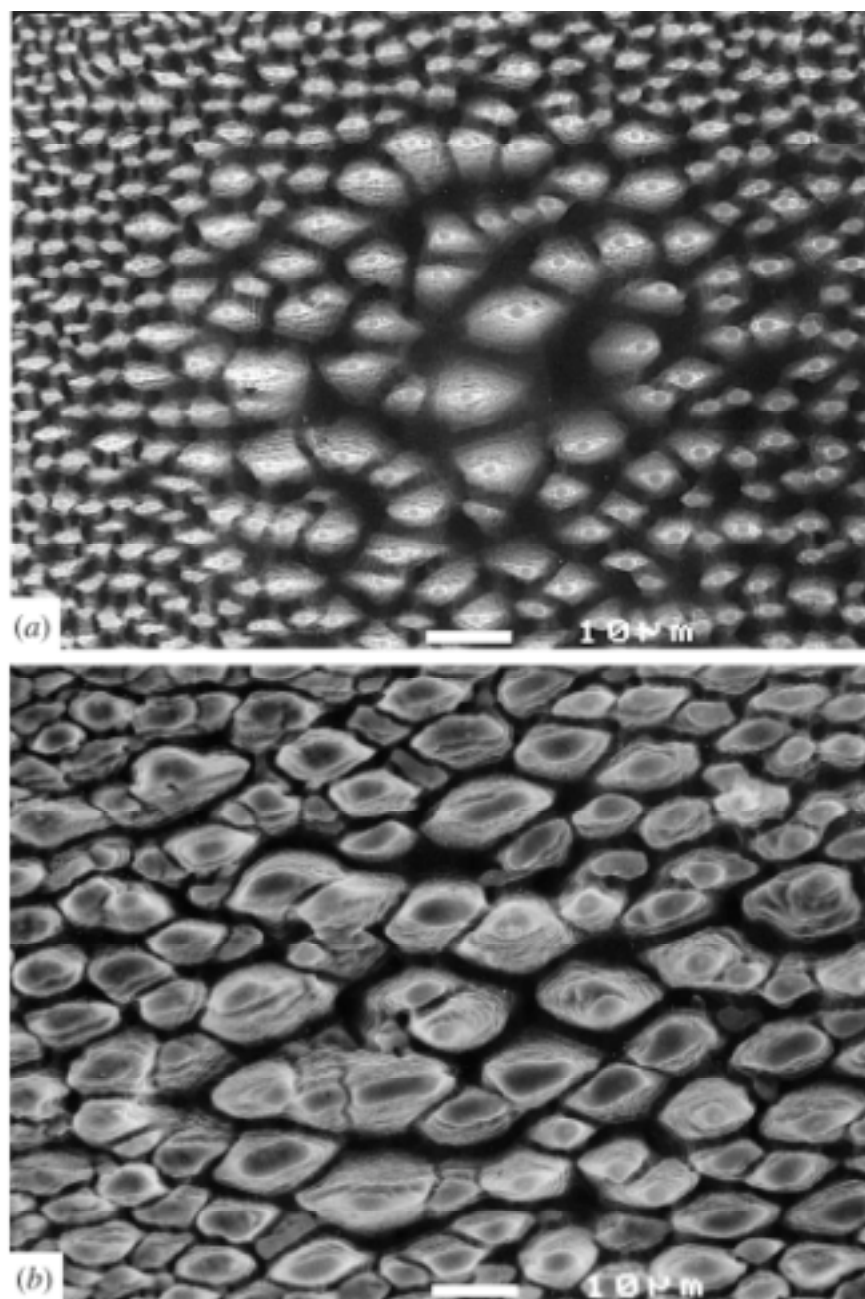
Figure 6.5 Comparison of the surfaces irradiated in (*a*) 500-torr SF$_6$ and (*b*)

vacuum with the same laser parameters as Figure 6.4. The scale bar indicates

10-μm. This view is along the surface normal. The laser light was polarized

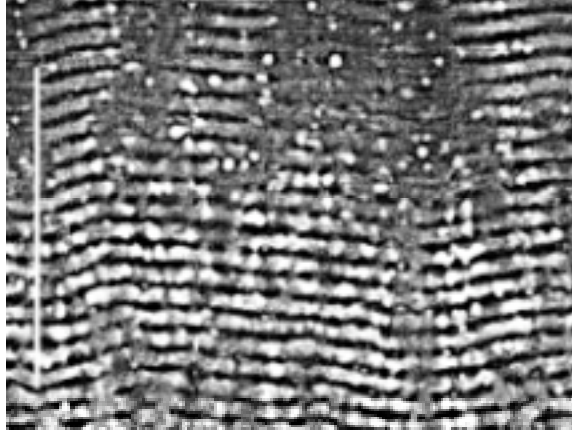in the top-to-bottom direction in the plane of the page.

Figure 6.6 SEM micrograph of the silicon surface following irradiation in vacuum with 10 pulses of 800-nm wavelength, and 100-fs duration. Similar ripples are observed on the samples with the spikes, beyond the regions shown in Figures 6.3, 6.4, and 6.5 where the fluence is approximately 1 kJ/m^2.
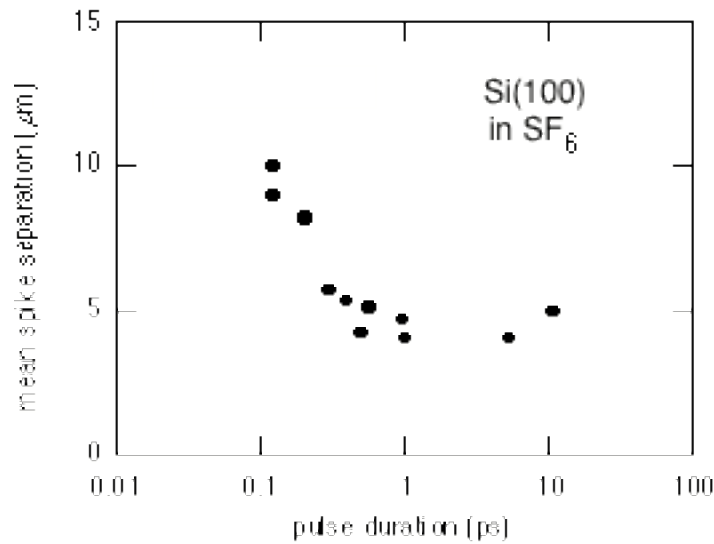

Figure 6.7 The square root of the mean area per spike (equivalent to the mean spike separation) is plotted against the duration of each laser pulse. We analyzed cleaved samples, such as Figure 6.3*b*, to determine that the mean spike separation is strongly correlated with the mean spike height.

We have considered and rejected the idea that the spikes may completely melt and reform on each successive laser shot. Even if all the light incident (10 kJ/m^2) on the area occupied by a one of the largest spikes (8×10^{-11} m^2) is absorbed by the spike, the temperature increase of the silicon within the spike volume (10^{-15} m^3) is only 750 K, assuming uniform energy density and heat capacity 1.64×10^6 J/Km^3. The spike temperature will not reach the 1683 K melting point of silicon. Furthermore, it would not be possible to account for the observation that the spikes point towards the incident direction of the laser pulses; after melting the only unique axes which could define the spike direction are the gradient in silicon temperature, which is almost coincident with the surface normal, and the surface normal itself. Rather than melting and reforming on each laser pulse, the spikes must develop successively over many laser pulses.

Some of the phenomena we observe are similar to reported phenomena using low-intensity sources. Blunt spikes similar to those we observe in vacuum, N$_2$, or He, have been reported by several groups. [96, 97, 103, 105] According to one model, blunt spikes are formed from super-cooled liquid silicon as the recrystallization front propagates towards the surface at different rates in different locations. [109] Okano *et al.* observed that chemical etching is independent of crystal orientation when the silicon has a high carriers density. [90] At low intensities, etch rates do depend on crystal orientation. [117] Our laser pulses create a very high carrier density, and so it is not surprising that we don't see any dependence on crystal orientation.

A striking feature of the spikes created in SF$_6$ and Cl$_2$ is the spherical cap. To see if the top of the spherical cap is a remnant of the native-oxide layer, we rinsed some samples in an aqueous solution of 2% HF to remove the native-oxide layer immediately before putting them in the vacuum chamber. The spherical caps, however, appear regardless of the presence of a native-oxide layer. The spherical shape of the caps suggests that they are due to recrystallization of a liquid silicon drop before the liquid can wet the sharp spike.

The influence of the ambient gas on the shape of the spikes indicates that chemical reaction between SF_6 or Cl_2 and silicon contribute to the formation of the sharp spikes. If the role of the gas were purely physical, such as an influence due to pressure or small heat conduction, then sharp spikes should also form in He or N_2, not just in SF_6 or Cl_2. Several reactions between silicon surfaces and halogenated gases are known. The silicon can react with free radicals created by photo-dissociation of SF_6 or Cl_2, producing volatile silicon halides. [87] The rate of this reaction can be increased by photo-exciting carriers in the silicon. [89] Alternatively, liquid silicon can react spontaneously with Cl_2. [88] Either of these reactions could contribute to the formation of the sharp spikes.

There are several phenomena which may contribute to the strong dependence of spike height on pulse duration. The absorption of the silicon may be nonlinear at the highest laser intensities, [103] in which case the dependence on pulse duration reflects the rapid increase in energy deposited in the silicon as the pulses become shorter. Whether the absorption is linear or nonlinear, there could be a threshold for explosive sublimation of material, perhaps causing material to be swept away by the shock front. Some authors claim that a semiconductor is subject to a rapid phase change known as cold melting, or plasma annealing when excited with laser pulses shorter than a picosecond. [113, 114, 118] The structuring of the silicon may be enhanced when the silicon passes through this phase. Finally, there are many photochemical reactions that have a dramatic increase in cross section when the pulse duration is subpicosecond. [1, 57] We do not know which, if any, of these mechanisms causes the spike size to be so dramatically dependent on laser pulse duration.

6.7 Potential applications of the spikes

Many materials emit electrons when a strong DC bias is applied between the material and an anode. The field emission is greatly enhanced by the concentration of electric field where the material tapers to a point. [28] Field emission has been demonstrated from a cone-shaped structure with a 1-μm diameter polycrystalline diamond ball on top. This spike

was created by deposition of silicon from the vapor phase, and the diamond ball was applied in a separate step using chemical vapor deposition. [119] Though we have not yet demonstrated field emission from the sharp spikes in Figure 6.3, the similarity of the sharp spikes to known field emitters is promising. An array of field emitting points could be used to construct an extremely energy-efficient television or computer display.

Currently, field-emitting arrays are created by condensing the emitter material from the vapor phase onto a patterned substrate. [120] They are also created by using photo-lithography to create a mold in which the emitting material is deposited. [121, 122] High-current field emitters are created by electron-beam evaporation of carbon to produce nanometer-scale carbon tubes. [123] Finally, amorphous diamond deposited on silicon is sharpened in to cones with radii as small as a few nanometers by sputtering in argon ions. [124] None of these techniques has yet been adapted to produce commercial quantities of field-emitting arrays.

Our laser-treatment of the silicon is a simple way of roughening micrometer-sized patches of the surface. Rough surfaces bond better than smooth surfaces; a locally-roughened surface may be useful to help attach contacts to semiconductor devices. Rough surfaces also absorb more light than smooth surfaces. This feature may make our laser-treatment appropriate for the surfaces of solar-power cells.

6.8 Conclusions

We have created sharp conical spikes on a silicon surface irradiated with 10-kJ/m^2, 100-fs laser pulses. The spikes develop successively over 500 shots without melting and regrowing on each laser pulse. Based on the polarization-dependent asymmetry of the spikes, and their orientation with respect to the laser beam, we conclude that local absorption of the laser pulse determines the local changes in the silicon. A spherical cap perched on top of each spike is most likely caused by liquid silicon that recrystallizes before it can wet the spike.

These experiments are conducted at fluences above the damage threshold of silicon in vacuum, in the regime where ablation of the silicon is substantial. However, we also know that chemical reaction is important for the spike evolution because the spikes form in SF_6 or Cl_2, but not vacuum, N_2, or He. High laser fluence is not sufficient to induce formation of large spikes; spike size drops substantially as the laser pulse duration is increased from 100 fs to 500 fs.

Electron-beam-induced oxidation of benzene in $C_6H_6/O_2/Pt(111)$

A.1 Background

This appendix describes ongoing experiments that investigate reaction of benzene and O_2 to make phenol (C_6H_5OH). The phenol is formed when $C_6H_6/O_2/Pt(111)$ is exposed to an electron beam. In contrast, no phenol is formed from $O_2/C_6H_6/Pt(111)$. This appendix concludes with proposals for the next experiments.

The industrial process for converting benzene to phenol is called the "Cumene" process. Cumene is benzene with a $CH(CH_3)_2$ group substituted for one of the hydrogen atoms. Molecular oxygen inserts into the C-H bond of the propylene group to yield cumene hydroperoxide that subsequently decomposes in sulfuric acid solution to yield phenol and acetone (CH_3COCH_3). In the laboratory, the reaction is also driven electrolytically in fuel cells, [125] and with ultraviolet radiation in the gas phase, [126] but neither process has sufficient yield to merit industrial application.

Gas-phase benzene has a negative-ion resonance 4.8 eV above the vacuum level due to a π^* orbital. [127] High resolution electron-energy-loss spectroscopy shows that when benzene is chemisorbed on Pt(111) this orbital is located 2.1 eV above the vacuum level, or 6.5 eV above platinum's Fermi level. It had been speculated that photo-excitation of electrons in to this state should induce desorption or dissociation: experiments with low-intensity irradiation subsequently showed that the benzene is not photo-active. [128]

Electrons with energies in the range 150 – 2000 eV dissociate benzene on W(110) to yield H^+ ions. [129] Electrons are also known to induce surface reaction between O_2 and coadsorbates. For example, O_2 reacts with NO to form NO_2 when $NO/O_2/Pt(111)$ is stimulated with 6 – 350 eV electrons. [130] There have been no previous reports of electron-beam induced reaction of benzene with O_2 in $C_6H_6/O_2/Pt(111)$.

A.2 Sample characterization and electron-beam experiments

The experiments are conducted on the Pt(111) sample described in chapter 5. Molecular oxygen, atomic oxygen, benzene (C_6H_6), or phenol (C_6H_5OH) are adsorbed onto the platinum surface as soon as the surface has cooled following a cleaning cycle. The sample is sputtered and annealed in oxygen between experiments to remove graphitic carbon. The benzene (Aldrich, 99.8%, anhydrous) is purified by repeated freeze/pump/thaw cycles: freezing it with a liquid nitrogen bath, pumping on the vapor remaining in the flask, and then thawing the frozen benzene. Benzene contamination is removed from the phenol (Mallinckrodt 99.1%) by evacuating the volume containing the crystals a few minutes prior to use. The purity of the benzene and phenol is verified with the mass spectrometer. All adsorbates are deposited using a tube facing the platinum surface to reduce background pressure. Samples are analyzed by temperature-programmed desorption with a 4 K/s heating rate.

Figure A.1 shows temperature-programmed desorption of $C_6H_6/Pt(111)$ prepared by applying benzene to the surface at 200 K. The structure in the desorption peaks in Figure A.1 is consistent with other reports. [131] On a truly clean Pt(111) surface, benzene adsorbs molecularly and is aligned almost parallel to the surface. [132, 133]
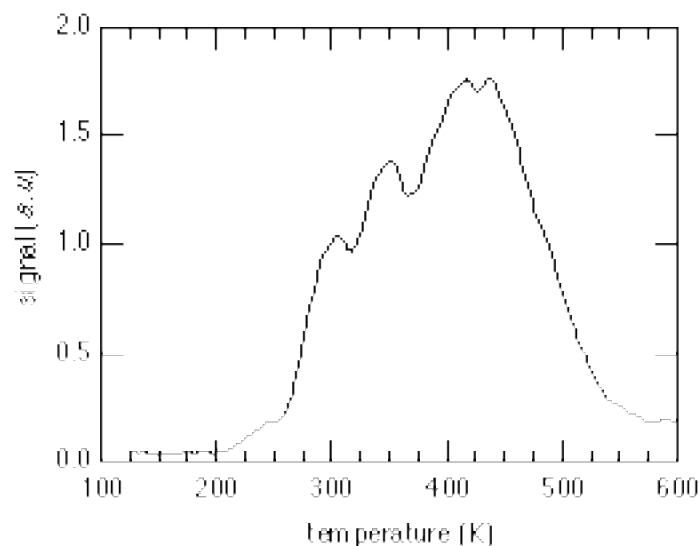
Figure A.1 Temperature-programmed desorption of benzene (78 amu) from C_6H_6/Pt(111).

To make a C_6H_6/O_2/Pt(111) sample preparation, molecular oxygen is applied to the platinum as soon as the temperature has fallen to 100 K following a cleaning cycle. The benzene is applied after the oxygen. Figure A.2 shows that most of the benzene desorbs below 250 K, confirming that the benzene does not displace the oxygen and chemisorb on the platinum surface. The oxygen desorbs over a wide temperature range compared to desorption from O_2/Pt(111), probably because the benzene overlayer inhibits the desorption. Figure A.2 also shows that there is no thermally-induced formation of phenol from C_6H_6/O_2/Pt(111).

Benzene and oxygen are applied in the opposite order to make O_2/C_6H_6/Pt(111). The benzene is deposited while the sample temperature is held at 250 K, immediately following a cleaning cycle. Then the sample is cooled to 100 K and O_2 is deposited. Figure A.3 shows that the benzene remains chemisorbed on the platinum surface when the O_2 is deposited. The yield of O_2 at 210 K indicates that oxygen sticks to C_6H_6/Pt(111), but that it desorbs at a higher temperature than from O_2/Pt(111). There is no thermally-induced yield of phenol from O_2/C_6H_6/Pt(111).

128
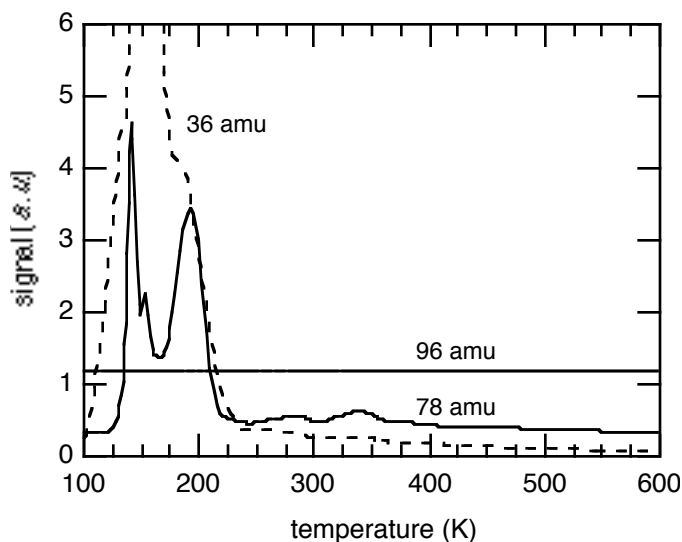
Figure A.2 Temperature programmed reaction spectroscopy of $C_6H_6/O_2/Pt(111)$.

We exposed $C_6H_6/O_2/Pt(111)$ at 84 K to 20 eV electrons from the LEED/Auger electron gun by operating the gun at 100 eV and electrically biasing the sample at $-$ 80 V. Figure A.4*a* shows the yield of phenol after 15 minutes exposure to the electrons. The phenol desorbs at 220 K. We also exposed $C_6H_6/O_2/Pt(111)$ to approximately 70 eV electrons from the ionizer of the mass spectrometer. Figure A.4*b* shows the yield of phenol after 90 minutes exposure. In contrast, Figure A.4*c* shows that when the benzene and the oxygen are applied in the opposite order, $O_2/C_6H_6/Pt(111)$, exposure to electrons does not yield phenol.

Sometimes a mass spectrometer detects fragments of an ion that falls apart in the ionizer. The 96-amu signal in Figure A.4 is not likely due to fragmentation of a heavier ion because there are no species present in the background of the chamber with mass greater than 96. To see if the 96-amu signal could be due to contamination of the benzene or oxygen gases, we analyzed these gases with the mass spectrometer; they do not contain phenol, nor any heavier species. We therefore conclude that the 96-amu signals in Figure A.4 are due to phenol formed from the benzene and the oxygen.
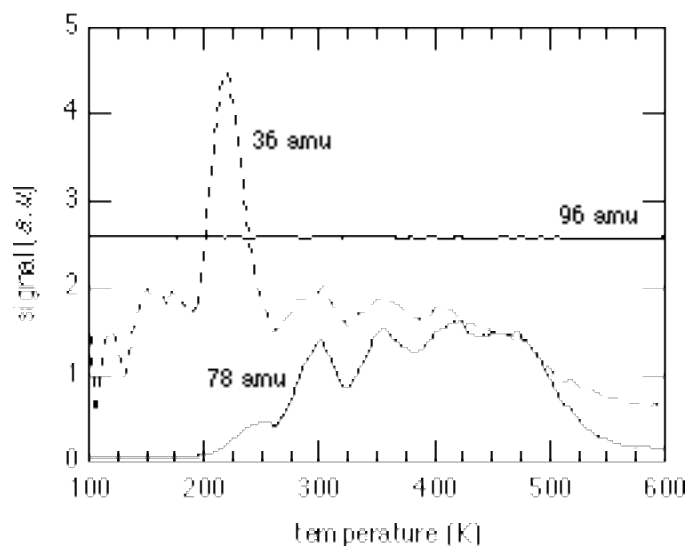
Figure A.3 Temperature programmed reaction spectroscopy of $O_2/C_6H_6/Pt(111)$.

Could the yield of phenol in Figures A.4*a* and A.4*b* be due to thermal reaction during the temperature-programmed desorption? Figure A.2 shows that no phenol is formed from temperature-programmed desorption of $C_6H_6/O_2/Pt(111)$. To further confirm that a slow thermal reaction does not create phenol during the time required to expose the sample to electrons, we maintained a $C_6H_6/O_2/Pt(111)$ sample at 84 K for 90 minutes while shielding it from all electron sources. After 90 minutes, temperature-programmed desorption did not yield any phenol. We therefore conclude that the yield of phenol in Figure A.4 is due to a reaction between O_2 and C_6H_6 that is induced by the electrons.

We created a saturation coverage of chemisorbed $C_6H_5OH/Pt(111)$ by applying phenol to Pt(111) at 170 K. Figure A.5*a* shows that the phenol desorbs at 240 K. Some of the phenol decomposes to yield benzene (Figure A.5*b*). We created a physisorbed layer of phenol on Pt(111) by applying phenol at 100 K. Figure A.5*d* shows that physisorbed phenol desorbs at 190 K. Greater exposures of phenol than used in Figure A.5*d* yield very large 190 K desorption peaks. The yield of phenol induced by the electrons (Figure A.4*a*) is 11% of the yield of phenol from $C_6H_5OH/Pt(111)$ (Figure A.5*a*).

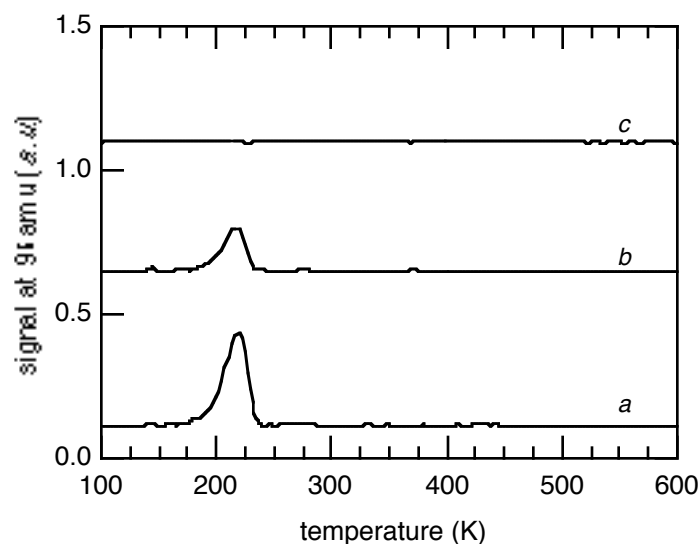**Figure A.4** The yield at 96 amu attributed to phenol from (*a, b*) $C_6H_6/O_2/Pt(111)$ after (*a*) exposure for 15 minutes to 20 eV electrons from the LEED/Auger electron gun, and (*b*) exposure for 90 minutes to approximately 70 eV electrons from the ionizer of the mass spectrometer. (*c*) There is no yield at 96 amu from $O_2/C_6H_6/Pt(111)$ exposed to electrons from the mass spectrometer.

Neither of the phenol desorption peaks in Figure A.5 is at the same temperature as phenol created by surface reaction, Figure A.4. The phenol desorption temperature after the electron-beam-induced reaction may be affected by the coadsorbed O_2 and C_6H_6 that did not react. Indeed, we determined that the desorption of phenol from $C_6H_5OH/O_2/Pt(111)$ is greatest at 210 K. Another possible explanation for the different phenol desorption temperatures in Figures A.5 and A.4 is that the electron beam may create an intermediate species that only turns in to phenol during the temperature-programmed desorption. In this case, the phenol would not necessarily be observed at its molecular desorption temperature.

We also studied benzene coadsorbed with atomic oxygen, $C_6H_6/O/Pt(111)$ and did not detect any thermally-induced or electron-beam-induced phenol.

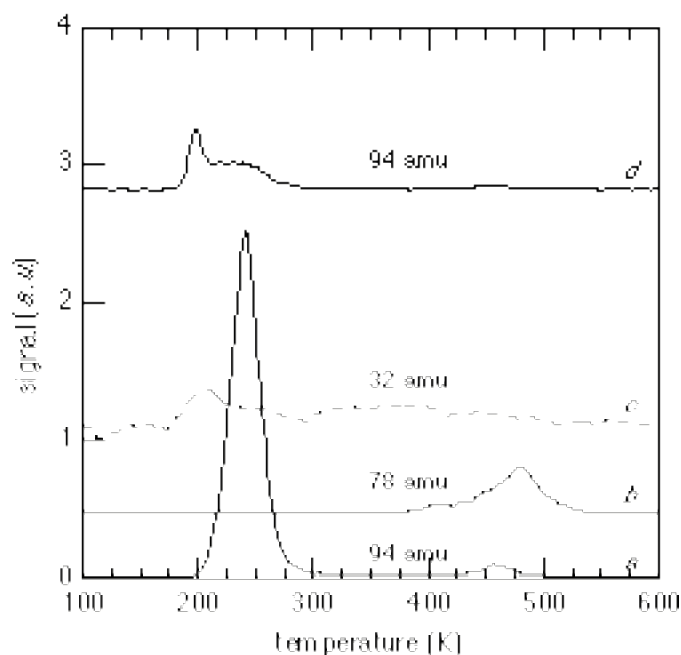**Figure A.5** Temperature-programmed desorption of $C_6H_5OH/Pt(111)$ prepared by (*a–c*) application of phenol at 170 K or (*d*) application of phenol at 100 K.

A.3 Interpretation of the data

The experiments show that phenol is produced when $C_6H_6/O_2/Pt(111)$ is exposed to electrons with energies in the approximate range $20 - 70$ eV. At least some of the phenol sticks on the sample surface and is detected later with temperature-programmed desorption. The data show that the phenol is not formed by thermal reaction from O_2 and C_6H_6 during the temperature-programmed desorption, nor is the phenol formed by slow thermal reaction during the time required to expose the sample to the electrons. Phenol is formed when the sample is placed in front of either the mass spectrometer or the LEED/Auger electron gun, further confirming that electrons induce the reaction.

Perhaps the electrons dissociate O_2 in $C_6H_6/O_2/Pt(111)$, producing energetic oxygen atoms that insert into a benzene C–H bond. This proposal is reasonable because oxygen atoms released by dissociation of O_2 have a high translational energy (see chapter 4). Within this model there are two explanations for the absence of phenol from $O_2/C_6H_6/Pt(111)$

132

and $C_6H_6/O/Pt(111)$: either the electrons are unable to create energetic oxygen atoms on these surfaces, or the geometric arrangement of the oxygen and the benzene does not promote reaction.

The electrons may cause intact O_2 to react with C_6H_6 and form a peroxide intermediate. This peroxide could decompose to phenol during the temperature-programmed desorption. A spectroscopic technique such as electron-energy-loss spectroscopy (section 2.14) could be used to look for a peroxide intermediate.

A.4 Future experiments

The assignment of the 96-amu temperature-programmed desorption signal to phenol currently relies on a plausibility argument: there is no other species which could produce a 96-amu ion. A more conclusive assignment could be reached by comparing the cracking pattern of phenol with the relative yields of the same fragments during the temperature-programmed desorption. We currently have temperature-programmed desorption data for only the 96-amu ion.

In the experiments completed so far, neither the energy distribution of the electrons, nor their total flux is well known. We are therefore not able to determine the yield of phenol as a function of the electron energy, $Y(E)$. The yield will be highest when the electrons (or secondary electrons generated in the substrate) have the same energy as an adsorbate affinity level. If $Y(E)$ has a resonance, the energy of the resonance will indicate the energy of the relevant affinity level in the adsorbate. If $Y(E)$ is very broad, it may indicate that the reaction is driven by secondary electrons from the substrate. The first step in determining $Y(E)$ is characterizing the electron beams by determining the flux of electrons at a given energy.

The sample preparations should also be better characterized. To properly compare experiments on $C_6H_6/O_2/Pt(111)$ with $O_2/C_6H_6/Pt(111)$, we should determine the relative amounts of benzene and oxygen in each preparation. It is also important to estimate the depth of the physisorbed adsorbates because the adsorbates may prevent penetration of

the electrons to the substrate, and thereby complicate interpretation of the experiments. The scattering length for $0 - 10$ eV electrons in condensed benzene is approximately 8 Å, so electron attenuation will not be problem if the adsorbates are only a few layers thick. [134]

REFERENCES

1. S. Deliwala, R. J. Finlay, J. R. Goldman, T. H. Her, W. D. Mieher, E. Mazur, *Chem. Phys. Lett.* **242**, 617-622 (1995).

2. R. J. Finlay, S. Deliwala, J. R. Goldman, T. H. Her, W. D. Mieher, C. Wu, E. Mazur, in *Laser Techniques for Surface Science II* . (1995), vol. 2547, pp. 218-226.

3. R. J. Finlay, E. Mazur, in *to appear in Molecular spectroscopy on the ultrafast dynamics of quantum systems: physical processes and spectroscopic techniques* B. DiBartolo, Ed. (Plenum, New York, 1998).

4. R. J. Finlay, T.-H. Her, S. Deliwala, W. D. Mieher, C. Wu, E. Mazur, in *Femtochemistry: Ultrafast chemical and physical processes in molecular systems* M. Chergui, Ed. (World Scientific, Singapore, 1996) pp. 457-464.

5. T.-H. Her, R. J. Finlay, C. Wu, E. Mazur, *to appear in J. Chem. Phys.* (1998).

6. R. J. Finlay, T.-H. Her, C. Wu, E. Mazur, in *Femtochemistry and Femtobiology: Ultrafast Reaction Dynamics at Atomic-Scale Resolution* V. Sundstrom, Ed. (Imperial College Press, London, 1998).

7. R. J. Finlay, T.-H. Her, C. Wu, E. Mazur, *Chem. Phys. Lett.* **274**, 499-504 (1997).

8. T.-H. Her, R. J. Finlay, C. Wu, E. Mazur, *submitted to Appl. Phys. Lett* .

9. T.-H. Her, R. J. Finlay, C. Wu, E. Mazur, S. Deliwala, Novel microstructuring of silicon with femtosecond laser pulses, Optical Society of America, Long Beach, CA (1997).

10. M. Tinkham, *Group theory and quantum mechanics* (McGraw-Hill, New York, 1964).

11. C. Kittel, *Introduction to Solid State Physics* (John Wiley and Sons, New York, ed. 6th, 1986).

12.   N. W. Ashcroft, N. D. Mermin, *Solid state physics*. D. G. Crane, Ed. (Saunders College, Philadelphia, 1976).

13.   J. J. Sakurai, *Modern quantum mechanics*. S. F. Tuan, Ed. (Addison-Wesley, New York, 1985).

14.   B. Segall, *Phys. Rev.* **124**, 1797 (1961).

15.   G. A. Burdick, *Phys. Rev.* **129**, 138 (1963).

16.   G. Leschik, R. Courths, H. Wern, S. Hüfner, H. Eckardt, J. Noffke, *Solid State Comm.* **52**, 221-225 (1984).

17.   J. H. Weaver, C. Krafka, D. W. Lynch, E. E. Koch, *Optical Constants of Materials, Part 1, Physics Data* (1981).

18.   P. N. Ray, J. Chowdhuri, S. Chatterjee, *J. Phys. F* **13**, 2569-2580 (1983).

19.   S. I. Anisimov, B. L. Kapeliovich, T. L. Perel'man, *Sov. Phys. JETP* **39**, 375 (1974).

20.   P. B. Corkum, F. Brunel, N. K. Sherman, T. Srinivasan-Rao, *Phys. Rev. Lett.* **61**, 2886-2889 (1988).

21.   C. Suárez, W. E. Bron, T. Juhasz, *Phys. Rev. Lett.* **75**, 4536-4539 (1995).

22.   W. S. Fann, R. Storz, H. W. K. Tom, J. Bokor, *Phys. Rev. Lett.* **68**, 2834-2837 (1992).

23.   S. Ogawa, H. Petek, *Surf. Sci.* **357-358**, 585-594 (1996).

24.   C.-K. Sun, F. Vallée, L. H. Acioli, E. P. Ippen, J. G. Fujimoto, *Phys. Rev. B* **50**, 15337-15347 (1994).

25.   B. Feuerbacher, B. Fitton, R. F. Willis, Eds., *Photoemission and the electronic properties of surfaces* (Wiley, New York, 1978).

26.   H. Lüth, *Surfaces and interfaces of solids*. G. Ertl, R. Gomer, D. L. Mills, Eds., Springer Series in Surface Science (Springer-Verlag, Berlin, 1993), vol. 15.

27.   R. G. Musket, W. McLean, C. A. Colmenares, D. M. Makowiecki, W. J. Siekhaus, *Applications of Surf. Sci.* **10**, 143-207 (1982).

28. E. M. Purcell, *Electricity and magnetism*, Berkeley Physics Course (McGraw-Hill Book Company, New York, ed. 2, 1985).

29. J. Grimblot, A. C. Luntz, D. E. Fowler, *Journal of electron spectroscopy and related phenomena* **52**, 161-174 (1990).

30. L. E. Davis, N. C. MacDonald, P. W. Palmberg, G. E. Riach, R. E. Weber, *Handbook of auger electron spectroscopy* (Physical Electronics Industries, Inc., Eden Prairie, ed. 2nd, 1976).

31. H. Steininger, S. Lehwald, H. Ibach, *Surface Science* **123**, 1-17 (1982).

32. J. Gland, V. Secton, G. Fisher, *Surface Science* **95**, 587-602 (1980).

33. W. D. Mieher, W. Ho, *J. Chem. Phys.* **99**, 9279-9295 (1993).

34. T. A. Germer, J. C. Stephenson, E. J. Heilweil, R. R. Cavanagh, *Phys. Rev. Lett.* **71**, 3327 (1993).

35. T. A. Germer, J. C. Stephenson, E. J. Heilweil, R. R. Cavanagh, *J. Chem. Phys.* **101**, 1704 (1994).

36. J. Wintterlin, R. Schuster, G. Ertl, *Phys. Rev. Lett.* **77**, 123-126 (1996).

37. J. Gland, E. Kollin, *J. Chem. Phys.* **78**, 963-974 (1983).

38. T. Matsushima, *Surf. Sci.* **127**, 403-423 (1983).

39. K.-H. Allers, H. Pfnür, P. Feulner, D. Menzel, *J. Chem. Phys.* **100**, 3985-3998 (1994).

40. M. Orchin, H. H. Jaffé, *Symmetry, Orbitals, and Spectra (S.O.S.)* (Wiley-Interscience, New York, 1971).

41. B. C. Stipe, M. A. Rezaei, W. Ho, S. Gao, M. Persson, B. I. Lundqvist, *Phys. Rev. Lett.* **78**, 4410-4413 (1997).

42. A. Eichler, J. Hafner, *Phys. Rev. Lett.* **79**, 4481-4484 (1997).

43. W. Eberhardt, T. H. Upton, S. Cramm, L. Incoccia, *J. Vac. Sci. Tech. A* **6**, 876-877 (1988).

44. W. Wurth, et al., *Phys. Rev. Lett.* **65**, 2426-2429 (1990).

45.   J. L. Gland, V. N. Korchak, *Surf. Sci.* **75**, 733 (1978).

46.   A. W. E. Chan, R. Hoffmann, W. Ho, *Langmuir* **8**, 1111-1119 (1992).

47.   D. A. Outka, J. Stöhr, W. Jark, P. Stevens, J. Solomon, R. J. Madix, *Phys. Rev. B* **35**, 4119-4122 (1987).

48.   B. Hellsing, *Surf. Sci.* **282**, 216-228 (1993).

49.   I. Panas, P. Siegbahn, *Chem. Phys. Lett.* **153**, 458-464 (1988).

50.   N. V. Smith, *Phys. Rev. B* **9**, 1365 (1974).

51.   N. Avery, *Chem. Phys. Lett.* **96**, 371-373 (1983).

52.   K. Mortensen, C. Klink, F. Jensen, F. Besenbacher, I. Stensgaard, *Surface Science* **220**, L701-L708 (1989).

53.   K. Sawabe, Y. Matsumoto, *Chem. Phys. Lett.* **194**, 45-50 (1992).

54.   X.-Y. Zhu, S. R. Hatch, A. Campion, J. M. White, *J. Chem. Phys.* **91**, 5011-5020 (1989).

55.   W. D. Mieher, W. Ho, *J. Chem. Phys.* **91**, 2755-2756 (1989).

56.   D. G. Busch, W. Ho, *Phys. Rev. Lett.* **77**, 1338-1341 (1996).

57.   F.-J. Kao, D. G. Busch, D. G. da Costa, W. Ho, *Phys. Rev. Lett* **70**, 4098-4101 (1993).

58.   F.-J. Kao, D. G. Busch, D. Cohen, D. G. da Costa, W. Ho, *Phys. Rev. Lett.* **71**, 2094-2097 (1993).

59.   H.-L. Dai, W. Ho, Eds., *Laser spectroscopy and photochemistry on metal surfaces Part II*, vol. 5 (World Scientific, Singapore, 1995).

60.   J. A. Misewich, A. Kalamarides, T. F. Heinz, U. Höfer, M. M. T. Loy, *J. Chem. Phys.* **100**, 736-739 (1994).

61.   D. G. Busch, S. Gao, R. A. Pelak, M. F. Booth, W. Ho, *Phys. Rev. Lett.* **75**, 673-676 (1995).

62.   J. A. Prybyla, T. F. Heinz, J. A. Misewich, M. M. T. Loy, J. H. Glownia, *Phys. Rev. Lett.* **64**, 1537-1540 (1990).

63. F. Budde, T. F. Heinz, A. Kalamarides, M. M. T. Loy, J. A. Misewich, *Surf. Sci.* **283**, 143-157 (1993).

64. J. A. Prybyla, H. W. K. Tom, G. D. Aumiller, *Phys. Rev. Lett.* **68**, 503-506 (1992).

65. L. M. Struck, L. J. Richter, S. A. Buntin, R. R. Cavanagh, J. C. Stephenson, *Phys. Rev. Lett.* **77**, 4576-4579 (1996).

66. S. Deliwala, PhD, Harvard University (1995).

67. C. E. Tripa, C. R. Arumaninayagam, J. T. Yates, *J. Chem. Phys.* **105**, 1691-1696 (1996).

68. F. Weik, A. de Meijere, E. Hasselbrink, *J. Chem. Phys.* **99**, 682 (1993).

69. W. Ho, *Surf. Sci.* **363**, 166-178 (1996).

70. C. Springer, M. Head-Gordon, *Chem. Phys.* **205**, 73-89 (1996).

71. J. A. Misewich, T. F. Heinz, D. M. Newns, *Phys. Rev. Lett.* **68**, 3737-3740 (1992).

72. W. S. Fann, R. Storz, H. W. K. Tom, J. Bokor, *Surf. Sci.* **283**, 221-225 (1993).

73. F. Budde, T. F. Heinz, M. M. T. Loy, J. A. Misewich, F. de Rougemont, H. Zacharias, *Phys. Rev. Lett.* **66**, 3024-3027 (1991).

74. A. N. Artsyukhovich, I. Harrison, *Surface Science* **350**, L199-L204 (1996).

75. K. Sawabe, J. Lee, Y. Matsumoto, *J. Chem. Phys.* **99**, 3143-3146 (1993).

76. J. Kiss, J. M. White, *J. Phys. Chem.* **95**, 7852-7857 (1991).

77. V. A. Ukraintsev, I. Harrison, *J. Chem. Phys.* **96**, 6307-6310 (1992).

78. E. P. Ippen, C. V. Shank, *Appl. Phys. Lett.* **27**, 488-490 (1975).

79. J. A. Misewich, T. F. Heinz, P. Weigand, A. Kalamarides, in *Laser spectroscopy and photochemistry on metal surfaces Part II* H.-L. Dai, W. Ho, Eds. (World Scientific, Singapore, 1995), vol. 5,.

80. E. M. Stuve, R. J. Madix, B. A. Sexton, *Chem. Phys. Lett.* **89**, 48-53 (1982).

81. C. T. Rettner, J. Lee, *J. Chem. Phys.* **101**, 10185-10188 (1994).

82. H. P. Bonzel, A. M. Franken, G. Pirug, *Surf. Sci.* **104**, 625-642 (1981).

83. H. Niehus, G. Comsa, *Surf. Sci.* **102**, L14-L20 (1981).

84.   H. Niehus, G. Comsa, *Surf. Sci.* **93**, L147-L150 (1980).

85.   M. Mundschau, R. Vanselow, *Surf. Sci.* **157**, 87-98 (1985).

86.   R. M. Osgood, T. F. Deutsch, *Science* **227**, 709-714 (1985).

87.   T. J. Chuang, *J. Chem. Phys.* **74**, 1453 (1981).

88.   M. Müllenborn, H. Dirac, J. W. Petersen, *App. Surf. Sci.* **86**, 568-576 (1995).

89.   R. Kullmer, D. Bäuerle, *Apply. Phys. A* **43**, 227-232 (1987).

90.   H. Okano, Y. Horiike, M. Sekine, *Jap. J. App. Phys.* **24**, 68-74 (1985).

91.   G. V. Treyz, R. Scarmozzino, H. H. Burke, R. M. Osgood Jr., *Mat. Res. Soc. Symp. Proc.* **129**, 291-297 (1989).

92.   M. Kawasaki, H. Sato, N. Nishi, *Mat. Res. Soc. Symp. Proc.* **129**, 305-309 (1989).

93.   F. Komori, K. Hattori, *SPIE* **2547**, 285-295 (1995).

94.   W. Sesselmann, E. Hudeczek, F. Bachmann, *J. Vac. Sci. Technol. B* **7**, 1284-1294 (1989).

95.   J. Ihlemann, B. Wolff, P. Simon, *Appl. Phys. A* **54**, 363-368 (1992).

96.   Y. K. Jhee, M. F. Becker, R. M. Walser, *J. Opt. Soc. Am. B* **2**, 1626-1633 (1985).

97.   J. Carvalho, I. Ferreira, B. Fernandes, J. Fidalgo, R. Martins, *Mat. Res. Soc. Symp. Proc.* **358**, 915-920 (1995).

98.   R. I. Johnson, G. B. Anderson, J. B. Boyce, D. K. Fork, P. Mei, S. E. Ready, S. Chen, *Mat. Res. Soc. Symp. Proc.* **297**, 533-538 (1993).

99.   P. L. Liu, R. Yen, N. Bloembergen, R. T. Hodgson, *Appl. Phys. Lett.* **34**, 864-866 (1979).

100. D. von der Linde, K. Sokolowski-Tinten, J. Bialkowski, *Appl. Surf. Sci.* **109/110**, 1-10 (1997).

101. S. Nolte, C. Momma, H. Jacobs, A. Tünnermann, B. N. Chichkov, B. Wellegehausen, H. Welling, *J. Opt. Soc. Am. B* **14**, 1-7 (1997).

102. C. Momma, S. Nolte, B. N. Chichkov, F. v. Alvensleben, A. Tünnermann, *Appl. Surf. Sci.* **109/110**, 15-19 (1997).

103. W. Kautek, J. Krüger, *Materials Science Forum* **173-174**, 17-22 (1995).

104. E. N. Glezer, M. Milosavljevic, L. Huang, R. J. Finlay, T.-H. Her, J. P. Callan, E. Mazur, *Optics Letters* **21**, 2023-2025 (1996).

105. B. Dam, J. H. Rector, J. Johansson, S. Kars, R. Griessen, *Appl. Surf. Sci* **96-98**, 679-684 (1996).

106. B. Hopp, M. Csete, K. Révész, J. Vinkó, Z. Bor, *Appl. Surf. Sci.* **96-98**, 661-616 (1996).

107. J. F. Young, J. S. Preston, H. M. van Driel, J. E. Sipe, *Phys. Rev. B* **27**, 1115-1172 (1983).

108. P. M. Fauchet, A. E. Siegman, *Appl. Phys. Lett.* **40**, 824-826 (1982).

109. M. F. von Allmen, S. S. Lau, in *Laser annealing of semiconductors* J. M. Poate, J. W. Mayer, Eds. (Academic Press, New York, 1982) pp. 564.

110. W. Jiang, H. Baumgärtner, I. Eisele, *App. Surf. Sci.* **86**, 564-567 (1995).

111. E. N. Glezer, C. B. Schaffer, N. Nishimura, E. Mazur, *Opt. Lett. in press* .

112. E. N. Glezer, E. Mazur, *Appl. Phys. Lett.* **71**, 882-884 (1997).

113. P. Saeta, J.-K. Wang, Y. Siegel, N. Bloembergen, E. Mazur, *Phys. Rev. Lett.* **67**, 1023- (1991).

114. J. A. V. Vechten, R. Tsu, F. W. Saris, D. Hoonhout, *Phys. Lett.* **74A**, 417 (1979).

115. Z. Guosheng, P. M. Fauchet, A. E. Siegman, *Phys. Rev. B* **26**, 5366-5381 (1982).

116. J. E. Sipe, J. F. Young, J. S. Preston, H. M. van Driel, *Phys. Rev. B* **27**, 1141-1154 (1983).

117. E. A. Ogryzlo, D. E. Ibbotson, D. L. Flamm, J. A. Mucha, *J. Appl. Phys.* **67**, 3115-20 (1990).

118. P. L. Silvestrelli, A. Alavi, M. Parrinello, D. Frenkel, *Phys. Rev. B* **56**, 3806-3812 (1997).

119. V. V. Zhirnov, E. I. Givargizov, P. S. Piekhanov, *J. Vac. Sci. Technol. B* **13**, 418-421 (1994).

120. E. I. Givargizov, *J. Vac. Sci. Technol. B* **11**, 449-453 (1993).

121. S. Kim, B. K. Ju, Y. H. Lee, B. S. Park, Y.-J. Baik, S. Lim, M. H. Oh, *J. Vac. Sci. Technol. B* **15**, 499-502 (1997).

122. Y. A. Grigoriev, et al., *J. Vac. Sci. Technol. B.* **15**, 503-506 (1997).

123. Y. V. Gulyaev, L. A. Chernozatonskii, Z. J. Kosakovskaja, N. I. Sinitsyn, G. V. Torgashov, Y. F. Zakharchenko, *J. Vac. Sci. Technol. B* **13**, 435-436 (1995).

124. T. Asano, Y. Oobuchi, S. Katsumata, *J. Vac. Sci. Technol. B* **13**, 431-434 (1994).

125. K. Otsuka, M. Kunieda, H. Yamagata, *J. Electrochem. Soc.* **139**, 2381-2386 (1992).

126. T. F. Hunter, D. Rumbles, M. G. Stock, *Chem. Phys. Lett.* **45**, 145-149 (1977).

127. O. Dippel, F. Cemic, E. Hasselbrink, *Surf. Sci.* **357-358**, 190-194 (1996).

128. J. M. White, *J. Vac. Sci. Technol. B* **10**, 191-195 (1992).
129. J. E. Whitten, R. Gomer, *Surf. Sci.* **347**, 280-288 (1996).

130. T. M. Orlando, A. R. Burns, E. B. Stechel, D. R. Jennison, *J. Chem. Phys.* **93**, 9197-9199 (1990).

131. C. Lutterloh, J. Biener, K. Pöhlmann, A. Schenk, J. Küppers, *Surf. Sci.* **352-354**, 133-137 (1996).

132. D. F. Ogletree, M. A. Van Hove, G. A. Somorjai, *Surf. Sci.* **183**, 1-20 (1987).

133. A. Wander, et al., *Surf. Sci.* **249**, 21-34 (1991).

134. T. Goulet, J.-P. Jay-Gerin, *Solid State Communications* **55**, 619-623 (1985).